U.S. DEPARTMENT OF COMMERCE
National Technical Information Service
PB-292 654

Comparison of Linear Induction Motor Theories for the LIMRV and TLRV Motors

(U.S.) Transportation Systems Center, Cambridge, MA

Prepared for

Federal Railroad Administration, Washington, DC Office of Research and Development

Jan 78

PB 292654

REPORT NO. FRA/ORD-77/68

COMPARISON OF LINEAR INDUCTION MOTOR THEORIES FOR THE LIMRV AND TLRV MOTORS

John J. Stickler
U.S. Department of Transportation
Transportation Systems Center
Kendall Square
Cambridge MA 02142

JANUARY 1978
FINAL REPORT

Prepared for
U.S. DEPARTMENT OF TRANSPORTATION
FEDERAL RAILROAD ADMINISTRATION
Office of Research and Development
Washington DC 20590

Technical Report Documentation Page

1. Report No	2. Government Accession No	3. Recipient's Catalog No
FRA/ORD-77/68		PB292654

4. Title and Subtitle	5. Report Date
COMPARISON OF LINEAR INDUCTION MOTOR THEORIES FOR THE LIMRV AND TLRV MOTORS	January 1978
	6. Performing Organization Code
7. Author's	8. Performing Organization Report No
John J. Stickley	DOT-TSC-FRA-77-21
9. Performing Organization Name and Address	10. Work Unit No (TRAIS)
U.S. Department of Transportation Transportation Systems Center Kendall Square Cambridge MA 02142	RR730/R8728
	11. Contract or Grant No
	13. Type of Report and Period Covered
12. Sponsoring Agency Name and Address	Final Report July 1977 - Aug. 1977
U.S. Department of Transportation Federal Railroad Administration Office of Research and Development Washington DC 20590	14. Sponsoring Agency Code

15. Supplementary Notes

16. Abstract

The Oberretl, Yamamura, and Mosebach theories of the linear induction motor are described and also applied to predict performance characteristics of the TLRV & LIMRV linear induction motors. The effect of finite motor width and length on performance predictions is examined for each theory. The edge and end effects are shown to play a dominant role in determining motor performance.

The LIM thrusts predicted by the Oberretl, Yamamura, and Mosebach computer models are in reasonable agreement over most of the LIM speed range. The Oberretl theory tends to predict somewhat lower thrust values than the Yamamura and Mosebach theories; possible causes for the divergent thrust predictions are discussed.

Computer listings for the Oberretl and Yamamura linear induction motor theories are presented in the appendix.

17. Key Words	18. Distribution Statement
Linear Induction Motor, LIM Propulsion Characteristics, TLRV & LIMRV Motors	DOCUMENT IS AVAILABLE TO THE U.S. PUBLIC THROUGH THE NATIONAL TECHNICAL INFORMATION SERVICE, SPRINGFIELD, VIRGINIA 22161

19. Security Classif. (of this report)	20. Security Classif. (of this page)	21. No. of Pages	22. Price
Unclassified	Unclassified	146	A07-A01

Form DOT F 1700.7 (8-72) Reproduction of completed page authorized

PREFACE

The work described in this report was the result of a request by the Office of Research and Development of the Federal Railroad Administration (FRA) for a study of current leading theories of linear induction motors (LIMs) as applied to the analysis of high speed linear motors. The work was directed for the FRA by Matthew Guarino, Jr.

The study was conducted at the Power & Propulsion Branch of the Transportation Systems Center (TSC), Cambridge, Massachusetts. The computer facilities at TSC were solely used for the numerical investigations contained in this report.

Dr. David G. Elliott of the Jet Propulsion Laboratory, Pasedena, California, provided extensive assistance during the course of the program and supplied helpful data on mesh-matrix predictions of LIM performance. Dr. Elliott was also helpful in providing values for certain LIM parameters used in the numerical studies.

The work benefited from valuable technical discussions with Dr. C.A. Skalski, The Mitre Corporation and Prof. J. Melcher, Massachusetts Institute of Technology.

The author wishes to thank Dr. H. Mosebach, University of Braunschweig, Braunschweig, Germany for permission to use certain material contained in a prior publication as well as for reviewing sections of the report describing the Mosebach treatment of linear induction motors.

The author takes particular pleasure in acknowledging the continuing support and active participation of Matthew Guarino, Jr. throughout the course of this program. His frequent discussions and helpful suggestions were largely responsible for much of the progress and ultimate accomplishments of this study effort.

METRIC CONVERSION FACTORS

Approximate Conversions to Metric Measures

Symbol	When You Know	Multiply by	To Find	Symbol
	LENGTH			
in	inches	2.5	centimeters	cm
ft	feet	30	centimeters	cm
yd	yards	0.9	meters	m
mi	miles	1.6	kilometers	km
	AREA			
in²	square inches	6.5	square centimeters	cm²
ft²	square feet	0.09	square meters	m²
yd²	square yards	0.8	square meters	m²
mi²	square miles	2.6	square kilometers	km²
	acres	0.4	hectares	ha
	MASS (weight)			
oz	ounces	28	grams	g
lb	pounds	0.45	kilograms	kg
	short tons (2000 lb)	0.9	tonnes	t
	VOLUME			
tsp	teaspoons	5	milliliters	ml
tbsp	tablespoons	15	milliliters	ml
fl oz	fluid ounces	30	milliliters	ml
c	cups	0.24	liters	l
pt	pints	0.47	liters	l
qt	quarts	0.95	liters	l
gal	gallons	3.8	liters	l
ft³	cubic feet	0.03	cubic meters	m³
yd³	cubic yards	0.76	cubic meters	m³
	TEMPERATURE (exact)			
°F	Fahrenheit temperature	5/9 (after subtracting 32)	Celsius temperature	°C

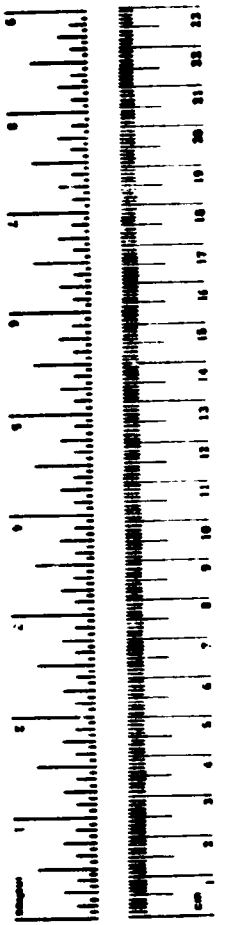

Approximate Conversions from Metric Measures

Symbol	When You Know	Multiply by	To Find	Symbol
	LENGTH			
mm	millimeters	0.04	inches	in
cm	centimeters	0.4	inches	in
m	meters	3.3	feet	ft
m	meters	1.1	yards	yd
km	kilometers	0.6	miles	mi
	AREA			
cm²	square centimeters	0.16	square inches	in²
m²	square meters	1.2	square yards	yd²
km²	square kilometers	0.4	square miles	mi²
ha	hectares (10,000 m²)	2.5	acres	
	MASS (weight)			
g	grams	0.035	ounces	oz
kg	kilograms	2.2	pounds	lb
t	tonnes (1000 kg)	1.1	short tons	
	VOLUME			
ml	milliliters	0.03	fluid ounces	fl oz
l	liters	2.1	pints	pt
l	liters	1.06	quarts	qt
l	liters	0.26	gallons	gal
m³	cubic meters	35	cubic feet	ft³
m³	cubic meters	1.3	cubic yards	yd³
	TEMPERATURE (exact)			
°C	Celsius temperature	9/5 (then add 32)	Fahrenheit temperature	°F

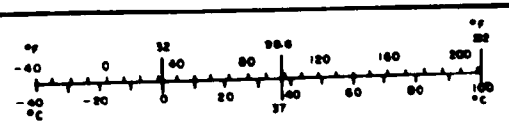

CONTENTS

CONTENTS (CONT.)

CONTENTS (CONT.)

LIST OF ILLUSTRATIONS

LIST OF ILLUSTRATIONS

LIST OF ILLUSTRATIONS

LIST OF TABLES

LIST OF TABLES (CONT.)

LIST OF SYMBOLS

Symbol	
a_k	wave vector component along x direction
a_n	Normalized Fourier coefficient of stator current sheet
A_z	stator current sheet
b	Secondary thickness
b_n^k	normalized Fourier coefficient of stator current sheet
B	magnetic flux density
B_n	complex Fourier coefficient of magnetic flux density
$\bar{B}$	matrix with Fourier coefficients of magnetic flux density
c	Half-width of primary (stator)
d_s	'sidebar' width of secondary
E_x	electric field along x direction
E_z	electric field along z direction
f	frequency
$f_k(x)$	parameter describing occupancy of stator slots of kth phase
F_x	total thrust (average)
$F(\nu,n)$	Thrust harmonic
g	Airgap separating primary and secondary
h	Distance beyond primary edge defining effective decay distance of primary mmf.
I_1	Stator coil current per phase
I^k	exciting current of phase k
j	$\sqrt{-1}$
J_1	primary current density - amps/(meter)^2
J_2	secondary current density - amps/(meter)^2

LIST OF SYMBOLS (CONT.)

k	index defining phase number
k_x, k_z	fundamental wave number components in x,z directions
K_1	primary current density - amps/meter
K_2	secondary current density - amps/meter
KP	ratio of expansion length to primary winding length
ℓ	length of periodic cell in longitudinal (x) direction
L	width of periodic cell in transverse (z) direction
m	number of primary phases
N	turns per coil
NMAX	maximum longitudinal harmonic order
P	number of poles
P_{ag}	airgap power
P_m	mechanical power
P_{sec}	secondary power loss
q	number of slots in given phase belt
r	magnetic Reynold's number
r'	modified magnetic Reynold's number
R	matrix with effective Reynolds number in diagonal element
R_1	primary phase resistance
s	slip
t	time
V	motor speed
V^k	voltage of kth phase winding
x	longitudinal direction
X_1	primary leakage reactance
X_2	secondary leakage reactance
X_m	magnetizing reactance

LIST OF SYMBOLS (CONT.)

y	direction normal to primary surface
y_1	half-thickness of secondary
y_2	half-width of core-to-core separation
y_{20}	half core-to-core separation within primary region
Y	matrix with Fourier coefficients of $y_2(x)$
z	transverse direction
Z_{ag}	airgap phase impedance
Z_{in}	input impedance of phase winding
$Z^{kk'}$	elements of input impedance matrix
α	Slot pitch in radians
α_z	Primary sheet current density in z direction
ε	Parameter defining stator pole pitch
κ	Index defining coil in given coil group
μ_o	Permeability of free space
m_2	Permeability of Secondary
ν	Longitudinal harmonic order
ρ	Index defining coil group in given phase
σ_2	Secondary conductivity
τ_p	pole pitch
ω	angular frequency

1. INTRODUCTION

Recent interest in linear induction motor applications for high speed ground transportation has stimulated a number of theoretical investigations of single and double-sided linear induction motors (LIMs). As a result of these investigations, different mathematical LIM models have been developed and applied to predict the performance characteristics of real LIMs. This report describes three such models representing widely different approaches for treating linear induction motors. The mathematical theories based on these models comprise three current LIM theories which have been applied with a high degree of success to investigate the performance characteristics of different high speeds LIMs. These include the LIM theories developed by K. Oberretl[1] (Brown-Boveri, Zurich, Switzerland), S. Yamamura[2] (University of Tokyo, Japan), and H. Mosebach[3] (University of Braunschwieg, Braunschweig, Germany).

This study has several objectives. One of these objectives is the development of software (computer models) which could be used for parametric studies of linear motors. In the past, such software has proved helpful in the analysis of LIM test data, as for example, through the comparison of measured test data with predicted LIM performance, and as a tool to be used in the design of linear induction motors. During the course of this study, computer programs were developed for the Yamamura (one-dimensional) model and the Oberretl (three-dimensional) model; this software was later supplemented by a computer program describing the Mosebach (one-dimensional) model, courtesy of Prof. H. Mosebach. All three computer programs were extensively used in the early phases of this investigation to study the effectiveness of the three theories in predicting real motor characteristics. In the later phases of the investigation, software studies were directed more towards examining the limitations of each theory as related to approximations introduced in the mathematical solution of the wave equation. These numerical studies were restricted to two

particular high speed linear induction motors, namely the Linear Induction Research Vehicle (LIMRV) LIM and the Tracked Levitated Research Vehicle (TLRV) LIM. This insured a common base for the analysis of the three theories and for the quantification of differences in LIM performance as predicted by the three theories. The availability of LIMRV test data obtained from test runs conducted at Pueblo, Colorado, proved particularly helpful in assessing the reliability of these theories.

Another objective of this program is the in-depth study of the Mosebach, Oberretl, and Yamamura LIM models and the field solutions of Maxwell's equations appropiate to each model. If boundary effects are ignored, the models predict motor performance which is characteristic of 'idealized' rotary induction machines. With boundary conditions included in the model description, the theories exhibit large differences depending upon the relative importance each theory assigns to a given boundary phenomena. Thus, the Mosebach model neglects variations in field quantities along the LIM normal axis but includes boundary effects associated with the finite size of the primary ferromagnetic region (stator core). The Oberretl and Yamamura models include the variations in field quantities along the LIM normal axis but, neglect boundary conditions associated with the finite size of the primary ferromagnetic region. One purpose of this study is to examine the different LIM models and to investigate the effect of the different boundary conditions and assumptions on predicted LIM performance.

During the initial phases of this study, the Oberretl and Yamamura theoretical preditions were compared with similiar predictions based on the mesh-matrix method* of LIM analysis. The mesh-matrix theory as developed by Dr. D. Elliott includes the effect of a finite length stator core structure which is neglected in the Oberretl and Yamamura theories. Later in the study, the Mosebach computer program became available and was subsequently

*Calculations based on the mesh-matrix approach were kindly supplied by Dr. D. Elliott, JPL, Pasadena, California.

used to provide comparative data describing the effect of finite core length on LIM performance.

The remaining sections of this report describe the Oberretl, Yamamura, and Mosebach theories of the linear induction motor. Each section contains a description of the respective LIM model and the mathematical solution of the wave equations with boundary conditions appropiate to each model. The final material in each section presents numerical studies of predicted LIM performance using computer models developed during the course of the work. The numerical studies were restricted to the LIMRV and TLRV linear induction motors. This was done intentionally in order to provide a common base for the comparison of the different theoretical prediction and to give a basis for judging the practicability of each theory through comparison of predicted and measured LIM data. Each section contains a summary of conclusions describing the significant results obtained during the course of the study. These conclusions together with the supplementary review material contained in the introduction should provide the reader with an appreciation of the capabilities as well as limitations of the three theories. Since the original publication of the Oberretl, Yamamura, and Mosebach LIM treatments, some modifications of the theories have appeared in the literature. These modifications involve only slight changes in the theories and refinements in the models. Their publication does not detract from the value of this report in presenting an in-depth review of three current leading LIM theories.

2. TECHNICAL DISCUSSION

An exact EM wave solution of a finite linear motor is impossible and one must attempt either approximate solutions of the real complex machine or exact solutions based on idealized models of real machines. The latter approach is the one most commonly adopted in most LIM treatments. The LIM stator (primary) is generally described by an equivalent MMF distribution of finite length and width 'supported' by ferromagnetic backing of infinite permeability. The LIM reaction rail (secondary) is represented by a conducting sheet of uniform thickness and conductivity. The finite size of the stator (iron) core is treated in the Mosebach analysis, as an equivalent airgap function which is designed to yield fringing fields at both motor ends in close agreement with measured fringing fields. The problem of leakage fields and their description in the LIM model is one usually omitted in LIM treatments. The effect of such fields is most easily handled in an equivalent circuit representation using empirically derived values for the primary and secondary leakage reactances.

An exact representation of a real LIM by an equivalent model would require the model to duplicate the MMF and field distributions of the real LIM at all points in space. Since the mathematical description of such a model would be impossibly difficult, the alternative is to seek a model which simulates the current-field distributions within the active region of the motor or which approximates the field distribution at the midplane of the LIM. Once the B, H distributions are defined along the midplane, the LIM thrust and normal force components can be evaluated using the Maxwell stress tensor.

One method of developing a LIM model is to conceive of the model as comprising an idealized rotary induction motor with superimposed boundary conditions to simulate the finite motor structure. This approach requires boundary conditions to be specified at the edge boundaries of the motor; in addition, the EM configuration of the adjoining regions must also be defined.

The manner in which these boundary conditions are set forth distinguishes the three theories from each other. In each of the three theories, the transverse edge-effect and end-effect have an important effect in determining LIM performance. Both boundary effects lead to solutions of Maxwell's equations which are describable by damped exponential waves. The waves produced by the transverse edge boundaries propagate inwards from both edges; the corresponding waves generated by the longitudinal end boundaries propagate along the longitudinal axis of the LIM. The manner in which these boundary effects are included in the LIM models is discussed below.

A. LIM Edge-Effect

The LIM edge-effect results from the finite width of the motor stator and the finite width of the secondary reaction rail. The currents flowing in the secondary are constricted at the edge regions due to the finite extention of the secondary in the overhang region. Unlike squirrel-cage induction motors, the secondary currents are not confined to fixed current contours but are free to flow in paths limited only by the width of the conducting sheet. The current flow pattern is dictated by the relative path impedances for the different current contour paths. These path impedances change with slip-frequency resulting in flow patterns which likewise vary with slip-frequency. A desirable characteristic of the LIM model is its ability to describe changing secondary current flow patterns with different operating conditions of the motor.

One consequence of the finite width of the LIM stator is the difference in reluctance experienced by flux at the motor edge compared with the flux within the 'active' region of the motor. This is illustrated by the sketch shown in Figure 1 giving the airgap flux components and the currents in the LIM secondary. Flux generated by the secondary currents closes around both the active current component, J_z, and the cross-current component, J_x. The path reluctance associated with the flux component, FR_1, and determined by the gap between primary cores, is considerably

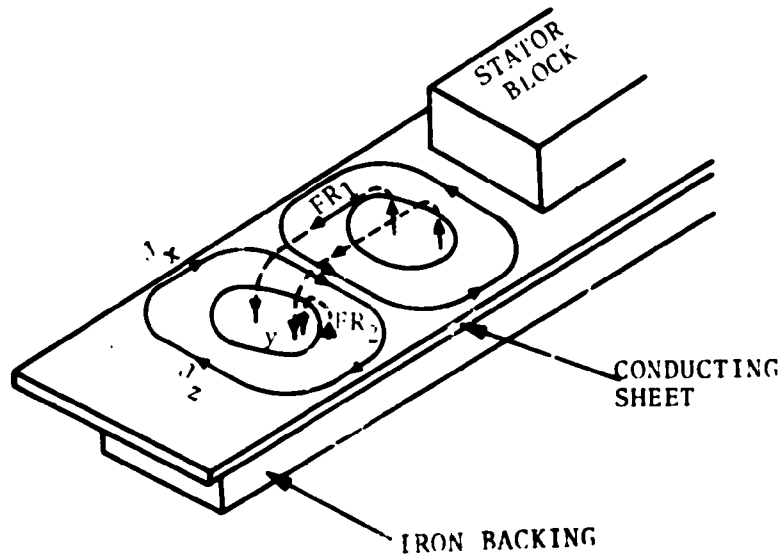

FIGURE 1. SKETCH OF LIM FLUXES AND CURRENTS IN A SHEET-ROTOR

less than the path reluctance for flux component, FR_2. A further difference exists also in the fact that flux component, FR_1, enters the stator block within the plane of the stator laminations while flux component, FR_2, enters the stator block in a direction at right angles to the plane of the laminations. In the latter case, Eddy currents are generated in the laminations, which further act to increase the effective path reluctance of flux component, FR_2.

The Mosebach (one-dimensional) and Yamumura (Bolton edge correction) theories take account of the different path reluctances by setting the edge path reluctance equal to infinity. This assumption forces the field outside the motor edge to be zero. The Bolton theory of the transverse edge effect,[4] which is used by Yamamura to correct for edge-effect, predicts transverse flux distributions which agree closely with field distributions in LIMs operating at low speeds. Since the Bolton analysis neglects end-effect, the Bolton correction factors should be less accurate at high LIM speeds where end-effect becomes important. A more exact treatment would include edge-effect corrections for all harmonic waves propagating in the LIM, including the harmonic waves whose sum comprise the end-effect waves.

The Mosebach (one-dimensional) theory includes the higher harmonic fields in the treatment of the edge-effect; however, it introduces some severe restrictions regarding the shape of the secondary current path distribution. This is illustrated in Figure 2, which shows a sketch of the secondary current flow pattern as assumed in the Mosebach model. Within the active region of the motor, i.e., [illegible], only z-directed (transverse) currents flow; outside the active region, only x-directed currents flow. The increased current path required for the secondary current results in an increase in the effective secondary resistivity over that which would exist for the case of an infinite sidebar conductivity. It can be shown that the increase in the effective secondary resistivity for the Mosebach model is equivalent to the corresponding increase in effective resistivity in the Bolton analysis at low slip-frequencies, i.e., when the LIM is operated

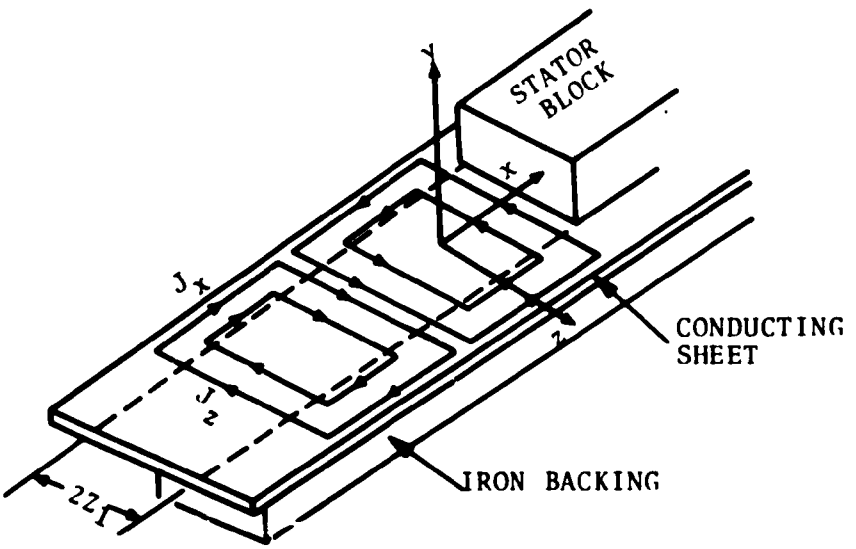

FIGURE 2. SKETCH OF LIM SECONDARY CURRENT PATTERN IN MOSEBACH ONE-DIMENSIONAL LIM MODEL

in the resistive mode. When the LIM is driven at higher slip frequencies, i.e., in the inductive mode, the Mosebach edge-effect treatment yields results which diverge from those of Bolton. The matter of judgment enters into the choice of which model to use when examining a specific operating region of the LIM. Based upon the edge-effect consideration, one would expect the Yamamura model using the Bolton edge correction to be the best choice at high slip-frequencies (low motor speeds) and the Mosebach model to be the best choice at low slip-frequencies.

The Oberretl model treats the transverse edge effect in the same way as the longitudinal end-effect. It includes the simultaneous interaction or coupling between the edge and end-effect phenomena. A limiting feature in the Oberretl theory is its assumption of continuous ferromagnetic region in the primary, that is the stator core is assumed to extend to infinity along the plane of the motor. This assumption leads to excessively large magnetic fields in the trailing end of the LIM at high motor speeds. While such fields have little effect on LIM thrust, they do tend to exaggerate the LIM normal force and total magnetic energy stored in the LIM.

The Oberretl model treats the real LIM as an array of periodic cells extending along the longitudinal and transverse axes of the motor. This representation permits the two-dimensional Fourier expansion of the motor currents and fields along the principal axes using as base wavelength the length of the periodic unit cell. In the expansion along the transverse axis, the cell length is taken as the width of the secondary. A practical problem exists in the Fourier expansion when one attempts to describe the rapidly varying fields at the motor edges using a Fourier cell which extends only a short distance beyond the motor edge. A relatively large number of harmonics is required in such an expansion to describe the rapid field variation. Since the Fourier expansion must be limited to a finite number of terms, a judgment must be made on the maximum number of terms to use based on desired accuracy and computer costs required for the calculations.

B. LIM End-Effect

In constrast to the edge-effect which alters LIM performance over the complete range of operating speeds, the end-effect, associated with the finite length of the LIM, affects motor performance predominantly only at high motor speeds and low operating slip-frequencies. This applies to end-effect arising from both the finite length of primary MMF distribution and finite length of the stator core.

The finite MMF distribution is modelled in the three LIM theories as an equivalent sheet current density extending over the length of the primary excitation. The Mosebach and Oberretl models provide for arbitrary primary current excitations using Fourier expansions to develop the equivalent current density distribution. The Yamamura model is not refined to include arbitrary primary excitations; instead, the primary excitation is restricted to a fundamental wave which extends over a motor length equal to the distance spanned by the equivalent number of electrical poles. In using the Yamamura model, one should consider the relative amplitudes of the higher primary current harmonics and their possible effect on the predicted LIM performance. Fortunately, the fifth, seventh, and higher-harmonics generally contribute very little to LIM thrust under most conditions and their neglect does not introduce significant errors in the computed LIM characteristics.

The Oberretl and Yamamura models assume the primary ferromagnetic region is continuous in the plane of the motor, while the Mosebach model is refined to include the finite length of the primary ferromagnetic region. The so-called magnetic end-effect associated with the finite iron core structure becomes important at high motor speeds and low slip-frequencies. In this region of LIM operation, the Mosebach model predicts a lower thrust and output mechanical power than that predicted by the Oberretl and Yamamura models. A more dramatic difference in predicted motor characteristics occurs in the estimated LIM normal forces and power factor. Since the assumption of continuous ferromagnetic

region leads to large flux distributions in the trailing (wake) region of a high-speed LIM, the Oberretl and Yamamura models overestimate the attractive normal forces developed between the two halves of the LIM primary and the total stored magnetic energy in the field. The latter is reflected in larger input voltages to the LIM for a given output power delivered by the LIM, or equivalently to a larger input impedance to the LIM. From the standpoint of the use of the computer program for LIM design, the Mosebach program offers an advantage over the Oberretl and Yamamura programs. In addition to predicting more realistic magnitudes for the stored magnetic energy, the Mosebach program is capable of computing the input impedance as seen by each phase winding of the LIM. From this, one is able to estimate the degree of phase unbalance existing between the different motor windings, and to evaluate the effect of such unbalance on the operation of the LIM power conditioning equipment.

2.1 THE OBERRETL THEORY OF THE LINEAR INDUCTION MOTOR

2.1.1 The Oberretl LIM Model[1]

The Oberretl treatment of linear induction motors begins by replacing the actual LIM with a three-dimensional model, combining a two-dimensional Fourier mmf distribution with an exact solution of the diffusion equation along the direction normal to the primary surface. The mmf is developed by superimposing mmf contributions from an infinite array of adjacent primary elements lying in the plane of the stator. This leads to a Fourier series representation for the total mmf equal to the sum of an infinite number of (mmf) harmonics, each defined by its respective harmonic-order along the longitudinal and transverse wave vector directions. To limit the time required for numerical computations, a limit is imposed on the maximum number characterizing the series. The choice of the values of maximum harmonic number represents a compromise between excessive computing time and sufficient harmonics required to describe adequately the mmf-distribution. The airgap flux density, which is also expressed in a Fourier series, is

derived from the magnetic vector potential with suitable prescribed boundary conditions. LIM thrust and normal forces are determined by integrating the Maxwell Stress Tensor over the region bounded on one side by the secondary.

The Oberretl model is based on the following assumptions:

a. Current densities normal to the primary and secondary members are zero. Current flow in the primary and secondary elements lies in a plane parallel to the primary.

b. The permeability of the primary is infinite.

c. Edge-effects associated with the primary ferromagnetic region are neglected; i.e., magnetic end-effects are absent. Only end-effects associated with finite winding current distributions are included in the analysis.

d. The active primary current density is constant along the transverse direction within the confines of the primary (stator) and decays to zero at a distance, h, beyond the primary edge according to $1 - \sin \frac{(z-c)\pi}{2h}$, where z is the transverse distance relative to the primary midplane and c is the half-width of the primary element. As pointed out by Oberretl, other current density functions could be substituted for the above, provided they relate correctly to measured field distributions.

e. The mmf and flux density distributions are periodic functions of distance along the longitudinal and transverse directions of the motor. To develop this periodicity, mmf gaps are inserted at periodic positions along the longitudinal and transverse axes of the motor.

2.1.1.1 Criteria for Choosing Longitudinal MMF Gap

The Oberretl theory inserts an mmf gap adjacent to the primary in order to develop an mmf-distribution function which is periodic along the longitudinal (and transverse) axis of the motor. The choice of longitudinal gap length is critical in that too small a gap length causes unrealistic oscillations in the thrust-frequency characteristic while too large a gap length results in an

unreasonably long computation time. The criteria adopted in choosing the gap length is that the length be sufficiently long to allow the end-effect wave to decay to a small value. A choice of gap length equal to twice the decay length of the end-effect wave appears to be a reasonable compromise.

The decay length of the principal end-effect wave is given approximately by the reciprocal of the following quantity,[4]

$$\text{REAL}\left(\frac{\mu_o V}{2\rho_s g} - \frac{1}{2}\sqrt{\left(\frac{\mu_o V}{\rho_s g}\right)^2 + j\,\frac{4\omega\mu_o}{\rho_s g}}\right) \tag{1}$$

for LIMs having a pole gap separation g, secondary surface resistivity ρ_s, stator excitation frequency ω, and motor speed V relative to the secondary rail. For the TLRV LIM operating at 300 mph and a frequency of 165 Hz, the computed decay length was 11 meters; for the LIMRV operating at 250 mph and a frequency of 165 Hz, the computed decay length was 7.3 meters. See pages 26 and 32 for a summary of motor parameters describing the respective motors. In the computer studies of the TLRV and LIMRV motors, the respective gap lengths chosen were 33.212 and 11.096 meters.

2.1.1.2 Primary Winding Factor

Oberretl expresses the primary mmf, $\theta(x,t)$, in terms of the sum of mmfs of each coil described by

$$\theta(x,t) = j\,\frac{2NI_1\sqrt{2}\,{}^{\nu}k_w}{\pi\nu}\,e^{\,j\,(\omega t-\nu x+\nu\beta+\pi/m)}. \tag{2}$$

${}^{\nu}k_w$ is the winding factor associated with the νth harmonic, β is the phase angle of the harmonic, m is the number of phases in the winding, and N is the number of turns in each coil. The derivation of ${}^{\nu}k_w$ follows from summing the mmf contributions of each coil described by

$$\nu_\theta = \frac{NI\sqrt{2}\sin\nu(mq-\varepsilon)\frac{\alpha}{2}}{\pi\nu}\,e^{j\left[\omega t-\nu x-(k-1)\frac{2\pi}{m}+\nu(K-1)\alpha\right.}$$
$$\left.+\,\nu(\rho-1)mq\alpha+\nu(k-1)2q\alpha\right]. \tag{3}$$

Here α is the slot pitch in radians, k denotes the phase number, q denotes the particular coil in a given phase group, and ε is the reduction in width of the coils (coil pitch) in units of slots. For a double-layer winding with half-filled end slots, there exist

1, 2,.....k.....m phases,
1, 2,.....κ.....q coils in each coil group,
1, 2,.....ρ.....p* coil groups per phase.

The series summation of coils in a phase group leads to

$$\frac{\sin q\frac{\nu\alpha}{2}}{\sin\frac{\nu\alpha}{2}} e^{j(q-1)\frac{\nu q\alpha}{2}}.$$

The series summation of phase groups associated with the m phases of the primary yields

$$\frac{\sin m(\nu q\alpha-\pi/m)}{\sin (\nu q\alpha-\pi/m)} e^{j(m-1)(\nu q\alpha-\pi/m)}.$$

The series summation of the coil groups of a given phase gives

$$\frac{\sin \frac{P}{2} \nu mq\alpha}{\sin \nu mq\alpha} e^{j\left(\frac{p-1}{2}\right) m\nu q\alpha}.$$

Finally, the "reverse-connected" coil groups are related to the "forward-connected" coil groups by the factor

*Note that Oberretl uses p to denote pole pairs.

$$1 - \exp^{j(\nu mq\alpha - \pi)} = 2j \sin\frac{\nu mq\alpha}{2}$$

since the "reverse-connected" coil groups are both spatially and electrically 180 degrees out-of-phase relative to the "forward-connected" coil groups. Combining the above factors into a single expression, Oberretl obtains (Reference 1, p. 7)

$$\nu_{k_w} = \frac{\sin\frac{P}{2}\nu mq\alpha}{\sin\nu mq\alpha} \sin\frac{\nu mq\alpha}{2} \cdot \frac{\sin q\nu\alpha/2}{\sin\nu\alpha/2} \cdot \sin\frac{\nu mq - \varepsilon}{2} \alpha \frac{\sin m(\nu q\alpha - \pi/m)}{\sin(\nu q\alpha - \pi/m)} \quad (4)$$

The above equation is not valid for a LIM with odd numbers of poles since it gives infinitely large ν_{k_w} values when $\nu mq\alpha \to \pi$.

An alternate expression for the winding factor which is valid for both even and odd numbers of motor poles can be derived by summing the mmf contributions first within a pole pitch and next over the number of half-wavelength contributions comprising the motor. Thus summing the coil groups within a pole pitch gives

$$\sum_{k=1}^{m} e^{j\left[-(k-1)\frac{\pi}{m} + \nu(k-1)q\alpha\right]} = \frac{\sin\frac{m}{2}(\nu q\alpha - \pi/m)}{\sin\left(\frac{\nu q\alpha - \pi/m}{2}\right)} \cdot e^{j\frac{(m-1)}{2}\left(\nu q\alpha - \frac{\pi}{m}\right)}$$

and summing the respective pole-pitch contributions over the entire length of the motor yields

$$\sum_{\rho=1}^{P} e^{j\left[\nu(\rho-1)mq\alpha + (\rho-1)\pi\right]} = \frac{\sin P\frac{\nu mq\alpha - \pi}{2}}{\sin\frac{\nu mq\alpha - \pi}{2}} \cdot e^{j(P-1)\left(\frac{\nu mq\alpha - \pi}{2}\right)}$$

This leads to the following expression for the winding factor

$$\nu_{k_w} = \frac{\sin P\frac{\nu mq\alpha - \pi}{2}}{\sin\frac{\nu mq\alpha - \pi}{2}} \cdot \frac{\sin q\nu\alpha/2}{\sin\nu\alpha/2} \cdot \sin\frac{\nu mq - \varepsilon}{2} \alpha \frac{\sin m\frac{\nu q\alpha - \pi/m}{2}}{\sin\frac{\nu q\alpha - \pi/m}{2}} \quad (5)$$

Equation 5 was used instead of Equation 4 to compute the primary mmf in the Oberretl computer program developed as part of this study.

2.1.1.3 Primary Harmonic Current Distribution

The Oberretl model substitutes for the actual primary current distribution in the stator, an effective current density (sheet), $\alpha_z(x,z)$, given by

$$\alpha_z(x,z) = \sum_n \sum_\nu J(\nu,n) \cos\frac{n\pi z}{L} e^{j\left(\omega t - \nu x\frac{2\pi}{\ell} + \frac{\pi}{m}\right)} \qquad (6)$$

where $J(\nu,n)$ is the amplitude of the Fourier current harmonic for transverse (z-directed) currents, ℓ and L are the length and width respectively of the "unit periodic cell", and ν and n and the respective harmonic orders along the longitudinal are transverse wave vector directions. The harmonic amplitude, $J(\nu,n)$, is given explicitly by

$$J(\nu,n) = \frac{16\ NI_1\sqrt{2}\ {}^{\nu}k_w\ n_y}{\pi\ell}. \qquad (7)$$

Here ${}^{\nu}k_w$ is the winding factor for the νth harmonic, $N\ I_1$ the ampere-turns in a single stator slot, and ${}^{n}y$ the amplitude of the transverse dependence of the mmf-distribution.

A. $J(\nu,n)$ dependence on longitudinal harmonic order, ν.

The variation of $J(\nu,n)$ with longitudinal harmonic order is presented in Figure 3 (solid curve) using the motor parameters listed in Section 2.2.1. For the purpose of calculation, the transverse harmonic order, n, was set equal to 1. For the choice of gap length, ℓ_ℓ = 33.212 meters, the peak Fourier harmonic at ν_5 = 198. (197.5) and the effective 7th Fourier harmonic at ν_7 = 277 (276.5). It is interesting to compare the Oberretl harmonic current density function (Equation 7) with the Fourier transform of a single harmonic wave,

$$J(k) = J_1 \frac{\sin\left((k - k_o)\ell_s\right)}{k - k_o}, \qquad (8)$$

ℓ_s is the distributed length of the current density wave, k the independent wave propagation number equivalent to $\nu mq\alpha/\tau_p$ in the Oberretl model, and k_o the propagation number of the wave equal

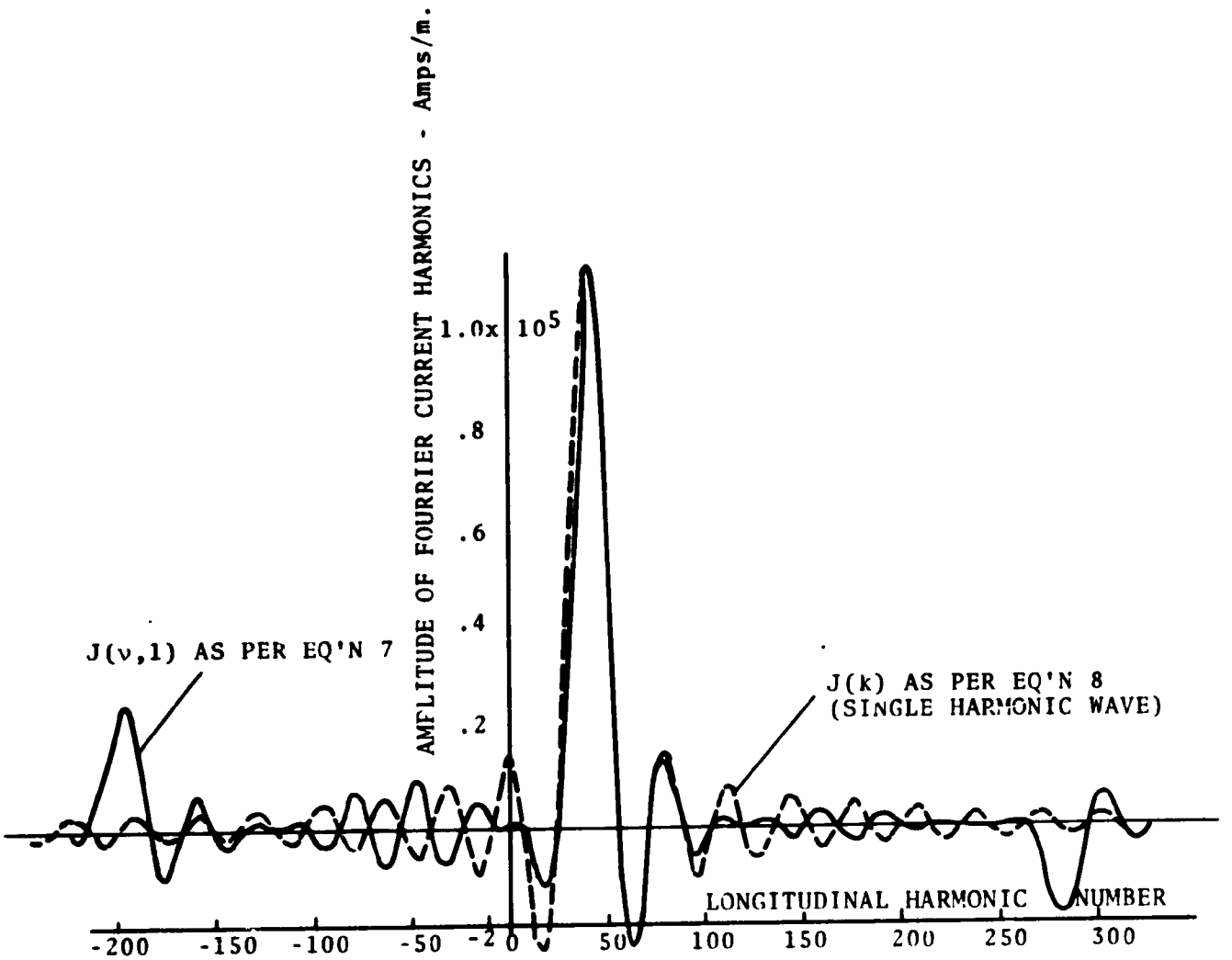

FIGURE 3. PRIMARY CURRENT HARMONIC SPECTRUM OF TLRV LIM AS COMPUTED BY OBERRETL THEORY

to π/τ_p. Setting k_o equal to the wave number of maximum $J(\nu,n)$ in Figure 3 and ℓ_s equal to the effective length of the TLRV stator ($\ell_s = P\tau_p$), the dashed curve shown in Figure 3 is obtained for the harmonic current distribution J_1 in Equation 8 was normalized to the peak amplitude computed from Equation 7. Figure 3 shows that the harmonic spectrum derived from a single-harmonic wave represents a fair approximation to $J(\nu,1)$ in the spectrum region of the principal harmonic contribution, i.e., $10<\nu<70$. Since the contribution of the higher-order harmonics to the LIM reaction forces is comparatively small, the stress tensor components evaluated using the single harmonic transformation (Equation 8) should not be significantly different from those evaluated using the multi-harmonic transform function (Equation 7). Since Yamamura and Oberretl use Equations 8 and 7 respectively to describe the primary harmonic current spectrum, a comparison of the reaction forces computed using the two methods should indicate whether the above conclusion is valid.

B. J(ν,n) dependence on transverse harmonic order, n.

The Oberretl model assumes the primary current density to vary with transverse displacement as shown in the sketch below. For z-positions within the confines of the primary, i.e., $-c \leq z \leq c$, the primary current density is constant. Beyond the primary edge, the current density decays to zero in a distance h according to $1 - \sin\frac{(z-c)\pi}{2h}$ and remains zero in the regions defined by $c+h \leq |z| \leq L/2$. Oberetl indicates this choice of z-functional dependence for the primary current is somewhat arbitrary and other functional dependences could be used in its place, provided they are consistent with results of field measurements.

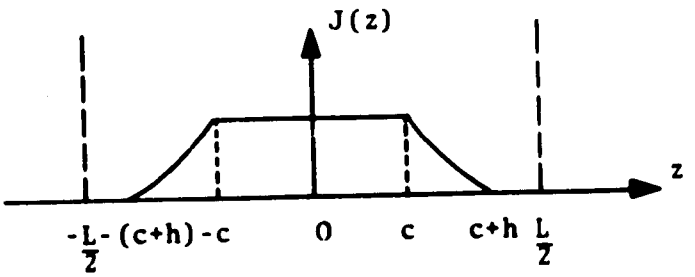

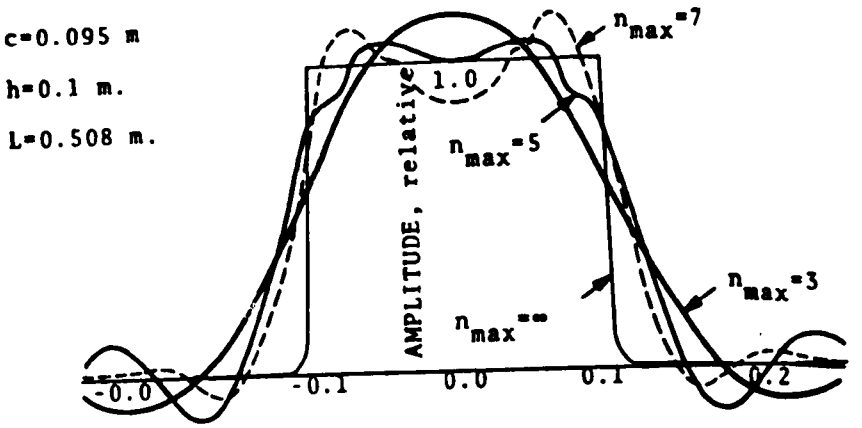

FIGURE 4. TRANSVERSE CURRENT DISTRIBUTION OF TLRV LIM AS COMPUTED BY OBERRETL THEORY

Oberretl expresses the above current distribution in terms of the Fourier Series

$$\theta(z) = \frac{4}{\pi} \sum_{n} \left\{ \frac{\left(\frac{L}{2h}\right)^2}{\left(\frac{L}{2h}\right)^2 - n^2} \left[\frac{1}{n} \sin \pi n \frac{(c+h)}{L} - \frac{2h}{L} \cos \pi n \frac{c}{L} \right] \right\} \cos n\pi \frac{z}{L} \quad (9)$$

$n = 1, 3, 5, \ldots$

where the term in brackets {} corresponds to n_y in Equation 7. Figure 4 shows a sketch of $\theta(z)$ as a function of the transverse displacement along the z axis for increasing values of maximum harmonic order, n_{max}, for the TLRV LIM. The larger the value of n_{max}, the better the approximation to the "ideal" current distribution function corresponding to $n_{max}=\infty$. Large n_{max}, however, results in excessive computing time and a compromise is necessary between computational costs and the relative "accuracy" of the current distribution function. In the TLRV and LIMRV LIM calculations described later in the report, n_{max} was chosen equal to the

value used by Oberretl in his LIM calculations, namely, $n_{max}=5$.

The use of a two-dimensional Fourier representation to describe the primary current causes the propagation vector in the secondary along the normal direction to be a function of both longitudinal and transverse wave numbers. This appears to be the basis for the Oberretl claim to a three-dimensional model. It leads to a reduction in the dependence of computed thrust on the longitudinal harmonic number only, which in the case of the Yamamura theory (Reference 2, p. 98) results in oscillatory type behavior in the thrust-versus-slip characteristics of high speed LIMs near small motor slips.

2.1.1.4 Thrust Harmonic Amplitude Distribution

The LIM thrust in the Oberretl model is found by summing harmonic thrust contributions over the longitudinal (ν) and transverse (n) harmonic wave orders. If $F(\nu,n)$ is the amplitude of the ν, nth thrust harmonic, the LIM thrust is given by

$$F_x = \sum_{\nu} \sum_{n} F(\nu,n)$$

where

$$F(\nu,n) = \frac{L\ell^2 \lambda \mu_o}{8\pi\nu} J_1^2(\nu,n) \quad \frac{\mathrm{Im}(C_{12})}{|\sinh\lambda g + C_{12}\cosh\lambda g|^2} \tag{10a}$$

$$C_{12} = \frac{\sqrt{\lambda^2 + j\omega\mu_2\sigma_2 {}^{\nu}s}}{\lambda\mu_{02}} \tanh\left(\sqrt{\lambda^2 + j\omega\mu_2\sigma_2 {}^{\nu}s}\ \frac{b}{2}\right) . \tag{10b}$$

λ is the wave number in the airgap along the normal direction, σ_2 is the conductivity in the secondary, μ_2 is the permeability of the secondary equal to $\mu_2=\mu_{o2}\mu_o$, and ${}^{\nu}s$ is the harmonic slip given by ${}^{\nu}s=1-\nu(1-s)mq\alpha/\pi$.

Figure 5 presents a plot of Equation 10 as a function of longitudinal order (ν) for the TLRV LIM at line frequencies of

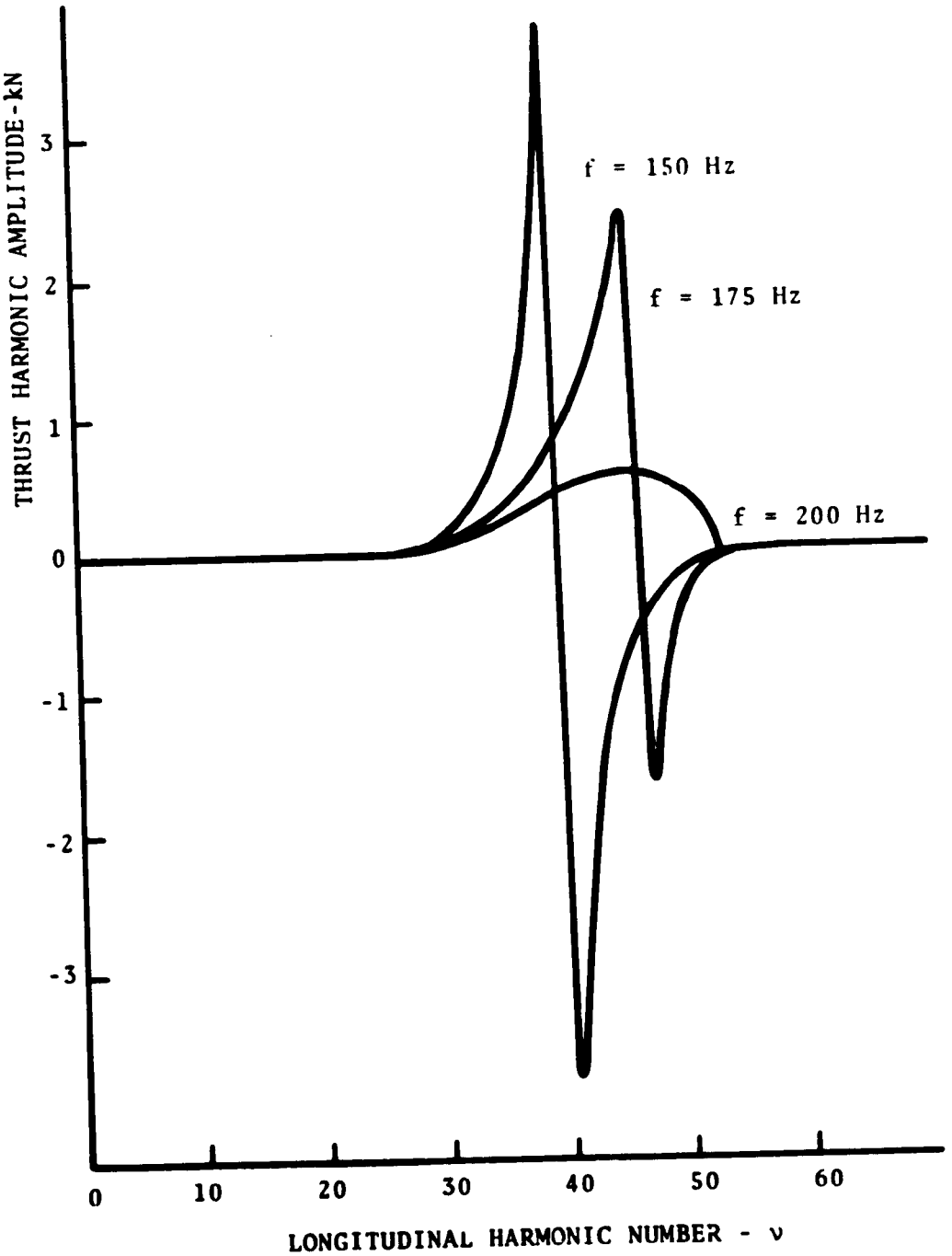

FIGURE 5. THRUST HARMONIC SPECTRUM OF TLRV LIM AS COMPUTED BY OBERRETL THEORY

150, 175, and 200 Hz. For purposes of calculation, the transverse harmonic order was set equal to unity. Motor speed was fixed at 300 mph and line current at 530 amperes corresponding to conditions assumed in the later TLRV LIM calculations. The remaining TLRV parameters used to compute $F(\nu,n)$ are given in Table 1. The figure illustrates several features of the harmonic thrust function.[5] First, $F(\nu,n)$ is large only within a limited range of longitudinal harmonic orders centering on the principal harmonic order ν_o associated with the fundamental wave number. In this example of the TLRV LIM, the principal harmonic order $\nu_o \approx 40$ corresponds to the peak current density as shown in Figure 3. Second, $F(\nu,n)$ is zero at periodic values of longitudinal harmonic order since $J(\nu,n) = 0$ for $\nu = \nu_o(1 \pm 2m/P)$, $(m=1,2,3,..)$. Third, $F(\nu,n)$ shows a rapid change at the singular point $\nu = \nu_o/(1 - \text{slip})$. Special care must be exercised in the numerical integration of $F(\nu,n)$ in the region of the singularity, particularly at frequencies near zero motor slip. Iwamoto[5] suggests the use of finite difference methods for improving the accuracy of the numerical integration in the region of the singularity.

2.1.1.5 Airgap Flux Density

The LIM flux density distribution in the Oberretl theory is described by an infinite Fourier series of spatial harmonics along the longitudinal and transverse axes of the motor. The components of flux density at the surface of the secondary can be written in the form

$$B_x = \sum_{\nu} \sum_{n} B_o(\nu,n)\, C_{12}\, \cos k_z z\; e^{-j(k_x x - \omega t)} \tag{11}$$

$$B_y = j \sum_{\nu} \sum_{n} \frac{\lambda}{k_x} B_o(\nu,n)\, \cos k_z z\; e^{-j(k_x x - \omega t)} \tag{12}$$

$$B_z = -j \sum_{\nu} \sum_{n} \frac{k_z}{k_x} B_o(\nu,n)\ C_{12}\ \sin k_z z\ e^{-j(k_x x - \omega t)} \qquad (13)$$

where

$$B_o(\nu,n) = \mu_o \frac{16N\ I_1 \sqrt{2}\ \nu k_w\ n_y}{\pi \ell_s (\sinh\lambda g + C_{12}\cosh\lambda g)}$$

and k_x, k_z are the wave number components along the x,z axes respectively, i.e., $k_x = \nu 2\pi/\ell, k_z = n\pi/L$. C_{12} is defined in Equation 10b.

The flux density components defined by Equations 11 through 13 determine the stress tensor components evaluated at the surface of the secondary. Therefore, the correctness with which these equations describe the flux density in an actual LIM is critical to an accurate calculation of LIM forces. A comparison of the computed flux density components with that obtained from flux mapping in the motor airgap offers a check on the effectiveness of the LIM model to represent an actual LIM.

Figure 6 gives the airgap flux density computed as a function of displacement distance along the transverse axis using parameters appropriate to the TLRV LIM. Motor speed was taken as 300 mph and line frequency as 200 Hz. Three curves are presented corresponding to three different values of maximum transverse harmonic number n_{max}. The curves show that the flux density tends to peak inside the primary region with increasing n_{max}, with the position of maximum flux density occurring near the inside edges of the primary. For n_{max}=17, the flux distribution approaches the form predicted by Bolton[4] for DLIMs with symmetric secondaries. The additional peak in flux density which occurs outside the region of the primary is disturbing, since in actual LIMs the flux density tends to decay monotonically with distance from the stator edges. The exact reason for the second peak in the computed flux distribution is not known, but it might be associated with the assumption of a continuous ferromagnetic region in the primary. Its existence raises questions regarding the ability of the

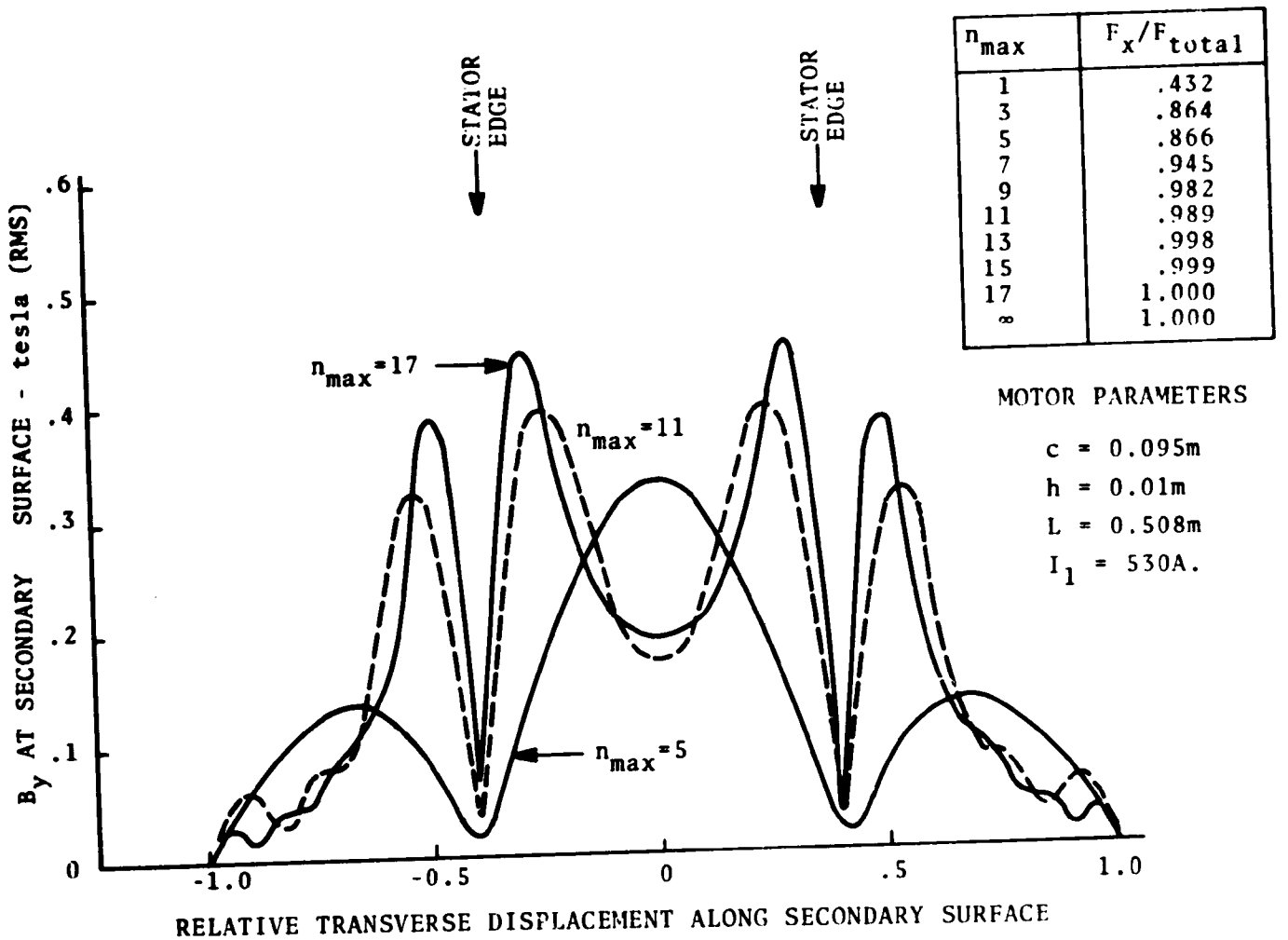

n_{max}	F_x/F_{total}
1	.432
3	.864
5	.866
7	.945
9	.982
11	.989
13	.998
15	.999
17	1.000
∞	1.000

MOTOR PARAMETERS

c = 0.095m

h = 0.01m

L = 0.508m

I_1 = 530A.

FIGURE 6. TLRV FLUX DENSITY ALONG TRANSVERSE AXIS COMPUTED USING OBERRETL THEORY

Oberretl model to describe accurately effects related to the finite width of the motor.

The ratio of thrust for increasing n_{max} values normalized to the thrust for n_{max}=25 is shown in tabular form in Figure 6. The table shows an increase in computed thrust with increase in n_{max} for this LIM example; at n_{max}=7, the thrust is 95 percent of the value computed for n_{max}=25. In view of the irregular behavior of the flux density distribution along the transverse axis and dependence on n_{max}, it is not clear whether the thrust is computed with greater accuracy when n_{max} is larger as compared with n_{max} of a smaller specified value.

2.1.2 Application of Oberretl Computer Model to TLRV & LIMRV LIMs

The following sections summarize results of computer studies of TLRV and LIMRV motors, using a computer program based on the Oberretl model. All computations were performed using the PDP-10 Computer located at the Transportation Systems Center, Cambridge, Massachusetts. Computer times required for typical runs comprising ten cases (variable slip or frequency) were of the order of 60 seconds.

2.1.2.1 TLRV Linear Induction Motor

The TLRV thrust and normal forces were computed for a fixed input line current of 700 amperes and motor speed of 300 mph (134.1 m/s). The motor parameters used in the calculations are given below. The dimensions of the motor 'unit cell' forming the basis for the two-dimensional periodic array are shown in Figure 7. The longitudinal and transverse mmf gap lengths were taken respectively at 33.212 and 0.199 meters. Longitudinal (ν) harmonics were summed over the range $-120 \leq \nu \leq 120$. Transverse (n) harmonics were summed from n = 1 to 5, i.e., n = 1, 3, and 5.

TABLE 1. TLRV LIM PARAMETERS IN OBERRETL MODEL

Turns per Coil (N) = 4
Pole Pitch (τ_p) = .448 m.
Core Width (2c) = .1905 m.
Poles (P) = 5
Core Length (ℓ_s) = 2.56 m.
Air Gap (g) = .0171 m.*
Phases (m) = 3
Slots per Phase (q) = 5
End Half-filled Slots (ε) = 5
Secondary Thickness (b) = .0066 m.
Secondary Resistivity (ρ) = $.416 \times 10^{-7}$ ohm-m.
Coil Overhang (h) = .01 m.
Longitudinal MMF Gap (ℓ_s) = 33.212 m.
Transverse MMF Gap = .199 m.
Longitudinal Periodic Wavelength = 35.772 m.
Transverse Periodic Half-wavelength (L) = 54 m.
Motor Speed (V) = 134.1 m/s

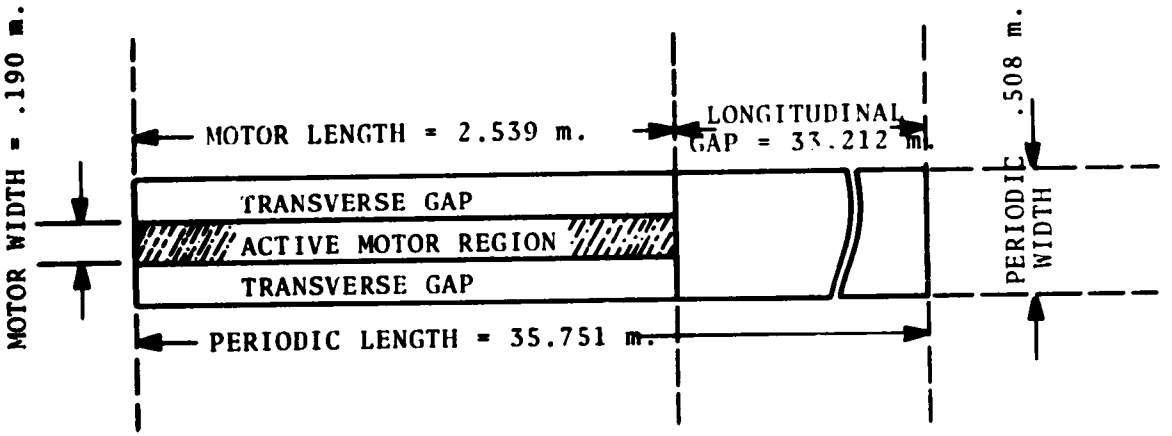

FIGURE 7. OBERRETL UNIT CELL USED IN TLRV LIM CALCULATIONS

2.1.2.2 TLRV Thrust-Frequency Characteristic

The TLRV thrust computed for frequencies in the range of 155 to 200 Hz is shown, in Figure 8. The corresponding thrust predicted by the mesh-matrix model[8] is also presented for comparison. The thrusts computed using the Oberretl model are about one-third larger than those computed by Elliott. The choice of longitudinal mmf gap length was sufficiently long to insure effective damping of the end-effect wave inside the periodic length defined by the "unit cell" of the motor.

It is interesting to speculate on the reasons for the divergent thrust predictions. The computer analysis of Elliott includes current and magnetic end-effects and assumes finite lengths for both the mmf and primary ferromagnetic regions. In contrast, the Oberretl analysis neglects ferromagnetic end-effects; however, as Yamamura (Reference 2, p. 67) points out, this should have a relatively small effect on the value of computed thrust. In the Fourier series representation of primary mmf, only three harmonic terms were included in the summation of transverse wave numbers, i.e., n = 1, 3, 5, in the Oberretl computer program. If additional harmonic terms had been included in the summation, it is likely that the thrust predicted by Oberretl would increase slightly since thrust is directly proportional to $(^{n}y)^{2}$ or the square of the transverse harmonic amplitude defined by Equation 2. This, however, would cause the Oberretl-Elliott thrust predictions to diverge even more than indicated in Figure 8.

2.1.2.3 TLRV Normal Force-Frequency Characteristic

The corresponding normal forces computed as a function of frequency are shown in Figure 9 for the TLRV. The mesh-matrix predictions for the same conditions are indicated by the dashed curve. Both results predict a zero force crossover frequency near 190 Hz. Oberretl's theory gives considerably larger normal forces than does the mesh-matrix model at frequencies below the crossover point. Such a large discrepancy in predicted forces is believed associated with the failure of the Oberretl theory ("infinite

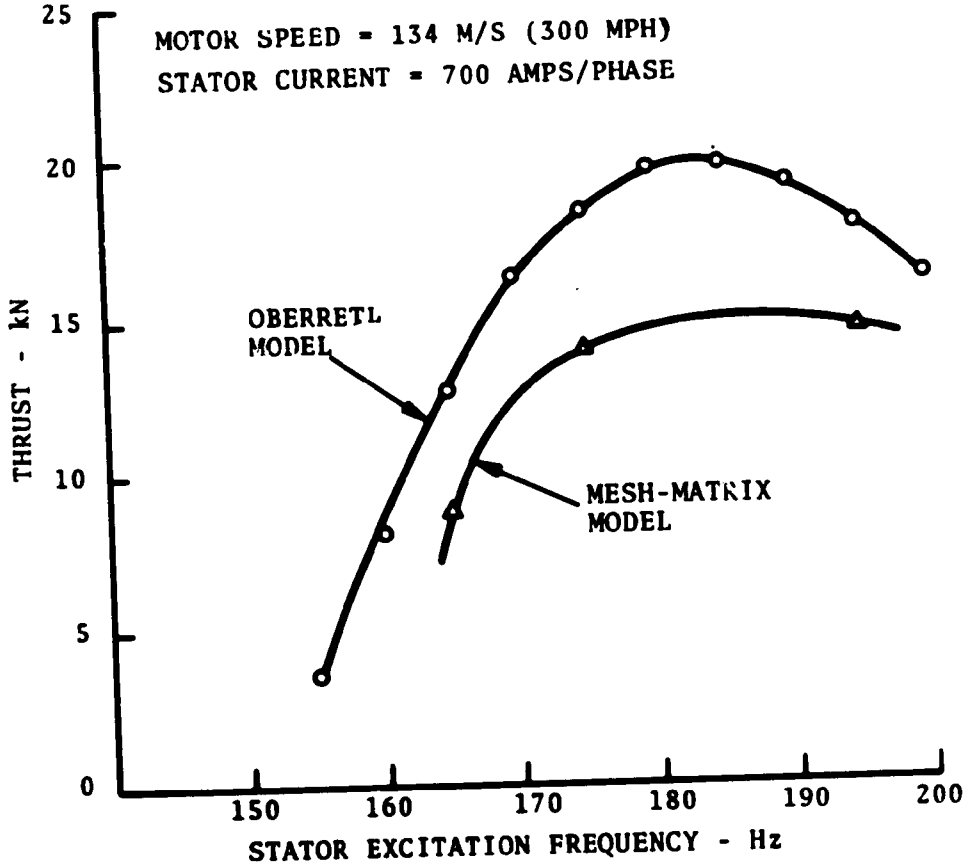

FIGURE 8. TLRV LIM THRUST AS PREDICTED BY OBERRETL THEORY

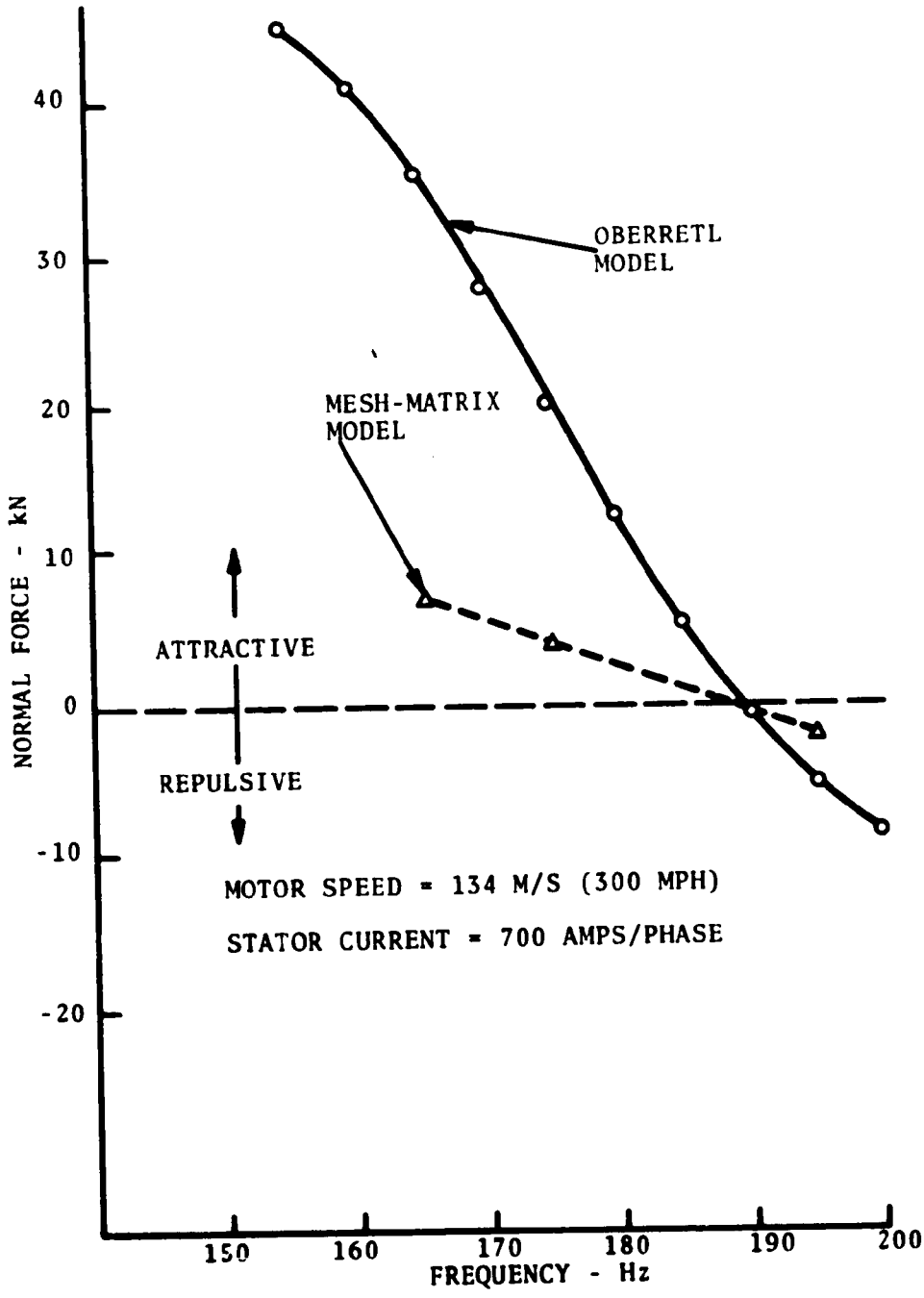

FIGURE 9. TLRV LIM NORMAL FORCE AS PREDICTED BY OBERRETL THEORY

iron") to include the effect of finite primary ferromagnetic region in the LIM model. This causes the Oberretl theory to overestimate the normal attractive force component as a result of overestimating the trailing end-effect wave and edge-effect flux along the sides of the motor

It is helpful in understanding the origin of the large normal forces to attempt a rough calculation of the attractive component of normal force at zero slip, where it is maximum and the predominant component of normal force. The magnetic force can be expressed in terms of the normal component of flux density, B_y.

$$F_n = \frac{1}{2\mu_o} (B_y)^2_{ave} \text{ Newtons/meter}^2. \tag{14}$$

The airgap flux density is given approximately by

$$B_y = \frac{\mu_o N I_1 \sqrt{2}}{g} q \cdot \frac{3}{2} 1.11 \, e^{j(\omega t - kx)}. \tag{15}$$

If one assumes the airgap flux density to be reduced by the end-effect by a factor of two when averaged over the length of the motor, then Equation 14 gives for the normal attractive force,

$$F_n = 11.7 \text{ kN (attractive)}. \tag{16}$$

This compares closely with the value of attractive normal force computed by Elliott for a frequency of 165 Hz equal to 9.35 kilonewtons. The Oberretl theory yields a considerably larger value of normal (predominantly attractive) force near zero slip equal to approximately 26 kilonewtons, or 2-1/2 times that of Elliott. This latter is explicable if one assumes the end-effect wave in the mmf gap region contributes a normal force component equal to that contributed by the active motor region.

2.1.2.4 LIMRV Linear Induction Motor

The LIMRV thrust and normal forces were computed for a fixed input line current of 2400 amps and motor speed of 250 mph (112 m/s). The relevant motor parameters used in the calculations are listed below. The dimensions defining the motor 'unit cell' are

given in Figure 10. The longitudinal and transverse mmf gap lengths were chosen respectively equal to 11.096 and 0.150 meters. The longitudinal gap length was equal to about 1-1/2 times the estimated decay length at 165 Hz computed using Equation 1. Longitudinal harmonics were summed over the range $-50 \leq \nu \leq 50$. Transverse harmonics were summed from n = 1 to 5, or n = 1, 3, and 5. The choice of maximum longitudinal harmonic number of 50 was adequate to include the significant components of Fourier current harmonic since the main current harmonics centered closely about $\nu = 21$ (20 9).

TABLE 2. LIMRV LIM PARAMETERS IN OBERRETL MODEL

Turns per Coil (N) = 1
Pole Pitch (τ_p) = .355 m.
Core Width (2c) = .254 m.
Poles (P) = 10
Core Length (ℓ_s) = 3.81 m.
Air Gap (g) = .024 m.*
Phases (m) = 3
Slots per Phase (q) = 5
End Half-filled Slots (ε) = 5
Secondary Thickness (b) = .0071 m.
Secondary Resistivity (ρ) = 0.416×10^{-7} ohm-m.
Coil Overhang (h) = .01
Longitudinal MMF Gap (ℓ_g) = 11.096 m.
Transverse MMF Gap = .150 m.
Longitudinal Periodic Wavelength = 14.906 m.
Transverse Periodic Half-wavelength (L) = .554 m.
Motor Speed (V) = 112 m/s

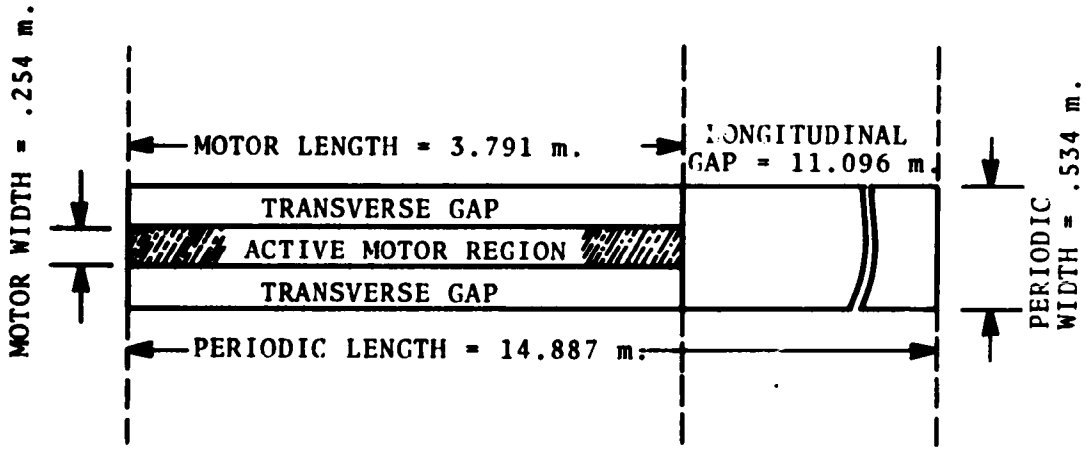

FIGURE 10. OBERRETL UNIT CELL USED IN LIMRV LIM CALCULATIONS

2.1.2.5 LIMRV Thrust-Frequency Characteristic

The LIMRV thrust characteristics were computed for pole gap separations of 38.1 mm and 47.6 mm for frequencies ranging from 160 to 200 Hz. Figure 11 summarizes the results of the calculations given by the solid curves. The dashed curve presents the corresponding thrust prediction by the mesh-matrix model for a pole gap separation of 47.6 mm.

The agreement of the computed thrusts predicted by the Oberretl and mesh-matrix models is good for the case of pole gap separation equal to 47.6 mm. When compared with the corresponding results for the TLRV thrust (Figure 8), the predicted thrusts are in considerable better agreement for the LIMRV than for the TLRV motor. This can probably be attributed to the larger number of poles and lower operating speed of the LIMRV compared with the TLRV; i.e., end-effects in the LIMRV are less pronounced than in the TLRV.

The change of thrust with pole gap separation is governed by two factors. If end-effects can be neglected (which they cannot in the present case), then the thrust must increase with reduced gap separation, since the airgap flux density must increase with smaller gap separations while holding primary current fixed. The situation is more complicated with end-effect present, however, since reducing the gap separation tends to enhance the end-effect wave. Note that the attenuation constant of the end-effect wave decreases with reduced gap separations. (Reference 2, P. 26.) The relative importance of these factors will determine the direction in which the thrust will vary with change in pole gap separation. For the thrust to decrease with decrease in gap separation, the end-effect wave must dominate the driven wave in the airgap region of the motor.

2.1.2.6 LIMRV Normal Force-Frequency Characteristic

The corresponding normal forces computed for the LIMRV are shown in Figure 12 for the Oberretl model (solid curves) and the mesh-matrix model (dashed curve). As in the case of the TLRV

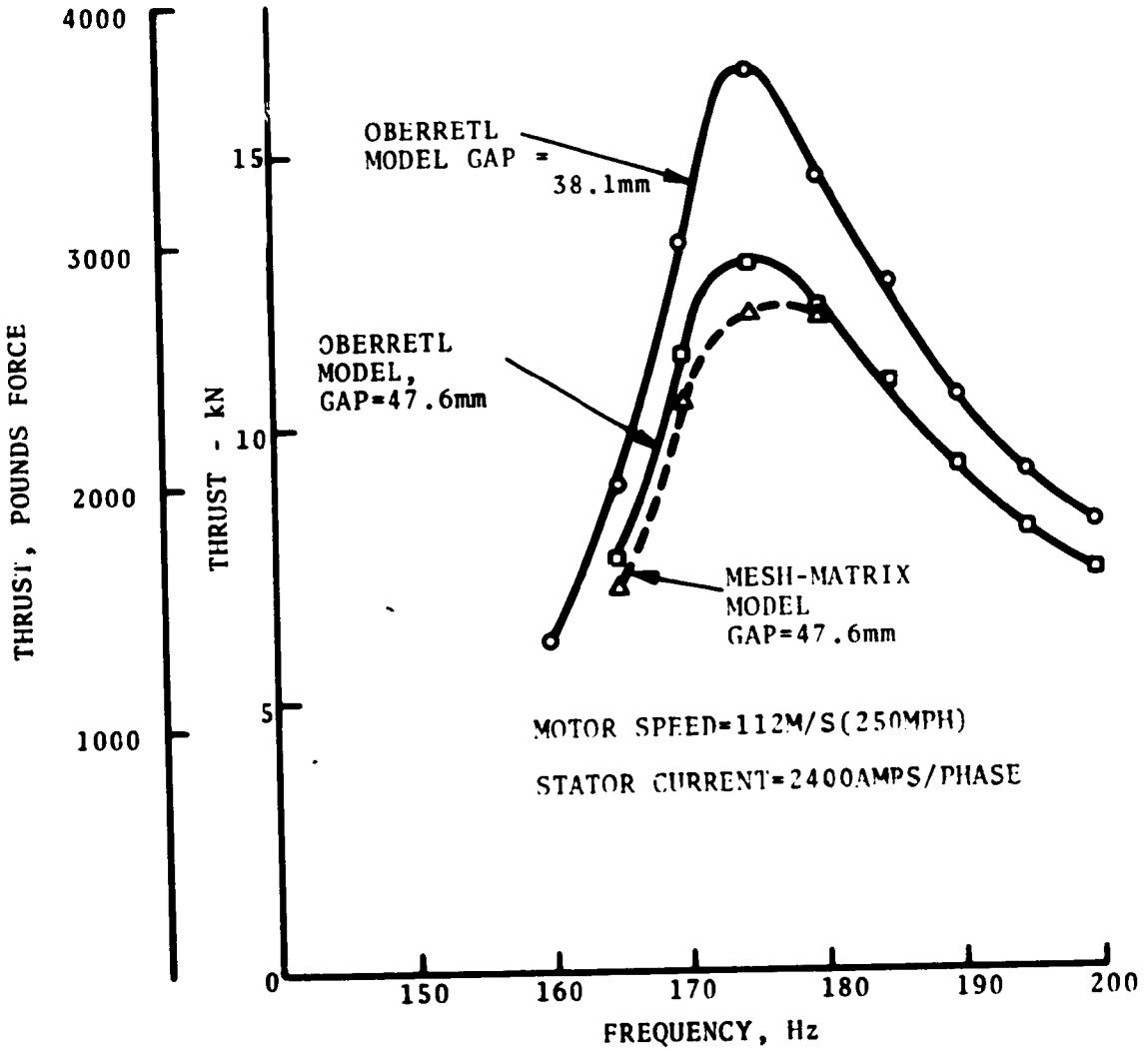

FIGURE 11. LIMRV LIM THRUST AS PREDICTED BY OBERRETL THEORY

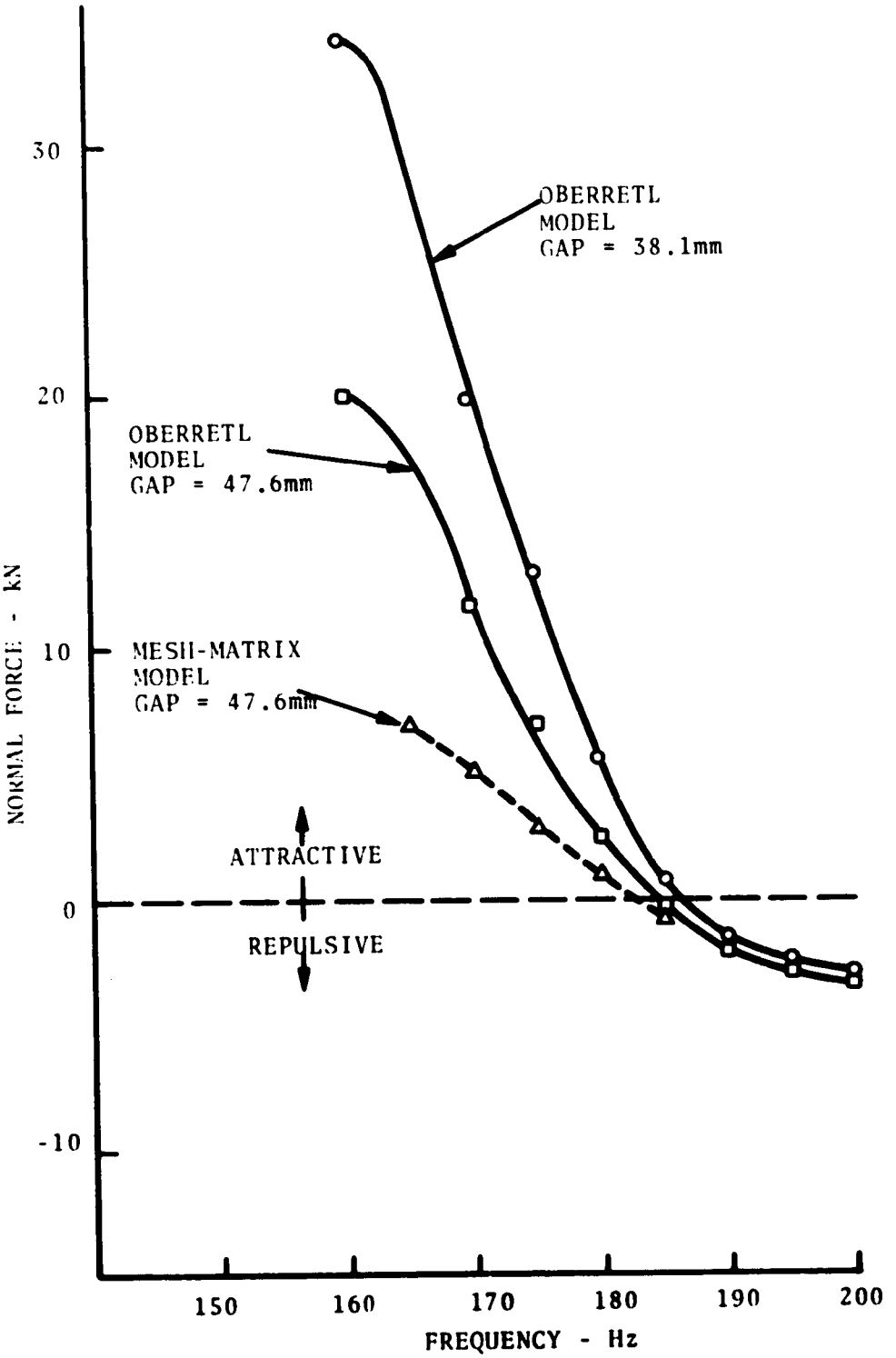

FIGURE 12. LIMRV NORMAL FORCE AS PREDICTED BY OBERRETL THEORY

LIM, the Oberretl theory predicts larger normal forces than does the mesh-matrix theory. The conclusions derived from the study of the TLRV force characteristics apply here as well; namely, the Oberretl theory over-estimates the normal forces at low slip frequencies (below the zero force crossover frequency) due to its neglect of magnetic end-effects.

A calculation of the attractive component of normal force, similar to that undertaken for the TLRV, is also appropriate here in order to estimate its magnitude near zero slip. Using Equation 14 and assuming a line current of 2400 amps, pole gap separation distance of 47.6 mm, the estimated attractive component of normal force at zero slip is 6.2 kilonewtons. This compares closely with the value of attractive force component predicted by the mesh-matrix model at 165 Hz.

2.1.3 Summary of Oberretl Theory Applied to TLRV & LIMRV LIMs

A computer model was developed based on the Oberretl LIM theory and applied to estimate the thrust and normal forces in the TLRV and LIMRV LIMs. The computed thrusts were in good agreement with those given by the mesh-matrix model for the LIMRV but, were about 20 percent greater than those given by the mesh-matrix model for the TLRV. The somewhat poorer agreement in the case of the TLRV LIM is attributed to the fact that end-effect is more prominant in the TLRV, due to its higher speed and reduced number of electrical poles.

The normal forces computed with the Oberretl program were consistently greater than those given by the mesh-matrix model at frequencies below the zero-force-crossover frequency. Estimates of the normal force at zero slip proved more consistent with that predicted by the mesh-matrix model than with that predicted by the Oberretl model. This is expected since the Oberretl model assumes a continuous ferromagnetic primary region which leads to excessively large flux densities in the trailing end of the LIM at high motor speeds.

The Oberretl analysis makes no allowance for the finite length of the primary ferromagnetic region. It therefore neglects magnetic end-effects and treats only end-effects related to a finite primary current distribution. A similar approach is undertaken by Yamamura[2] using a Fourier transform method instead of the Fourier Series representation of Oberretl. Yamamura sums the stress tensor (or JxB) component, evaluated at the primary surface, over the length of the primary while Oberretl sums the stress tensor components, evaluated at the secondary surface, over the length of the motor unit cell. Both methods should, in principle, give equivalent results. In considering the effect of finite LIM width, Yamamura uses the results of Bolton's treatment of edge-effects[4] to correct his answer for finite width of the primary current excitation. The Oberretl approach is different in that edge-effects are brought into the treatment in the same manner as are end-effects: namely, by describing the current and

field spatial distributions in terms of a series of two-dimensional spatial harmonics. It is seen that the Oberretl method leads to unreasonable predictions for the flux densities in the regions outside of the edges of the motor for the LIM example examined in this report. The Oberretl treatment of edge-effects bears closer scrutiny in order to assess its implications in the evaluation of LIM reaction forces.

The Oberretl treatment is limited to LIMs with even numbers of poles. This limitation can be traced to the winding distribution factor, which has been derived for even pole numbers. An alternate expression for the winding factor is given in this report, which is believed to correctly describe the mmf distribution of primaries comprising both even and odd numbers of poles.

2.2 THE YAMAMURA THEORY OF THE LINEAR INDUCTION MOTOR

2.2.1 The Yamamura LIM Model[2]

The model for the two-dimensional analysis (neglecting edge-effects) is shown in Figure 13 with coordinate axes as indicated in the figure. The model is divided into three regions along the y-direction and into three zones along the x-direction. Region 1 is the iron core (primary), Region 2 is the secondary conductive sheet, and Region 3 is the air gap separating primary and secondary.

The assumptions appropriate to the Yamamura LIM model are:

a. The field is uniform in the z-direction and all variables are independent of z, i.e., $d(\ )/dz=0$.

b. The stator windings are approximated by sinusoidally traveling surface current sheets existing between x=0 and x=L of the stator core surface.

$$j_1 = J_1 e^{j(\omega t - kx)} \tag{17}$$

Winding slot perturbations and effect of three-phase stator current unbalance are ignored.

c. The stator core extends to infinity in both directions of x-coordinate and has permeability $\mu >> \mu_0$. Magnetic end-effects are neglected.

The Yamamura treatment considers spatial variations of current and flux density only along the x- and y-directions. Since primary current flows in the z-direction, $\bar{B}$ and $\bar{H}$ have x and y components but no z component. The formulation of the electrodynamic problem begins with Maxwell's equations using a flux density, $\bar{B}$, derived from the vector potential, $\bar{A}$,

$$\bar{B} = \nabla \times \bar{A} \tag{18}$$

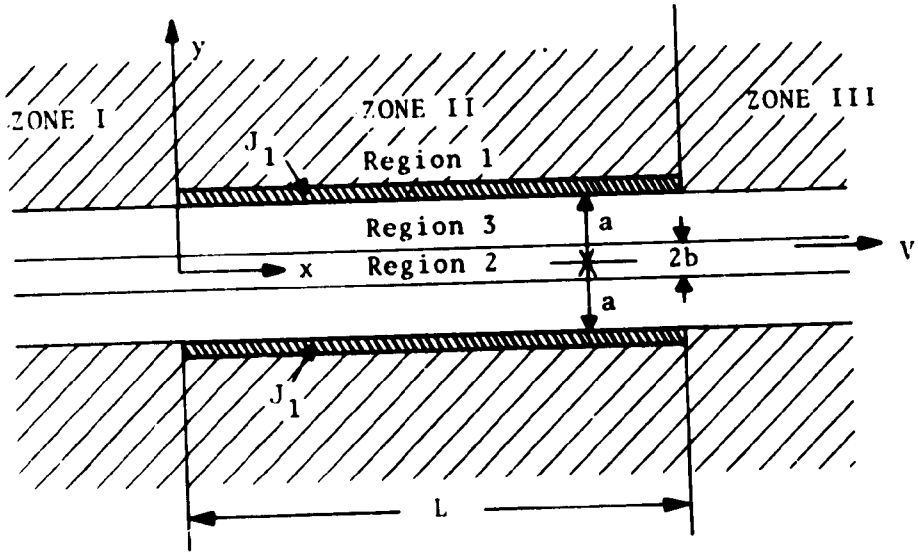

FIGURE 13. YAMAMURA MODEL FOR TWO-DIMENSIONAL LIM ANALYSIS

and

$$\nabla \cdot \bar{A} = 0$$

The general field equation expressed in terms of the vector potential then becomes,

$$\nabla^2 A_z = \mu\sigma\left(\frac{\partial A_z}{\partial t} + V\,\frac{\partial A_z}{\partial t}\right) \tag{19}$$

where $\bar{A}$ has only a z component. V is the velocity of the secondary relative to the fixed primary (stator), σ is the electrical conductivity of the rail, and μ its permeability.

The complete solution of the wave equation requires the boundary conditions to be satisfied at each interface of a given zone of the LIM model. Writing Maxwell's equations at the boundary of each region gives the following relations:

$$\frac{B_{1x}}{\mu_1} - \frac{B_{3x}}{\mu_3} = j_1 \qquad \frac{1}{\mu_1}\frac{dA_1}{dy} - \frac{1}{\mu_3}\frac{dA_3}{dy} = j_1 \text{ at } y = \pm a \text{ ZONE II} \tag{20}$$

where j_1 is the surface current density defined by Equation (17).

$$B_{1y} = B_{3y} \qquad \frac{dA_1}{dx} = \frac{dA_3}{dx} \qquad \text{at } y = \pm a \text{ ZONE II} \tag{21}$$

$$\frac{B_{3x}}{\mu_3} = \frac{B_{2x}}{\mu_2} \qquad \frac{1}{\mu_3}\frac{dA_3}{dy} = \frac{1}{\mu_2}\frac{dA_2}{dy} \qquad \text{at } y = \pm b \text{ ZONE II} \tag{22}$$

$$B_{3y} = B_{2y} \qquad \frac{dA_3}{dx} = \frac{dA_2}{dx} \qquad \text{at } y = \pm b \text{ ZONE II} \tag{23}$$

The solution for the vector potential in the airgap region (Region 3) is given by the Fourier transform.

$$A_3(x,y) = \frac{1}{2\pi}\int_{-\infty}^{\infty} \frac{\mu_o \tilde{J}_1\left[\cosh\gamma b\cosh\xi(y-b) + \frac{\gamma}{\xi}\sinh\gamma b\sinh\xi(y-b)\right]}{\xi\cosh\gamma b\sinh\xi(a-b) + \gamma\sinh\gamma b\cosh\xi(a-b)}\, e^{j\xi x} d\xi \tag{24}$$

where

$$\gamma^2 = \xi^2 + j V \mu_2 \sigma_2 \xi + j \omega \mu_2 \sigma_2$$

and $\check{J}_1$ is the transform of the primary current density.

$$\check{J}_1(\xi) = \int_{-\infty}^{\infty} J_1 e^{-jkx} e^{-j\xi x} dx$$

$$= j \frac{J_1 \left(e^{-j(\xi+k)L} - 1 \right)}{\xi + k} \tag{25}$$

The solution of the vector potential transform given by Equation (24) then leads to the LIM thrust and airgap power per unit width in the z direction.

$$F_x = \frac{-1}{2} \int_0^L \mathrm{Re} \left(j_1^*(x) \frac{dA_3}{dx}(x,a) \right) dx \tag{26}$$

$$P_{airgap} = \frac{-1}{2} \int_0^L \mathrm{Re} \left(j\omega A_3^*(x,a) \cdot j_1(x) \right) dx \tag{27}$$

A discussion of the use of theorem of residues to evaluate the vector potential transform is given in the next section.

2.2.1.1 Solution of Vector Potential Integral Using Residue Theorem

The residue theorem states that the integral of an analytic function around a closed contour is equal to the sum of the residues.[2] Thus if f(z) is an analytic function

$$\frac{1}{2\pi i} \int_{\substack{\text{closed} \\ \text{contour}}} f(z)\, dz = \sum \text{residues} \tag{28}$$

The solution for the residues directly follows once the poles of f(z) are found within the specified analytic region.

It is helpful to simplify the form of Equation (24) through the following substitutions:

$$G(\xi,y) = \cosh\gamma b\cosh\xi(y-b) + \frac{\mu_3\gamma}{\mu_2\xi}\sinh\gamma b\sinh\xi(y-b) \tag{29}$$

$$H(\xi) = \cosh\gamma b\sinh\xi(a-b) + \frac{\mu_3\gamma}{\mu_2}\sinh\gamma b\cosh\xi(a-b) . \tag{30}$$

Then the airgap vector potential is given by

$$A_3(x,y) = \frac{j\mu_o}{2\pi}\int_{-\infty}^{\infty} J_1 e^{j\xi x}\ \frac{e^{-j(\xi+k)L}-1}{\xi+k}\ \frac{G(\xi,y)}{H(\xi)}\,d\xi \tag{31}$$

where the poles of f(z) correspond to the roots of

$$(\xi + k)\,H(\xi) = 0 . \tag{32}$$

Equating the three principal roots of Equation (16) to ξ_1, ξ_2, and ξ_3, the residue theorem leads to the following relation for the vector potential in the airgap in Zone 2($0 < x < L$).

$$A_3(x,y) = \mu_o J_1\left[\frac{G(\xi_1,y)e^{j\xi_1 x}}{H(\xi_1)}\frac{}{} + \frac{G(\xi_2,y)e^{j\xi_2 x}}{(\xi_2+k)\left.\frac{dH}{d\xi}\right|_{\xi=\xi_2}} + \frac{G(\xi_3,y)e^{-j(\xi_3+k)L}e^{j\xi_3 x}}{(\xi_3+k)\left.\frac{dH}{d\xi}\right|_{\xi=\xi_3}}\right] . \tag{33}$$

2.2.1.2 Solution of $H(\xi)=0$ via the Newton-Raphson Method[3]

The residues of the vector potential integral described by Equation (26) are found once the roots of Equation (32) have been determined. One root is simply $\xi_1=-k$. An infinite number of additional roots remain, however, corresponding to the solution of the transcendental equation $H(\xi) = 0$. Such an infinite number of roots is characteristic of wave solutions describing the propagation of waves within regions with multi-defined boundaries, as for example, the propagation of electromagnetic and sonic waves inside cylinderical waveguides. Yamamura points out (Reference 2, p. 73) that only two of these infinite number of roots need to be considered in his mathematical treatment, since the other roots lie far from the origin in wave number space and describe waves which are highly attenuated. The justification for this is later born out in the results of Section 2.1.4, in which the thrust evaluated by numerically integrating the "exact" thrust function (described by an infinite number of wave vector roots) is closely equal to the thrust found in the Yamamura method (in which only the dominant roots, ξ_1, ξ_2, ξ_3, are considered).

Yamamura suggests the application of the Newton-Raphson method for evaluating the roots ξ_2 and ξ_3. According to this method, starting with an initial approximation to the root, successive iterations are made leading to increasingly better approximations to the final root. Thus, if ξ' represents the initial estimate of the root given by the thin sheet approximation, the Newton-Raphson method states that the new approximation to the root is obtained by repeated iterations of

$$\xi = \xi' - \frac{H(\xi)}{\left.\frac{dH(\xi)}{d\xi}\right|_{\xi=\xi'}} \qquad (34)$$

Tables 3 and 4 give the roots computed for the TLRV and LIMRV LIMs according to Newton-Raphson method using the motor parameters shown below:

TABLE 3. ROOTS OF $H(\xi) = 0$ FOR TLRV LIM; EDGE-EFFECTS NEGLECTED. LIM SPEED = 500 MPH

Freq. Hz	ξ_1	ξ_2	ξ_3
150	-7.012	-7.02+j0.07	0.21-j262.04
155	-7.012	-7.26+j0.08	0.21-j262.04
160	-7.012	-7.49+j0.08	0.22-j262.04
165	-7.012	-7.73+j0.09	0.23-j262.04
170	-7.012	-7.96+j0.10	0.23-j262.04
175	-7.012	-8.20+j0.10	0.24-j262.04
180	-7.012	-8.43+j0.11	0.25-j262.04
185	-7.012	-8.66+j0.11	0.25-j262.04
190	-7.012	-8.90+j0.12	0.26-j262.04
195	-7.012	-9.13+j0.13	0.27-j262.04
200	-7.012	-9.37+j0.13	0.27-j262.04

TABLE 4. ROOTS OF $H(\xi) = 0$ FOR LIMRV LIM; EDGE-EFFECTS NEGLECTED. LIM SPEED = 250 MPH

Freq. Hz	ξ_1	ξ_2	ξ_3
160	-8.840	-8.99+j0.19	0.25-j186.39
165	-8.840	-9.27+j0.20	0.26-j186.39
170	-8.840	-9.55+j0.21	0.27-j186.39
175	-8.840	-9.83+j0.22	0.27-j186.39
180	-8.840	-10.11+j0.23	0.28-j186.39
185	-8.840	-10.39+j0.25	0.29-j186.39
190	-8.840	-10.67+j0.26	0.30-j186.39
195	-8.840	-10.95+j0.27	0.30-j186.39
200	-8.840	-11.23+j0.29	0.31-j186.39

TABLE 5. TLRV LIM PARAMETERS

Turns per Coil	(N)	=	4
Pole Pitch	(τ_p)	=	0.448 m.
Core Width	(2c)	=	0.1905 m.
Poles	(P)	=	5
Core Length	(ℓ_s)	=	2.56 m.
Air Gap	(g)	=	0.0171 m.
Phases	(m)	=	3
Slots per Phase	(q)	=	5
End Half-filled Slots	(ε)	=	5
Secondary Thickness	(b)	=	.0060 m.
Secondary Resistivity	(ρ)	=	$.416 \times 10^{-7}$ ohm-m.

TABLE 6. LIMRV LIM PARAMETERS

Turns per Coil	(N)	=	1
Pole Pitch	(τ_p)	=	.355 m.
Core Width	(2c)	=	.254 m.
Poles	(P)	=	10
Core Length	(ℓ_s)	=	3.81 m.
Air Gap	(g)	=	.024 m.
Phases	(m)	=	3
Slots per Phase	(q)	=	5
End Half-filled Slots	(ε)	=	5
Secondary Thickness	(b)	=	.0071 m.
Secondary Resistivity	(ρ)	=	0.416×10^{-7} ohm-m.

These roots describe the propagation constants of the three principal waves in Zone II. (See Figure 13.) ξ_1 corresponds to the propagation number of the 'driving'wave, ξ_2 the propagation number of the entrance end-effect wave, and ξ_3 the propagation number of the exit end-effect wave. The large imaginery part of ξ_3 indicates that the exit end-effect is highly damped for both LIM examples. It should, therefore, contribute little to the total LIM thrust.

2.2.1.3 Calculation of Thrust Residues (Edge-Effects Neglected)

The LIM thrust in the Yamamura model is found by substituting Equation (24) in Equation (26) and performing the required integration over the length of the motor. The solution obtained by

Yamamura for the time-average thrust is given in terms of three thrust residue functions, F_1, F_2, F_3.

$$F_x = F_1 + F_2 + F_3$$

where

$$F_1 = \frac{\mu_o}{2} J_1^2 \, \mathrm{Re}\left[\frac{jkLG(-k,a)}{H(-k)}\right] \tag{35}$$

$$F_2 = \frac{\mu_o}{2} J_1^2 \, \mathrm{Re}\left[\xi_2 \frac{\left(1-e^{j(\xi_2+k)L}\right)}{(\xi_1+k)^2 dH/d\xi_{\xi=\xi_2}} G(\xi_2,a)\right] \tag{36}$$

$$F_3 = \frac{\mu_o}{2} J_1^2 \, \mathrm{Re}\left[\xi_3 \frac{e^{-j(\xi_3+k)L}\left(1-e^{j(\xi_3+K)L}\right)}{(\xi_3+k)^2 dH/d\xi_{\xi=\xi_3}} G(\xi_3,a)\right] \tag{37}$$

The three thrust components, F_1, F_2, F_3 describe the thrusts developed by the normal wave, the entrance end-effect wave, and the exit end-effect wave.

The values of these thrust components were computed for the examples of the TLRV and LIMRV LIM's as described by the motor parameters previously given. The computed thrust components for these two motors are presented in Tables 7 and 8 as a function of motor excitation frequency. The tables demonstrate the relatively small magnitude of the exit end-effect thrust component compared to the entrance end-effect thrust component. The magnitude of F_2 increases sharply with decreasing slip frequency and approaches the magnitude of F_1 at zero slip frequency. The data in Table 8 also illustrates the oscillatory-like characteristics of F_2 as a function of slip frequency. The study of thrust residues will be continued in Section 2.2.1 where the effect of finite LIM width on thrust will be examined.

TABLE 7. COMPUTED THRUST "RESIDUES" FOR TLRV LIM; EDGE-EFFECTS NEGLECTED. LIM SPEED = 300 MPH

Freq. Hz	F_1 N.	F_2 N.	F_3 N.	F_x N.
150	9380	-9750	2.74	- 360
155	14100	-13800	2.74	343
160	7730	-6720	2.74	1020
165	5270	-3670	2.74	1600
170	3990	-1930	2.74	2060
175	3210	- 845	2.74	2370
180	2680	- 179	2.74	2510
185	2310	186	2.74	2490
190	2020	333	2.74	2360
195	1800	329	2.74	2130
200	1620	238	2.74	1860

TABLE 8. COMPUTED THRUST "RESIDUES" FOR LIMRV LIM; EDGE-EFFECTS NEGLECTED. LIM SPEED = 250 MPH

Freq. Hz	F_1 N.	F_2 N.	F_3 N.	F_x N.
160	15700	-14500	2.6	1210
165	11100	-7810	2.6	3320
170	7450	-2860	2.6	4590
175	5510	- 619	2.61	4890
180	4360	+ 98.8	2.61	4460
185	3590	+ 81.6	2.61	3680
190	3060	- 120	2.61	2940
195	2660	- 218	2.61	2440
200	2350	- 165	2.61	2190

2.2.1.4 Thrust Calculation: Theorem of Residues-Versus-Numerical Integration Methods

Yamamura applies the theorem of residues to evaluate the magnetic vector potential and subsequently the thrust based on Equation (26). A similar approach is adopted by Iwamoto[4] to compute LIM thrust. However, instead of applying the theorem of residues to evaluate the vector potential integral, he uses a numerical integration approach since it is claimed that the latter approach leads to a "more accurate analysis of the end-effect." This section will examine the two mathematical methods in terms of their computed LIM thrusts.

The Iwamoto expression for the thrust given by Equation (32) of Reference 4 is equivalent to the Yamamura expression for thrust as found by substituting Equation (24) in (26) and replacing the current density with its Fourier transform as given by Equation (38). (Note that the Yamamura thrust is computed for one core side only while the Iwamoto thrust is for both LIM sides.) The Yamamura expression for thrust can be rewritten as

$$F_x = \frac{\mu_o J_1^2}{4\pi} \int_{-\infty}^{\infty} 4\ \mathrm{Re}\left[j\left(\frac{\sin(\xi+k)L}{\xi+k}\right)^2 \frac{\xi G(\xi,a)}{H(\xi)} \right] d\xi \text{ per side} \qquad (38)$$

where $j = \sqrt{-1}$. The integral can be converted to a series format by replacing the variable wave number, ξ, by ν times the wave number increment, $2\pi/\ell$, where ℓ is a periodic length of a "unit cell" forming the basis for the fundamental wave number. Equation (38) then takes the form.

$$F_x = \frac{\mu_o J_1^2}{2\ell} \sum_{\nu} 4\left(\frac{\sin\frac{L}{2}\left(\frac{\nu 2\pi}{\ell} + k\right)}{\frac{\nu 2\pi}{\ell} + k} \right)^2 \mathrm{Re}\left(j\xi \frac{G(\nu)}{H(\nu)} \right) \qquad (39)$$

where ν is summed over $-\infty$ to $+\infty$. The effect of finite primary width is not included in the above equation in its present form.

A comparative study was next undertaken to examine the possible variations in the thrust which result from the application

of the theorem of residues and numerical integration to evaluate the thrust integral. There is the question of the possible errors in the Yamamura thrust, which result from the neglect of the additional residues omitted in the evaluation of the vector potential integral. These additional residues neglected by Yamamura are associated with the multiple poles of $G(\xi,a)/H(\xi)$ which arise from the roots of $H(\xi)$ not located near the origin of the complex plane. A second question relates to possible inaccuracies in the numerical integration method resulting from the integration of the thrust distribution function in the region of the singularity.

Table 9 presents the thrusts computed by the residue method (Yamamura) and the numerical integration method (Iwamoto) for the example of the TLRV LIM operating at 300 mph. The value of the primary current density used in the residue thrust calculation was determined from

$$J_1 = \frac{6\sqrt{2}\,NI_i}{\tau_p}\,\frac{\sin q\alpha/2}{\sin\alpha/2}\,\sin\frac{\alpha'\pi}{2} \tag{40}$$

where τ_p is the slot pitch and α' is the pitch factor equal to 2/3. The remaining parameters associated with the TLRV LIM are given in Table 5. The expression for the primary current density distribution used the numerical integration method is given by

$$J_1(\nu) = \frac{16NI\sqrt{2}\,m}{\pi\ell}\,\frac{\sin\nu q\alpha/2}{\sin\nu\alpha/2}\cdot\frac{\sin P\left(\frac{\nu mq\alpha-\pi}{2}\right)}{2\sin\left(\frac{\nu mq\alpha-\pi}{2}\right)}\cdot\sin\frac{\alpha'\pi}{2} \tag{41}$$

The slot pitch for this case is equal to

$$\alpha = \frac{\text{motor length}}{\ell}\cdot\frac{2\pi}{85}\ . \tag{42}$$

Two separate sets of thrust calculations were made for the numerical integration method to study the effect of the size of the wave vector increment on the thrust result. The numerical summations were made over a range considered sufficient to encompass the main spectrum of the thrust distribution function. The numbers in

TABLE 9. COMPARATIVE TLRV LIM THRUSTS COMPUTED BY THEOREM OF RESIDUES AND NUMERICAL INTEGRATION METHODS

Freq. Hz	Residue Method[a] (Yamamura) N.	Numerical Integration[b] (Iwamoto) N. *	N. **
155	343	784(129)	347 (1)
160	1020	714(-30)	1011 (-1)
165	1600	1484(-7)	1597 (0)
170	2060	2241(9)	2063 (0)
175	2270	2255(-5)	2379 (0)
180	2510	2464(-2)	2536 (1)
185	2490	2554(2)	2541 (2)
190	2360	2362(0)	2418 (2)
195	2130	2146(1)	2202 (3)
200	1860	1885(1)	1935 (4)

(a) computed with J_1 defined by Equation (35)

(b) computed with $J_1(\nu)$ defined by Equation (36)

* periodic length ℓ = 33.212m.

** periodic length ℓ = 132.848m.

LIM speed = 300 MPH

parentheses specify the percent deviation in the thrust computed by the two methods. A glance at the table shows that the agreement is excellent between the residue method and the numerical summation method for the choice of a unit cell length equal to 132.848m. and reasonably good for the choice of a unit cell length equal to 33.212m. The results substantiate the equivalence of the two methods but point up the importance of the proper choice of wave number increment when numerically summing the thrust.

The expression for current density given by Equation (41) neglects the high-order harmonics associated with the number of slots per phase belt and number of phase belts per pole. A more complete description of the harmonic current density spectrum is given by the expression,

$$J(\nu) = \frac{16NI\sqrt{2}}{\pi \ell} \frac{\sin P\left(\frac{\nu mq\alpha - \pi}{2}\right)}{2 \sin\left(\frac{\nu qm\alpha - \pi}{2}\right)} \cdot \frac{\sin \nu q\alpha/2}{\sin \nu\alpha/2} \cdot \frac{\sin m\left(\frac{\nu q\alpha - \pi/m}{2}\right)}{\sin\left(\frac{\nu q\alpha - \pi/m}{2}\right)}$$

$$\cdot \sin \frac{\nu\alpha}{2} \left(\frac{mq - \varepsilon}{2}\right) \alpha \qquad (43)$$

where m is the number phases, and ε is the number of half-filled slots in the winding end turns. Table 10 presents the thrusts computed using Equations (41) and (43) for the example of the TLRV LIM. The value of periodic length was ℓ = 132.848 m. for both sets of calculations. The data shows that the use of the more complete current density expression given by Equation (43) results in significantly lower thrust values at low slip frequencies.

Several conclusions can be drawn from the thrust calculations presented in this section. The residue method and the numerical integration method yield equivalent results if the integration interval is made sufficiently narrow and the current densities used for both methods are consistent. Errors which result from the use of integration intervals, which are too large tend to be more pronounced at low slip frequencies. When higher-order harmonics are included in the current density distribution function,

TABLE 10. COMPARATIVE TLRV LIM THRUSTS COMPUTED USING $J_1(\nu)$ DEFINED BY EQUATIONS (41) AND (42). LIM SPEED = 300 MPH[1]

Freq. Hz	F_x (J_1: Eqn 20) N.	F_x (J_1: Eqn 22) N.
155	347	-49.3
160	1011	696
165	1597	1384
170	2063	1957
175	2379	2368
180	2536	2597
185	2541	2644
190	2418	2535
195	2202	2313
200	1935	2027

the thrust is reduced at low slip frequencies. An advantage in utilizing the numerical integration technique is the comparative ease with which arbitrary winding current configurations can be included in the summation process.

2.2.2 The Yamamura Model With Edge-Effect Correction

The previous discussion of the Yamamura LIM model considered the restrictive case when edge-effects (due to finite current sheet width) are assumed absent and the primary and secondary are infinitely wide. The computed thrusts describe the effect of a finite primary length on the total developed thrust of the LIM without regard to the effect of a finite primary width. When the finite width of the LIM is included in the analysis, the value of computed thrust is considerably altered. A study of linear induction motors with finite width primary and secondary structures by Bolton outlines one method for incorporating into the mathematical treatment the necessary corrections for edge-effects. The Bolton method consists of deriving a set of equivalent LIM parameters, which are used to describe the effective secondary resistivity and magnetizing reactance of the LIM when edge currents are present. The parameters are derived by Bolton under the assumption that end-effects are absent and that the flux density immediately beyond the stator edges is zero. While the above assumptions are only approximately realized in practice, numerical studies based on the Bolton analysis have yielded satisfactory results in terms of actual-versus-computed flux density in the LIM air gap. The use of the Bolton method, therefore, represents a reasonable first-approximation approach to the edge-effect LIM correction.

2.2.2.1 The Bolton Correction for Finite LIM Width

The finite width of the primary is taken into account in the Yamamura analysis by utilizing the Bolton Theory[5] of linear induction motors for symmetrically positioned secondaries. The Yamamura model corrects for edge-effects by introducing an effective goodness factor and secondary current into the calculations. The latter factors were derived to maintain the same average airgap

flux density with edge currents as that determined in the absence of edge current and using the unmodified goodness factor and secondary current. In the presence of edge-effect, the effective goodness factor becomes,

$$G' = (K_R/K_X)\ G \tag{44}$$

where $G = \omega\mu_o\sigma b/aK^2$

The effective current density, J_1', likewise becomes,

$$J_1' = K_1\ J_1 \tag{45}$$

where

$$K_R = 1 - \mathrm{Re}\left\{(1-jsG)\ \frac{\lambda}{\alpha a}\ \tanh\alpha a\right\} \tag{46}$$

$$K_X = 1 + \mathrm{Re}\left\{(Gs+j)\ Gs\ \frac{\lambda}{\alpha a}\ \tanh\alpha a\right\} \tag{47}$$

$$K_1 = K_X\ \frac{1 + s^2G^2K_R^2/K_X^2}{1 + s^2G^2} \tag{48}$$

Yamamura ascribes to the secondary conductivity the same edge-effect dependence as that assigned to the goodness factor via Equation (44). This is only valid if the magnetizing reactance is held fixed and leads to some confusion when comparing equivalent parameters with those of Bolton.

LIM thrust including edge-effects is found by summing Equations 35-37, using the effective goodness factor G' in place of G, and the effective current density J_1' instead of J_1. Care must be exercised in substituting J_1' for J_1 since this substitution is made to "correct" the flux density at the primary resulting from the edge-effect perturbation. The primary current density remains constant in the Yamamura model as given by Equation 1. The correction for edge-effects requires that J_1^2 in Equations 19-21 be replaced with $J_1 \cdot J_1'$ and not $J_1'^2$.

The parameters K_1 and K_R/K_X were computed for the examples of the TLRV and LIMRV LIM's operating at the respective speeds of 300 and 250 mph. Tables 11 and 12 list the values of these parameters as a function of driving frequency. The effective secondary conductivities of both LIM's are reduced by a factor of at least two; the effective current densities also exhibit a pronounced decrease with increasing slip frequency.

2.2.2.2 Solution of $H(\xi)=0$ via the Newton-Raphson Method; Edge-Effect Included

The solution of Equation (30) when the edge-effect is included in the treatment will be presented for completeness. The procedure described in Section 2.1.2 for determining the roots via the Newton-Raphson method was applied to the present calculations. Some difficulty was experienced in applying this method to the example of the TLRV LIM at higher slip frequencies, a situation not occurring in the previous calculation presented in Tables 7 and 8. When an attempt was made to determine ξ_3 using as an initial approximation of root of Equation (30) for small secondary thickness and airgap distance, the root determined by the Newton-Raphson method converged to ξ_2. The computer program was subsequently modified so as to set the initial approximation of ξ_3 equal to the value of the previous computed root determined at a somewhat different driving frequency. No difficulty was subsequently experienced in evaluating the roots of $H(\xi)$ after this modification.

The computed roots are presented in Tables 13 and 14 for the examples of the TLRV and LIMRV LIMs using the Bolton parameters given in Tables 11 and 12. For both motors, the imaginary part of ξ_3 is large, indicating that the corresponding "exit" end-effect waves are highly damped. The relative effect of the finite LIM width on ξ_2 can be seen by comparing the corresponding roots given in Tables 5 and 13 for the TLRV LIM and those given Tables 6 and 14 for the LIMRV LIM. The tables show that the main effect of finite stator width is to increase the imaginary part of ξ_2 resulting in increased damping of the entrance end-effect wave. This is expected on a physical basis since edge-effects produce a constriction of

TABLE 11. BOLTON PARAMETERS COMPUTED FOR TLRV LIM. MOTOR SPEED = 300 MPH

Freq. Hz	$\frac{K_R}{K_X}$	K_1
150	.40	1.0
155	.40	.99
160	.38	.95
165	.37	.91
170	.35	.87
175	.33	.83
180	.31	.79
185	.30	.76
190	.29	.73
195	.28	.71
200	.27	.69

TABLE 12. BOLTON PARAMETERS COMPUTED FOR LIMRV LIM. MOTOR SPEED = 250 MPH

Freq. Hz	$\frac{K_R}{K_X}$	K_1
160	.57	.99
165	.55	.96
170	.52	.91
175	.49	.87
180	.46	.83
185	.44	.80
190	.42	.77
195	.41	.75
200	.39	.79

TABLE 13. ROOTS OF $H(\xi)=0$ FOR TLRV LIM; EDGE-EFFECTS INCLUDED. LIM SPEED = 300 MPH

Freq. Hz	ξ_1	ξ_2	ξ_3
150	-7.012	-7.02+j0.18	0.40-j252.63
155	"	-7.25+j0.20	0.42-j252.40
160	"	-7.48+j0.22	0.44-j251.86
165	"	-7.71+j0.25	0.48-j251.11
170	"	-7.94+j0.27	0.52-j250.27
175	"	-8.17+j0.31	0.56-j249.40
180	"	-8.40+j0.34	0.60-j248.55
185	"	-8.63+j0.37	0.65-j247.74
190	"	-8.86+j0.41	0.69-j246.98
195	"	-9.09+j0.45	0.74-j246.29
200	"	-9.32+j0.48	0.78-j245.64

TABLE 14. ROOTS OF $H(\xi)=0$ FOR TLRV LIM; EDGE-EFFECTS INCLUDED. LIM SPEED = 250 MPH

Freq. Hz	ξ_1	ξ_2	ξ_3
150	-8.840	-8.41+j0.29	0.36-j182.64
155	"	-8.69+j0.30	0.37-j182.84
160	"	-8.97+j0.32	0.38-j182.83
165	"	-9.25+j0.35	0.40-j182.65
170	"	-9.53+j0.39	0.43-j182.35
175	"	-9.80+j0.43	0.46-j182.00
180	"	-10.08+j0.47	0.49-j184.64
185	"	-10.35+j0.52	0.52-j181.29
190	"	-10.63+j0.56	0.55-j180.96
195	"	-10.90+j0.61	0.58-j180.65
200	"	-11.17+j0.66	0.61-j180.37

secondary current flow near the stator edges and an increase in the secondary resistance; this results in more rapid attenuation in the end-effect wave distance.

2.2.2.3 Yamamura LIM Thrust With Edge-Effect Included

The thrust was next computed for the LIM models based on the TLRV and LIMRV LIM's and including the corrections for the finite width of the primary. Tables 15 and 16 give the magnitudes of the thrust components, F_1(normal wave), F_2(entrance end-effect wave), F_3(Exit end-effect wave) for the TLRV and LIMRV LIM's driven at different line frequencies. The F_3 thrust component is negligibly small compared with F_1 and F_2 and can be discarded with little error in the final thrust result. This leads to an appreciable reduction in computer time, since it eliminates the length calculation of one of the two roots of $H(\xi) = 0$.

A comparison of thrusts computed by the Yamamura, Oberretl, and mesh-matrix models is given in Figures 15 and 16 for the TLRV & LIMRV LIM's. The Yamamura model gives consistently larger thrusts than the mesh-matrix model. In general, the Yamamura model gave thrusts which agreed better with the Oberretl thrust than with the mesh-matrix thrusts. Below the frequency of 170 HZ, the Yamamura and Oberretl models predicted identical thrusts for the TLRV LIM.

The thrust characteristics shown in Figures 14 and 15 are sensitive to the end-effect and the manner in which it is treated in the Yamamura, Oberretl, and mesh-matrix theories. Since the Yamamura model uses the Bolton factor to compensate for edge-effect, some error is expected since the Bolton factor neglects end-effect in its derivation.

It is worthwile to review certain aspects of the different LIM models in the light of the results previously presented. The Yamamura model considers the fundamental mmf harmonic only and neglects higher-order mmf components. The inclusion of higher-order mmf harmonics in the Yamamura calculation would likely result in some reduction in computed thrust due to the negatively

TABLE 15. PREDICTED THRUST FOR TLRV LIM USING YAMAMURA THEORY WITH EDGE-EFFECTS INCLUDED. MOTOR SPEED = 300 MPH

Freq. Hz	F_1 N.	F_2 N.	F_3 N.	F_x N.
150	3910	-4460	2.90	-548
155	24300	-23300	2.87	987
160	16900	-14500	2.78	2420
165	12300	-8670	2.67	3620
170	9570	-5050	2.56	4520
175	7830	-2750	2.46	5080
180	6620	-1310	2.36	5310
185	5740	- 476	2.28	5270
190	5070	- 58.8	2.21	5010
195	4540	86.4	2.15	4630
200	4110	73.9	2.10	4190

I = 530A./Ph.
b = .0066 M.
gap = .017M

TABLE 16. PREDICTED THRUST FOR LIMRV LIM USING YAMAMURA THEORY WITH EDGE-EFFECTS INCLUDED. MOTOR SPEED = 250 MPH

Freq. Hz	F_1 N.	F_2 N.	F_3 N.	F_x N.
160	12700	-10800	2.68	1910
165	14800	-10000	2.63	4770
170	11500	-5010	2.56	6470
175	9000	-2070	2.47	6940
180	7340	- 804	2.39	6540
185	6180	- 431	2.32	5750
190	5340	- 378	2.26	4960
195	4690	- 356	2.20	4340
200	4190	- 286	2.15	3906

I = 1200A/Ph.
b = .0071M
gap = .024M

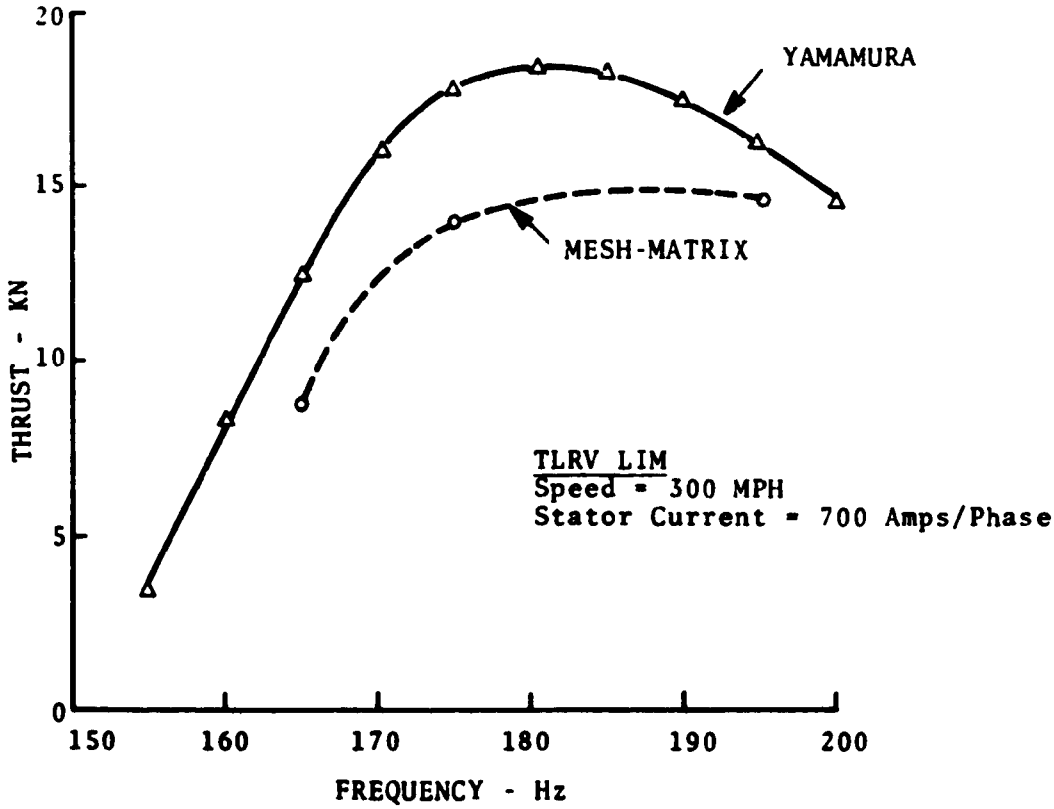

FIGURE 14. TLRV LIM THRUST AS PREDICTED BY YAMAMURA THEORY

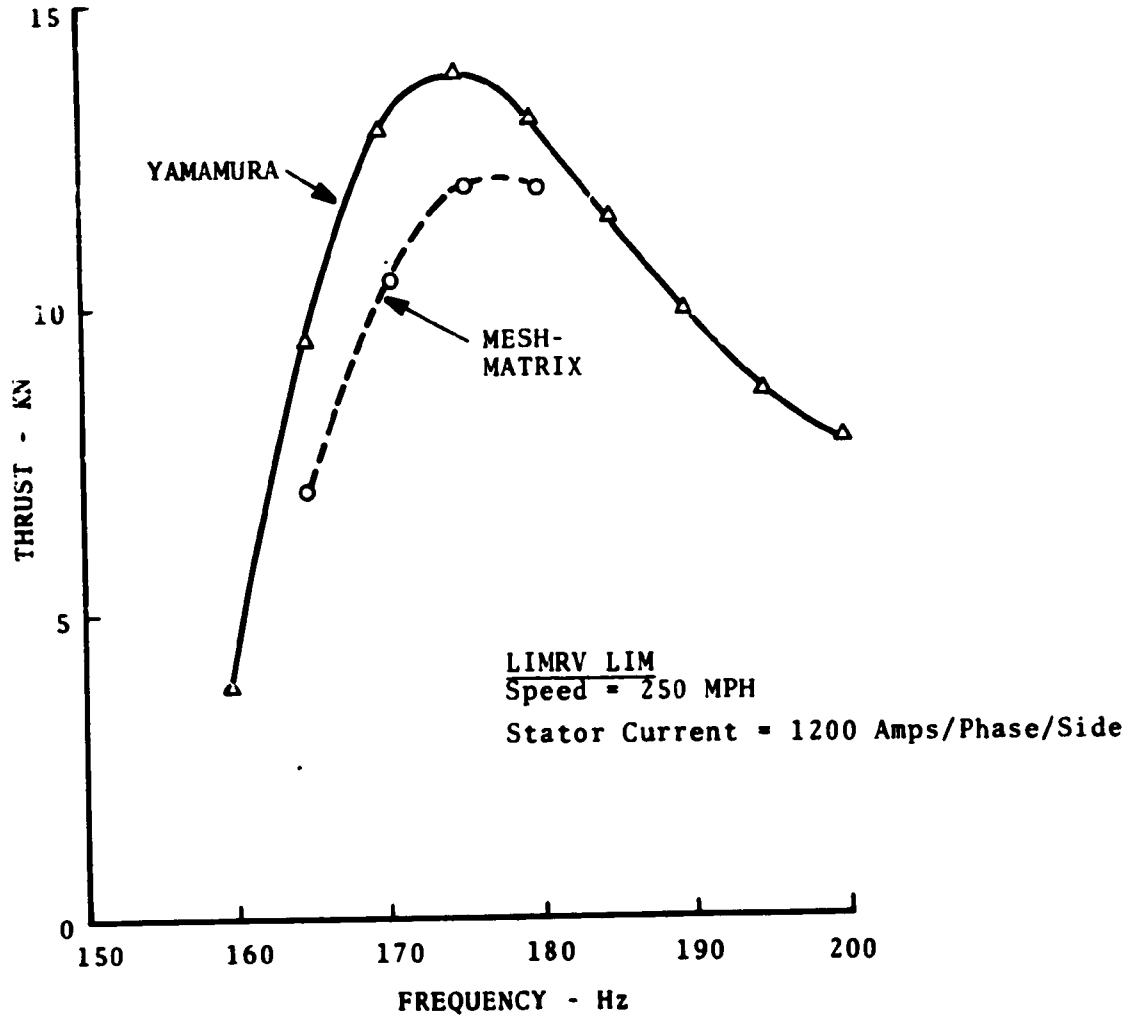

FIGURE 15. LIMRV LIM THRUST AS PREDICTED BY YAMAMURA THEORY

propagating 5-th harmonic wave; it is unlikely, however, that the thrust reduction would be sufficient to bring the Yamamura thrust into agreement with the Elliott result. Both Yamamura and Elliott models compensate for edge-effects by modifying the values of the secondary resistivity and magnetizing reactance according to the method of Bolton. In deriving the appropriate factors to modify the secondary resistivity and magnetizing reactance, Bolton neglects end-effects. A glance at Tables 15 and 16 shows that end-effects have a dominant effect at low slip frequencies and could not be neglected when computing thrust. The possible error introduced into the result by neglecting end-effects in calculating Bolton factors and ultimately thrust remains unknown.

The Yamamura model described in this report uses the same value of secondary resistivity for both normal and end-effect secondary current waves. It is questionable whether the same current flow constriction exists for the end-effect current wave and whether its effective resistivity should be the same as that of the normal wave. The Oberretl treatment avoids the above complication by describing the current distribution as a multiple-harmonic Fourier representation and the secondary resistivity as the actual secondary resistivity.

2.2.3 Summary of Yamamura Theory Applied to TLRV & LIMRV LIMs

The Yamamura theory of linear induction motors was used to compute the thrust developed by the TLRV and LIMRV LIMs. The computer study shows that the Yamamura theory predicts LIM thrusts in reasonable agreement with the Oberretl and Elliott predictions. The Yamamura LIM thrusts tend to agree more closely with the Oberretl predictions than with those of Elliott.

The possible reasons for the predicted thrust discrepancies have been considered. The Yamamura model describes the primary mmf by a single spatial harmonic and neglects the effect of the higher-order mmf components. A computer study of the effect of these additional harmonics indicates that; for the example of the TLRV LIM, the additional mmf harmonics reduce LIM thrust considerably in the region of zero slip frequency and have a small effect on LIM thrust at higher slip frequencies. In the Yamamura model, edge-effects (current) are compensated by modifying the values of secondary resistivity and magnetizing reactance according to the theory by Bolton. The ultimate effect on LIM thrust of neglecting end-effects in the derivation of the Bolton factor is questionable, as is the effect of using a common value of effective secondary resistivity for both normal and end-effect secondary current waves.

The Yamamura LIM model assumes a continuous primary ferromagnetic region and neglects the magnetic end-effects associated with the ferromagnetic boundaries. Yamamura states that the above assumption results in negligible error in the LIM output characteristics, since the important boundary conditions at the entrance end of the motor are little affected by the highly damped exit end-effect wave. If the above condition is correct, then other explanations must be found to account for the discrepancies between the Yamamura results and those of the mesh-matrix which takes into account the finite length of the stator core.

The computer time required to run the Yamamura computer program is comparable with that required to run the Oberretl computer program, namely about 40-60 seconds for 10 case runs. This is approximately an order of magnitude less than the time required to run the same number of cases using the mesh-matrix computer program.

2.3 THE MOSEBACH THEORY OF THE LINEAR INDUCTION MOTOR

2.3.1 The Mosebach LIM Model[3]

Because exact solutions of the field equations for actual LIMs are impossible, one must resort either to approximate solutions of real structures, or to exact solutions of idealized models of real structures. The Mosebach treatment takes the latter approach. It replaces the real motor, shown in Figure 16a, with an idealized model as illustrated in Figure 16b. The stator winding current is represented in the model by a surface current density sheet propagating in the x-direction. The secondary is described by a region with conductivity and dimensions equivalent to that of the real secondary.

The coordinates used in the model description are shown in Figure 16b. The origin is positioned at the center of the motor and inside the secondary. The secondary moves in the x-direction relative to the fixed primary. The y-axis denotes the direction normal to the motor surface and the z-axis denotes the direction along the transverse axis of the motor.

The LIM model simulates the fringing magnitude flux of the real motor by means of the linear gap function of 51 degrees shown in Figure 16b. In the idealized model, airgap flux is assumed to be restricted to the y-direction in the absence of secondary. Conformal mapping studies of the flux distribution of the real motor (comprising 90 degree air-iron interfaces at motor ends) without secondary reveal that the y-directed flux of the real motor is closely approximated by that of the idealized model at positions along the x-axis of the motor.[4]

Two versions of the above model are considered by Mosebach and referred to as the <u>one-dimensional LIM model</u> and the <u>two-dimensional LIM model</u>. The one-dimensional model treats the fringing fields at the motor ends only, by the use of the linear gap function. The ferromagnetic primary is assumed to be continuous in the transverse direction. The two-dimensional model uses the linear gap function to describe the varying magnetic

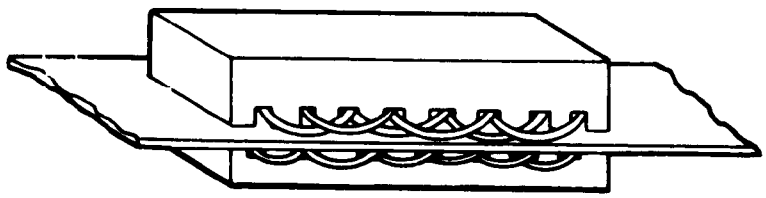

FIGURE 16a. SKETCH OF REAL LIM

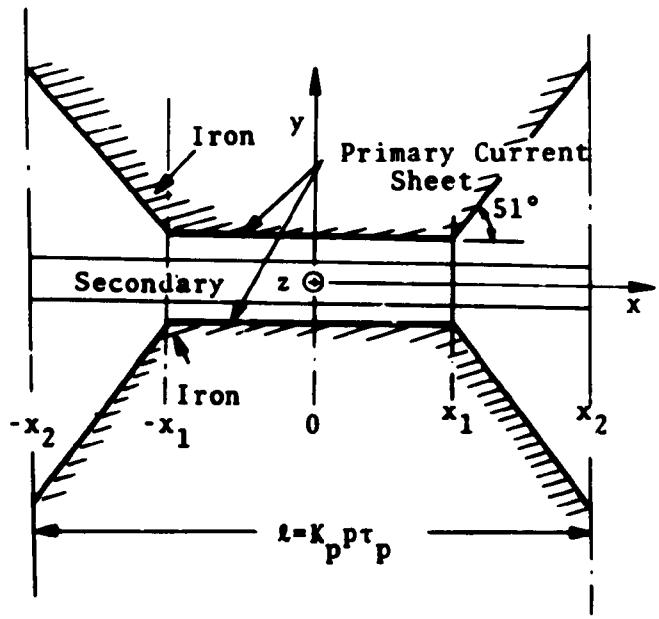

FIGURE 16b. EQUIVALENT MOSEBACH LIM MODEL (SIDE VIEW)

permeance at both the ends and the sides of the motor. Thus, it should provide a better description of magnetic boundary effects than the one-dimensional model. However, this is partly offset by the increased computer time required in the two-dimensional computer analysis. The one-dimensional computer program is used exclusively in this report for computer studies based on the Mosebach LIM model.

End views of the one and two-dimensional models are shown in Figures 17a and 17b. The primary and secondary edges are located at transverse positions z_1 and z_2 respectively. The secondary half-thickness is y_1 and the core-to-core separation is $2y_{20}$.

The following assumptions are applicable to both versions of the Mosebach model:

a. The permeability of the ferromagnetic primary is infinite. The permeability of the secondary is equal to free-space permeability.

b. Primary and secondary currents are confined to the x-z plane.

c. Air-gap and secondary thickness are small compared with the pole pitch. Y-directed flux components are assumed uniform in both the airgap and the secondary.

d. Primary current density (surface) varies with distance (x) and time (t) according to exp (jkx + ωt).

The following additional assumptions are applicable to the one-dimensional model:

e. Secondary currents inside the primary region ($-z_1<z<z_1$) flow in the z direction.

f. Secondary currents outside the primary region flow in the x-direction. Current density in the secondary overhang (sidebar) is a uniform function of z.

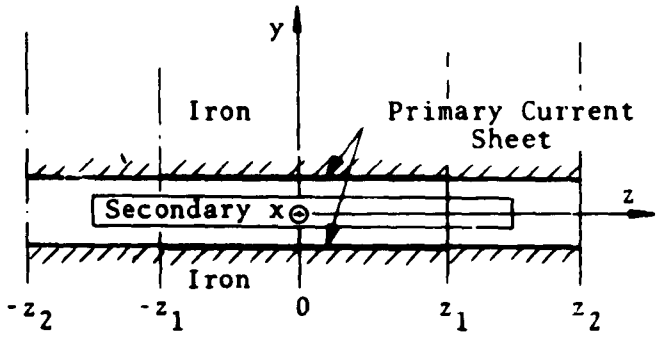

FIGURE 17a. END VIEW OF ONE-DIMENSIONAL MOSEBACH MODEL

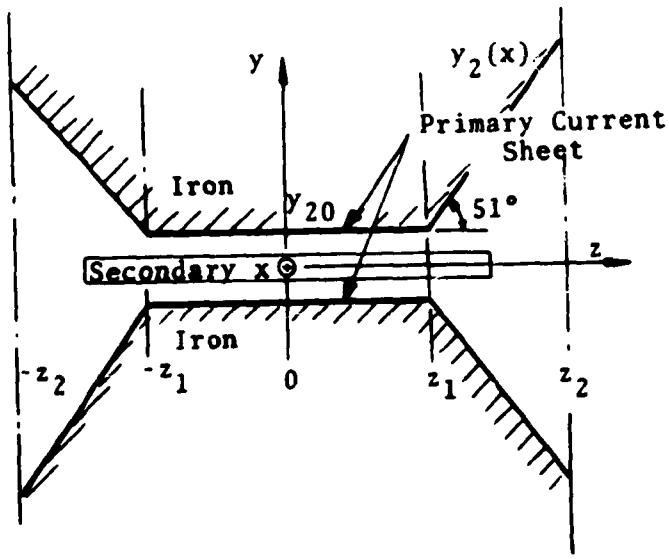

FIGURE 17b. END VIEW OF TWO-DIMENSIONAL MOSEBACH MODEL

2.3.1.1 Magnetic Induction Equation: Two-Dimensional Model

The solution for the electromagnetic fields in the region between the two sides of the primary follows from Ampere's law with displacement current neglected and Faraday's law. Thus,

$$\bar{\nabla} \times \bar{H} = \bar{J}$$

$$\bar{\nabla} \times \bar{E} = - \frac{\partial \bar{B}}{\partial t} \tag{49}$$

where $\bar{G}$ is the secondary current density. For an isotropic medium moving with velocity $\bar{V}$, Ohm's law gives,

$$\bar{J} = \sigma \, (\bar{E} + \bar{V} \times \bar{B}) \, . \tag{50}$$

Continuity of current inside the secondary requires,

$$\bar{\nabla} \cdot \bar{J} = 0 \tag{51}$$

Since assumption c requires the normal field to be independent of y, it is convenient to apply Ampere's law in integral form around the contour shown in Figure 18. Thus,

$$H(x+\Delta x) \cdot y_2(x+\Delta x) - H(x) \cdot y_2(x) = K_z \, \Delta x + J_z \cdot \Delta x \, y_1$$

or

$$\frac{\partial}{\partial x} \left(B_y y_2 \right) = \mu_o \left(K_z + J_z y_1 \right) \tag{52}$$

where K_z^+ and J_z are the primary surface current density and secondary (volume) current density, respectively, in the z-direction.

---

†In the Mosebach notation, primary surface current density is given by A_z instead of K_z.

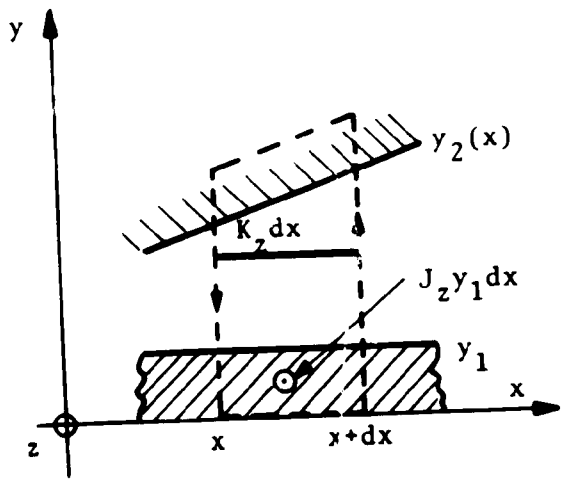

FIGURE 18. CONTOUR INTEGRATION USED IN DERIVATION OF MAGNETIC INDUCTION EQUATION

For the y field component, Faraday's law gives,

$$\frac{\alpha E_x}{\alpha z} - \frac{\alpha E_z}{\alpha x} = - \frac{\alpha B_y}{\alpha t} \tag{53}$$

where the electric field components E_x, E_z, given by Equation (50) take the form,

$$E_x = \frac{1}{\sigma} J_x$$

$$E_z = \frac{1}{\sigma} J_z - v B_y .$$

Here v is the speed of the secondary in the x direction relative to the motor. Substituting E_x, E_z in Equation (53) gives,

$$\alpha J_z/\alpha x - \alpha J_x/\alpha z - \sigma\left[\alpha B_y/\alpha t + \alpha/\alpha x \left(v B_y\right)\right] = 0 \tag{54}$$

J_x can be eliminated using Equation (51) after taking the partial derivative of Equation (54) with respect to x.

J_x can be eliminated using Equation (51) after taking the partial derivative of Equation (54) with respect to x.

$$\frac{\alpha^2 J_z}{\alpha x \alpha z} + \frac{\alpha^2 J_z}{\alpha z^2} = \frac{\sigma \alpha}{\alpha x}\left(\frac{\alpha B_y}{\alpha t} + \frac{\alpha}{\alpha x}\left(v\ B_y\right)\right) = 0 \qquad (55)$$

If J_z is calculated from Equation (52), Equation (55) can be rewritten in the form expressing the field B_y, air-gap $y_2(x)$, and primary current density K_z in terms of the independent variables, x, z, and t.

$$\frac{\alpha^3}{\alpha x^3}\left(B_y y_2\right) + \frac{\alpha^3}{\alpha x \alpha z^2}\left(B_y y_2\right) - \mu_o \sigma y_1 \frac{\alpha}{\alpha x}\left[\frac{\alpha B_y}{\alpha t} + \frac{\alpha B_y}{\alpha x}\right] = \mu_o\left[\frac{\alpha^2 K_z}{\alpha x^2} + \frac{\alpha^2 K_z}{\alpha z^2}\right] \qquad (56)$$

A derivation of the corresponding equation for the one-dimensional model is given below.

2.3.1.2 Magnetic Induction Equation: One-Dimensional Model

The one-dimensional model assumes secondary currents flow in rectangular shaped paths as illustrated in Figure 19a. Inside the primary region, secondary currents flow in the z-direction; outside the primary region, secondary currents flow in the x-direction. No flux generated by the edge currents couples to the primary currents. The field inside the primary is constant in amplitude and phase over the width of the primary.

Faraday's Law of Induction, Equation (49) written in integral form, together with Ohm's law for the moving secondary, requires that for a contour C in the secondary enclosing a surface S,

$$\frac{1}{\sigma}\int_C \bar{J}\cdot d\bar{\ell} + \frac{\alpha}{\alpha t}\int_S \bar{B}\cdot\bar{n}\ da - \int_C \bar{V}\times\bar{B}\cdot d\bar{\ell} = 0\ . \qquad (57)$$

This general law is now applied to a current path having incremental length Δx in the x direction, but finite width spanning half of the secondary (Figure 19b).

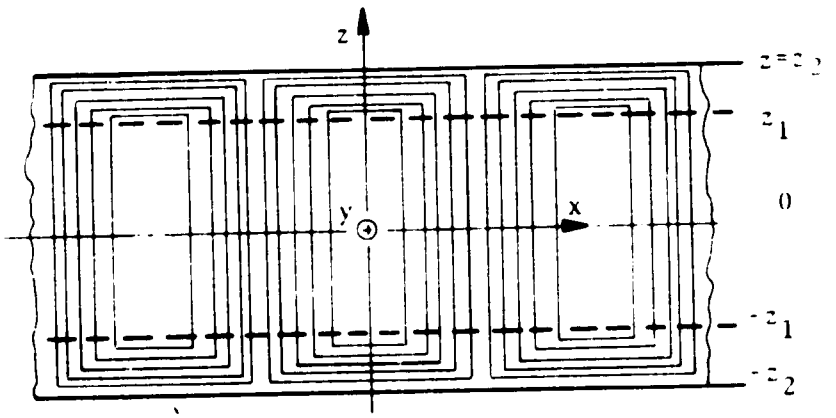

FIGURE 19a. SECONDARY CURRENT FLOW PATTERN FOR ONE-DIMENSIONAL MODEL

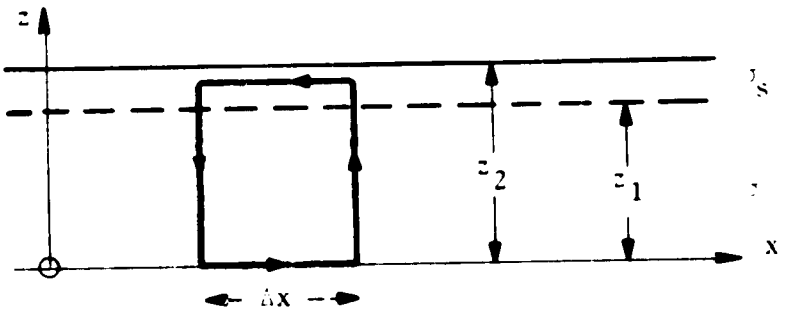

FIGURE 19b. INCREMENTAL CURRENT PATH FOR ONE-DIMENSIONAL MODEL

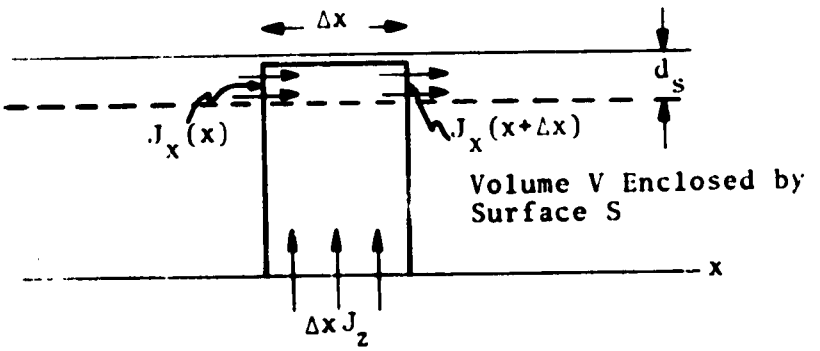

FIGURE 19c. INCREMENTAL MODEL FOR CURRENT CONTINUITY

$$\frac{1}{\sigma}\int_0^{z_1} J_z(x+\Delta x)dz - \frac{1}{\sigma}\int_0^{z_1} J_z(x)dz - \frac{J_x}{\sigma_s}\Delta x$$

$$- v\int_0^{z_1}\left[B_y(x+\Delta x) - B_y(x)\right]dz - \frac{\alpha}{\alpha t}\int_0^{z_1} B_y\,\Delta x\,dz = 0 \quad (58)$$

Here, the conductivity of the edges of the secondary is designated as σ_s as distinguished from σ describing the central region of the secondary.

Consistent with the one-dimensional model is the assumption that J_z and B_y in the region $-z_1<z<z_1$ are independent of z so that in the limit $\Delta x\to 0$, Faraday's law requires that

$$\frac{z_1}{\sigma}\frac{\alpha J_z}{\alpha x} - \frac{J_x}{\sigma_s} - z_1\left(\frac{B_y}{\alpha t} + \frac{\alpha B_y}{\alpha x}\right) = 0 . \quad (59)$$

Just as an integral form of Faraday's law is used to bring the edge effects into the one-dimensional model, so also is an integral form of the current continuity equation, Equation (51), now brought in. With the help of the incremental section of secondary shown in Figure 19c, the continuity condition requires that

$$d_s\left[J_x(x+\Delta x) - J_x(x)\right] = J_z\,\Delta x \quad (60)$$

and in the limit it follows that

$$J_z = d_s\frac{\alpha J_x}{\alpha x} \quad (61)$$

where the thickness of the edge is defined as $d_s = z_2 - z_1$.

After taking the derivative with respect to x of Equation (59), use can be made of Equation (61) to eliminate J_x, and it follows that

$$z_1 \frac{\partial^2 J_z}{\partial x^2} - \frac{1}{\sigma_s} J_z - z_1 \left[\frac{\partial B_y}{\partial t} + v \frac{\partial B_y}{\partial x} \right] = 0. \qquad (63)$$

With the understanding that B_y and K_z are independent of z, Equation (52) can be introduced into this expression to eliminate J_z and give Mosebach's expression for the magnetic flux density as a function of the primary currents.

$$\frac{\partial^3}{\partial x^3}\left(B_y y_2\right) - \frac{\sigma}{z_1 \sigma_s d_s} \frac{\partial}{\partial x}\left(B_y y_2\right) - \sigma y_1 \mu_o \frac{\partial}{\partial x}\left[\frac{\partial B_y}{\partial t} + v \frac{\partial B_y}{\partial x}\right] \qquad (65)$$

$$= \mu_o \frac{\partial^2 K_z}{\partial x^2} - \frac{\sigma \mu_o}{z_1 \sigma_s d_s} K_z$$

The above equation determines the field distribution in the one-dimensional Mosebach model.

2.3.1.3 Solution of Magnetic Induction Equation: Two-Dimensional Model

The Mosebach treatment of the two-dimensional LIM model consists of expanding the spatial distributions of the airgap flux density $B_y(x,z)$, primary current density $K_z(x,z)$, and airgap function $y_2(x,z)$ along both the longitudinal (x) and transverse (z) axes of the LIM model. For this purpose, it is convenient to define a 'motor unit cell' having a length ℓ in the x direction and width $2z_2$ in the z direction. Inside the cell region, $B_y(x,z)$, $K_z(x,z)$, $y_2(x,z)$ are each described by a two-dimensional Fourier series, each term in the series being characterized by a wave propagation vector, $\bar{k}$, given by

$$\bar{k} = \bar{i}_x \frac{n\,2\pi}{\ell} + \bar{i}_z \frac{m\pi}{2z_2} \qquad (64)$$

$$\bar{k} = \bar{i}_x\, n\, a + \bar{i}_z\, m\, b \qquad (65)$$

where n, m are the harmonic orders associated with the x,z wave vector components. In practice, the unit cell length ℓ is set approximately equal to a multiple of the primary winding length. If KP denotes some integer greater than unity, then $\ell = KP \cdot P\tau_p$, where P is the number of (mmf) poles in the motor. The width of the unit cell, $2z_2$, can be chosen equal to the [illegible]ndary width. The two-dimensional function distributions [illegible] he form,

$$B_y(x,z,t) = \mathrm{Re} \sum_n \sum_m B_{nm} e^{j(\omega t + nax + [illegible])} \tag{66}$$

$$K_z(x,z,t) = \mathrm{Re} \sum_n \sum_m K_{nm} e^{j(\omega t + nax + mbz)} \tag{67}$$

$$y_2(x,z,t) = \sum_\lambda \sum_\mu Y_{\lambda\mu} e^{j(\lambda ax + \mu bz)} \tag{68}$$

The harmonic amplitudes K_{nm} and $Y_{\lambda\mu}$ are found by taking the Fourier transforms of the known spatial distributions of primary current and airgap spacing respectively.

The substitution of Equations (66), (67), (68) in (56) yields the following equation relating the amplitude cofficients B_{nm}, K_{nm}, and $Y_{\lambda\mu}$.

$$\sum_m \sum_n \sum_\mu \sum_\lambda \left[-j(n+\lambda)^3 a^3 - j(n+\lambda)a(m+\mu)^2 b^2 \right] Y_{\mu\lambda} B_{nm} e^{j\left(\omega t + (n+\lambda)ax + (m+\mu)bz\right)}$$

$$- \sigma y_1 \mu_o \sum_n \sum_m (jna)(j\omega + jvna) B_{nm} e^{j(\omega t + nax + mbz)} \tag{69}$$

$$= \mu_o \sum_n \sum_m \left[(jna)^2 + (jmb)^2 \right] K_{nm} e^{j(\omega t + nax + mbz)}$$

†Mosebach uses P_o to denote number of pole pairs.

Transforming the summation indices n, m, in Equation (69).

$$m + \mu \rightarrow m$$

$$n + \lambda \rightarrow n$$

and collecting coefficient of terms with identical space and time dependences,

$$\sum_{\mu}\sum_{\lambda} Y_{\mu\lambda} B_{m-\mu,n-\lambda} + j\, r\, \frac{s_n\, y_{20}}{\left(\frac{2n}{K_p p}\right)^2 + \left(\frac{m\tau_p}{2z_2}\right)^2} B_{nm} = -\, j\mu_o \frac{K_{nm}}{\left(\frac{2n}{K_p p}\right)\frac{\pi}{\tau_p}} \tag{70}$$

where r is the magnetic Reynolds number

$$r = \frac{\mu_o \omega \sigma y_1}{\left(\frac{\pi}{\tau_p}\right)^2 y_{20}} \tag{71}$$

and s_n is the harmonic slip given by

$$s_n = 1 - \left(\frac{2n}{K_p p}\right)(1 - s). \tag{72}$$

The quantity y_{20} in Equation (70) denotes the half-spacing between primary cores (see Figure 17b). Equation (70) describes a set of linear, complex equations relating the unknown flux density amplitudes, B_{nm}. In matrix notation, the equation takes the form,

$$\left([Y] + j\,[R]\right)\cdot \bar{B} = \bar{K} \tag{73}$$

[Y] is a real, quadratic matrix and is independent of slip. [R] is a real, diagonal matrix with slip-dependent elements. The solution of Equation (73) is obtained by setting,

$$\bar{B} = \bar{B}_r + j\,\bar{B}_i$$

$$\bar{K} = \bar{K}_r + j\,\bar{K}_i$$

and solving for the real and imaginery parts of B.

$$\bar{B}_r = \frac{\bar{K}_r - [R]\cdot[Y^{-1}]\cdot\bar{K}_i}{[Y] + [R][Y^{-1}][R]}$$

$$\bar{B}_i = \frac{\bar{K}_i + \bar{B}_r\cdot[R]}{[Y]} \quad .$$

2.3.1.4 Solutions of Magnetic Induction Equation: One-Dimensional Model

The procedure for solving the one-dimensional field equation is identical in principle to that used in the solution of the two-dimensional equation. In the one-dimensional model, the airgap field B_y, primary current density K_z, and airgap spacing function y_2 are expanded in Fourier series along the x axis.

$$B_y(x,t) = \mathrm{Re}\left\{\sum_{n=-\infty}^{\infty} B_n e^{j(\omega t + nax)}\right\} \qquad (74)$$

$$K_z(x,t) = \mathrm{Re}\left\{\sum_{n=-\infty}^{\infty} K_n e^{j(\omega t + nax)}\right\} \qquad (75)$$

$$y_2(x) = \sum_{\lambda=-\infty}^{\infty} Y_\lambda e^{j(\lambda ax)} \qquad (76)$$

Substituting the above equations in Equation (63) gives,

$$\bar{B} = \bar{B}_r + j\,\bar{B}_i$$

$$\bar{K} = \bar{K}_r + j\,\bar{K}_i$$

and solving for the real and imaginery parts of B.

$$\bar{B}_r = \frac{\bar{K}_r - \left[R\right]\cdot\left[Y^{-1}\right]\cdot\bar{K}_i}{[Y] + [R][Y^{-1}][R]}$$

$$\bar{B}_i = \frac{\bar{K}_i + \bar{B}_r\cdot[R]}{[Y]} \quad .$$

2.3.1.4 Solutions of Magnetic Induction Equation: One-Dimensional Model

The procedure for solving the one-dimensional field equation is identical in principle to that used in the solution of the two-dimensional equation. In the one-dimensional model, the airgap field B_y, primary current density K_z, and airgap spacing function y_2 are expanded in Fourier series along the x axis.

$$B_y(x,t) = \mathrm{Re}\left\{\sum_{n=-\infty}^{\infty} B_n e^{j(\omega t + nax)}\right\} \tag{74}$$

$$K_z(x,t) = \mathrm{Re}\left\{\sum_{n=-\infty}^{\infty} K_n e^{j(\omega t + nax)}\right\} \tag{75}$$

$$y_2(x) = \sum_{\lambda=-\infty}^{\infty} Y_\lambda e^{j(\lambda ax)} \tag{76}$$

Substituting the above equations in Equation (63) gives,

$$\sum_n \sum_\lambda - j\left[(n+\lambda)^3 a^3 + \frac{\sigma}{\sigma_s z_1 d_s}(n+\lambda)a\right] Y_\lambda B_n e^{j[\omega t + (n+\lambda)ax]}$$

$$+ \sum_n \mu_o \sigma \omega y_1 na \left(1 + \frac{vna}{\omega}\right) B_n e^{j[\omega t + nax]}$$

$$= - \mu_o \sum_n \left[(na)^2 + \frac{\sigma}{\sigma_s z_1 d_s}\right] K_n e^{j[\omega t + nax]} \qquad (77)$$

Transforming the summation indice n in the first summation, $n+\lambda \rightarrow n$, and collecting coefficients with common space and time dependence,

$$\sum_\lambda Y_\lambda \; B_{n-\lambda} \quad + j \; \frac{r'_n \; s_n \; y_1 \; B_n}{n^2} \quad = - \; j \; \frac{\mu_o}{na} \; K_n \qquad (78)$$

where r'_n is the magnetic Reynolds number associated with the fundamental spatial harmonic in the 'motor unit cell', i.e.,

$$r'_n = \frac{\mu_o \sigma \omega}{a^2 \left(1 + \frac{\sigma}{\sigma_s z_1 d_s a^2 n^2}\right)} \qquad (79)$$

and s_n is as defined by Equation (72). In matrix form, the above equation becomes,

$$[Y] + j[R] \cdot \bar{B} = \bar{K} \qquad (80)$$

For a system comprising the set of harmonics $-2 \leq n \leq 2$, [R] and [Y] take on the form,

$$[R] = \begin{bmatrix} \frac{r'_{-2} s_{-2}}{4} & 0 & 0 & 0 & 0 \\ 0 & \frac{r'_{-1} s_{-1}}{1} & 0 & 0 & 0 \\ 0 & 0 & 0 & 0 & 0 \\ 0 & 0 & 0 & \frac{r'_1 s_1}{1} & 0 \\ 0 & 0 & 0 & 0 & \frac{r'_2 s_2}{4} \end{bmatrix} \qquad [Y] = \begin{bmatrix} Y_0 & Y_1 & Y_{-2} & Y_{-3} & Y_4 \\ Y_1 & Y_0 & Y_{-1} & Y_2 & Y_3 \\ Y_2 & Y_1 & Y_0 & Y_{-1} & Y_{-2} \\ Y_3 & Y_2 & Y_1 & Y_0 & Y_{-1} \\ Y_4 & Y_3 & Y_2 & Y_1 & Y_0 \end{bmatrix}$$

where r' is given by Equation (79) and the matrix elements Y_λ are determined from

$$Y_\lambda = \int_{-\ell/2}^{\ell/2} y_2(x) e^{-j\lambda ax} dx \quad .$$

$\bar{B}$ and $\bar{K}$ are complex vectors

$$\bar{B} = \begin{bmatrix} B_{-2} \\ B_{-1} \\ 0 \\ B_1 \\ B_2 \end{bmatrix} \qquad \bar{K} = \begin{bmatrix} K_{-2} \\ K_{-1} \\ 0 \\ K_1 \\ K_2 \end{bmatrix} .$$

The solution for the real and imaginery parts of B are given by

$$B_r = \frac{\bar{K}_r - [R] \cdot [Y^{-1}] \cdot \bar{K}_i}{[Y] + [R] \cdot [Y^{-1}] \cdot [R]} \tag{81}$$

$$B_i = \frac{\bar{K}_i + \bar{B}_r \cdot [R]}{[Y]} \tag{82}$$

The current density harmonic K_n is found by taking the Fourier transform of the primary current distribution over the length ℓ of the unit cell. In practice, it is desirable to compute the current density harmonics for each phase winding since the "phase harmonics" are required for the subsequent constant voltage analysis. Thus if K_n^k denotes the nth harmonic of the kth phase,

$$\bar{K}_n^k = \frac{1}{\ell} \int_{-\ell/2}^{\ell/2} f_k(x) \; \bar{K}_z^k(x) e^{-jnax} dx \tag{83}$$

where $f_k(x)$ is a 'slot distribution function' which defines the occupancy of a given stator slop, i.e.,

$f_k(x) = 0$ slot unoccupied by kth phase winding

$f_k(x) = 1$ slot occupied by kth phase winding; reference phase equals zero

$f_k(x) = -1$ slot occupied by kth phase winding; reference phase equals 180 degrees.

In closed form, $\bar{K}_n^k$ can be expressed as,

$$\bar{K}_n^k = \left(a_{nk} - jb_{nk}\right) \cdot \bar{K}^k \tag{84}$$

where K^k is the primary current density amplitude

$$\bar{K}^k = \frac{3Nq}{\tau_p} \bar{I}^k \quad . \tag{85}$$

In a similar manner, it is possible to express the nth harmonic of flux density associated with the kth primary phase as,

$$\bar{B}_n^k = - \frac{j\mu_o}{an\ y_{20}} \left(c_n^k - jd_n^k\right) \bar{K}^k \tag{86}$$

where the complex coefficient $c_n^k - jd_n^k$ determines the amplitude and phase of B_n^k.

2.3.1.5 Constant Voltage Source

The solution for the case of a LIM with constant voltage excitation requires the calculation of currents flowing in each phase winding produced by the fixed input voltage excitation. Each phase current is uniquely determined once the input impedance of the given phase winding is known.

The equation for the voltage drop in the kth phase winding of the LIM is,

$$V^k = \left(r_1^k + jX_1^k\right) \cdot I^k + V_{induced}^k \, . \tag{87}$$

The first term on the right-hand side includes the winding resistance and primary leakage reactance. The second term describes the voltage induced by the air-gap field as a result of currents flowing in the different phase windings of the motor. The induced voltage can be computed by integrating the electric field over the length of the conductors in the given phase. For the nth harmonic flux wave,

$$E_n = \frac{\omega B_n}{n a} \tag{88}$$

Expressing B_n in terms of phase currents I_k using Equations (85) and (86),

$$E_n = - j\frac{\omega}{na} \frac{\mu_o}{na\, y_{20}} \frac{3Nq}{\tau_p} \sum_k I^k \left(c_n^k - jd_n^k\right) \tag{89}$$

The phase voltage found by integrating the electric field $E_z(x,t)$,

$$E_z(x,t) = \sum_n E_n e^{j(\omega t + nax)} \tag{90}$$

over all conductors of the k'th phase is,

$$V^{k'} = 2z_1 \int_{-\ell s/2}^{\ell s/2} E_z(x,t) \frac{3Nq}{\tau_p} f^{k'}(x)dx$$

$$= - j\frac{\omega \mu_o 2z_1}{a^2\, y_{20}} \left(\frac{3Nq}{\tau_p}\right)^2 \ell \sum_k I^k \sum_n \left(c_n^k - jd_n^k\right)\cdot\left(a_n^{k'} + jb_n^{k'}\right). \tag{91}$$

The voltages in a three-phase system can be written in the form,

$$\begin{bmatrix} V^1 \\ V^2 \\ V^3 \end{bmatrix} = \left[\begin{array}{c|c|c} Z_{11} + R_1^1 + jX_1^1 & Z_{12} & Z_{13} \\ \hline Z_{21} & Z_{22} + R_1^2 + jX_1^2 & Z_{23} \\ \hline Z_{31} & Z_{32} & Z_{33} + R_1^3 + jX_1^3 \end{array}\right] \begin{bmatrix} I_1^1 \\ I_1^2 \\ I_1^3 \end{bmatrix} \qquad (92)$$

Identifying the impedance elements of the above matrix with Equation (91) gives for the mutual impedance between the k and k'th phases.

$$Z_{kk'} = - j \frac{\omega \mu_o \ell z_{1\ell}}{a^2 y_{20}} \left(\frac{3Nq}{\tau_p}\right)^2 \sum_{n=-\infty}^{\infty} \frac{\left(c_n^k - jd_n^k\right)\cdot\left(a_n^{k'} + jb_n^{k'}\right)}{n^2} \qquad (93)$$

2.3.1.6 LIM Output Parameters

The electromagnetic characteristics of a LIM can be determined once the air-gap flux density and secondary current density have been found for the specified primary current density excitation. The nth harmonic of the second current density J(n) is related to the nth harmonic of air-gap flux density B(n),†

$$J(n) = \frac{\sigma \omega s_n}{a\, n} B(n) \qquad (94)$$

The thrust F_x is found by integrating the force density over the volume of the secondary.

$$F_x = - \int_V 1/2\ \mathrm{Re}\left(J_z\, B_y^*\right) dV \qquad (95)$$

†For clarity, the harmonic order is indicated in the parenthesis rather than subscripts as previously given.

Substituting the Fourier series expansions for J_z, B_y in the above equation and integrating,

$$F_x = \sum_n F_x(n) = 2z_1 y_1 K_p P\tau \sum_n \left(B(n)G^*(n) + B^*(n)J(n) \right) \qquad (96)$$

Mechanical power P_m, is equal to the product of thrust and motor speed. It can also be expressed as the summation of the products of thrust harmonics and speed harmonics. Since the nth harmonic wave has a speed $v(n)=(1-s_n)\omega/na$, the mechanical power is

$$P_m = \sum_n P_m(n) = \sum_n F_x(n) \ (1-s_n) \ \frac{\omega}{a\,n} \qquad (97)$$

The air-gap power which is the real power tranferred to the secondary, is given by

$$P_{ag} = \sum_n P_{ag}(n) - \sum_n F_x(n) \ \frac{\omega}{a\,n} \ . \qquad (98)$$

The secondary power loss equal to the heating losses in the secondary is

$$P_{sec} = \sum_n P_{sec}(n) = \sum_n F_x(n) \ \frac{s_n}{a\,n} \ . \qquad (99)$$

The form which these harmonic spectra takes is illustrated in Figure 6 for the TLRV operating at a speed of 300 MPH.

2.3.2 Mosebach One-Dimensional Computer Program

Choice of Fourier Cell Length ℓ and Maximum Harmonic Order NMAX

The Mosebach theory uses Fourier series expansions to describe the spatial distributions of airgap flux density and airgap function $y_2(x)$. These series are expanded on the basis of a periodic

length in the x direction equal approximately to some multiple of the motor (primary) length. Thus, $\ell = KP\ P\ \tau_p$ where KP is some integer greater than unity. The criteria for choosing ℓ is determined by the requirement that the flux density at the exit end of the motor cell be sufficiently attenuated so as to have negligible effect on the boundary conditions at the entrance end of the motor cell. A choice of cell (periodicity) length, which results in the flux being attenuated to one percent of its maximum value, is considered adequate. If ℓ is chosen larger than necessary to satisfy the above condition, the number of harmonics required to describe the Fourier distribution becomes unduly large leading to excessively high computing times.

The dependence of LIM motor characteristics on the choice of KP is illustrated in the table below in which LIM thrust, airgap power, and secondary power loss are computed for the TLRV LIM for KP = 2, 4, and 8. Motor conditions correspond to primary phase current of 530 amperes, excitation frequency of 165 Hertz, and speed equal to 300 mph. In order to include the same relative range of harmonics in the spectral distribution, the maximum harmonic order NMAX, was increased roughly proportional to KP. Sketches showing the airgap functions for the different values of KP are given in Figure 20.

The results given in Table 17 show that airgap power and secondary power loss are relatively insensitive to KP (cell length) while the thrust shows a functional dependence when KP varies from 2 to 4. For KP greater than 4, the motor output parameters vary only slightly, with no change being observed in LIM thrust. For all examples considered in Table 17, the cell length is sufficient to insure attenuation of the airgap flux density to one percent of maximum value.

NMAX specifies the range of harmonic orders, $-NMAX \leq n \leq NMAX$, required to describe the field and current distributions in the motor. Experience has shown that a value of NMAX equal to three times the harmonic order of peak flux density amplitude is generally adequate. Table 18 gives the TLRV LIM output parameters computed

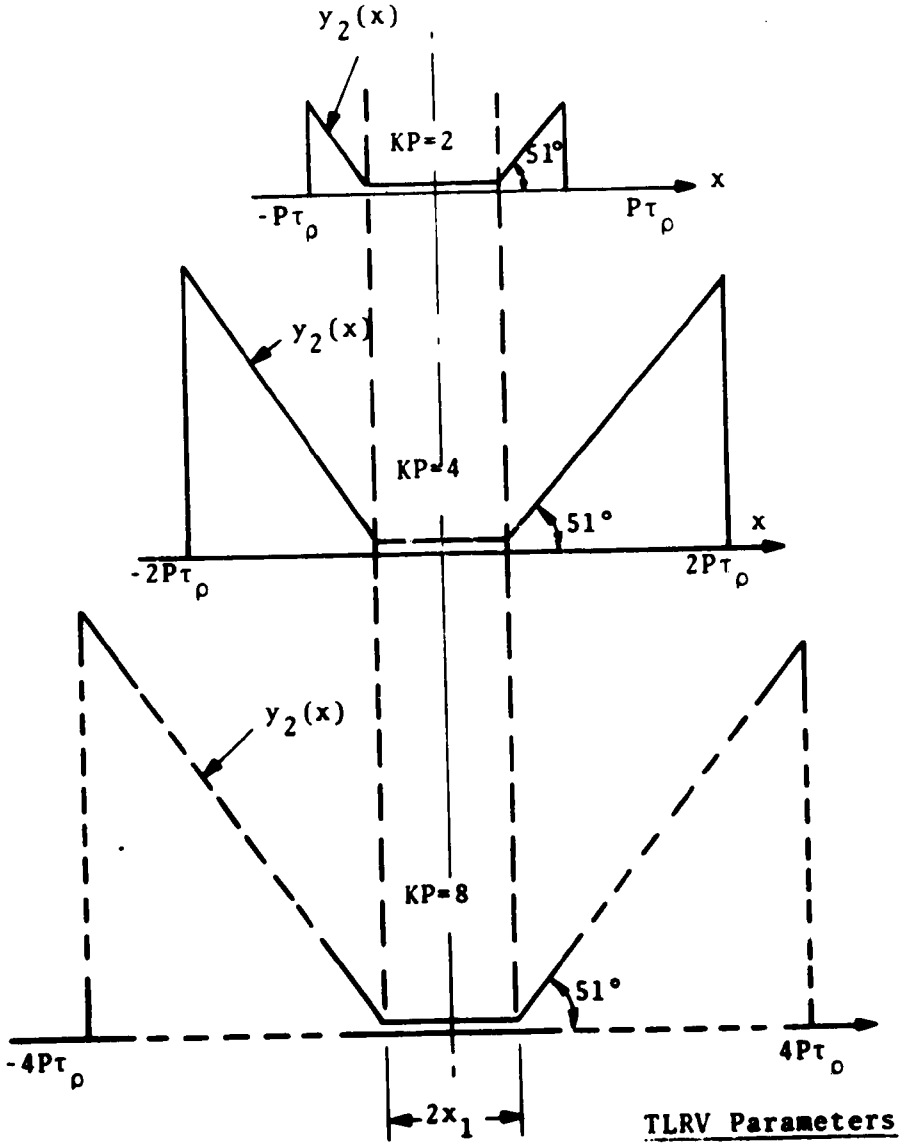

FIGURE 20. MOSEBACH AIRGAP FUNCTIONS FOR TLRV LIM

TABLE 17. TLRV OUTPUT PARAMETERS VERSUS NORMALIZED FOURIER CELL LENGTH

KP	NMAX	THRUST (N/side)	AIRGAP POWER (KW/side)	SECONDARY POWER LOSS (KW/side)
2	15	1569	668.66	458.16
4	25	1663	673.97	450.94
8	50	1663	670.30	449.21

TABLE 18. TLRV OUTPUT PARAMETERS VERSUS MAXIMUM HARMONIC ORDER

NMAX	THRUST (N/side)	AIRGAP POWER (KW/side)	SECONDARY POWER LOSS (KW/side)
8	4593	801.8	185.7
10	4550	800.6	190.3
16	4497	796.9	193.7
24	4481	797.1	196.1
50	4450	797.2	200.3

for five NMAX values for the LIM operated at 530 amperes/phase, an excitation frequency of 200 Hertz, and speed of 300 mph. With KP equal to two, the peak field and current harmonics corresponded to the fifth harmonic order. Table 18 shows that an increase in NMAX from 16 to 50 results in only a one percent change in thrust and an almost insignificant change in airgap power. The dependence of secondary power loss on NMAX is somewhat greater, due to the fact that a large number of harmonics is necessary to describe the sharp peak in secondary current which normally exists at the trailing edge of the LIM at high speeds.

The computed spectral distributions of flux density, thrust, airgap power, and secondary power are shown in Figure 21 for the motor conditions applicable to Table 18. The form of the spectral distribution suggests that little loss in accuracy results from

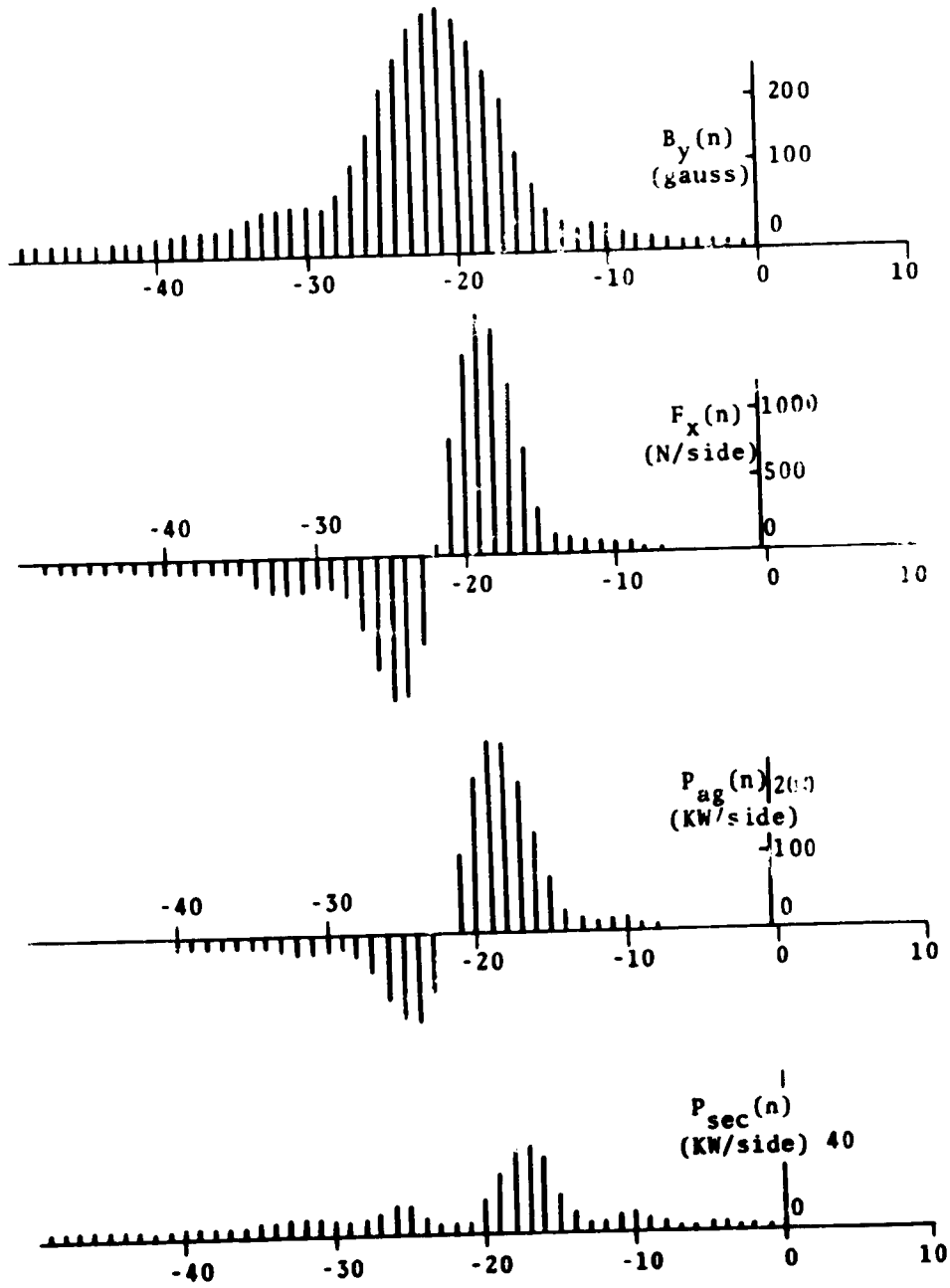

FIGURE 21. HARMONIC AMPLITUDES FOR TLRV LIM AIRGAP FLUX DENSITY, THRUST, AIRGAP POWER, AND SECONDARY POWER LOSS. (KP=8, MOTOR SPEED = 300 MPH, EXCITATION FREQUENCY = 165 Hz)

restricting the harmonic orders to negative values. In its present form, the Mosebach computer program sums over equal numbers of positive and negative harmonic orders so that some modification of the program to limit the region of harmonic summation would seem worthwhile.

2.3.3 Boundary-Effect Considerations

2.3.3.1 Magnetic End-Effect

The effect of the finite length of primary iron (core) on LIM performance or so-called magnetic end-effect, can be important at high motor speeds and low slip-frequencies. The magnetic end-effect is examined in this section using the example of the TLRV operating at rated speed and stator current excitation. Two LIM models are considered: the first has a finite length primary iron (Model A) and the second has continuous primary iron (Model B). The difference in LIM characteristics of the two models describes the effect of the limited iron length on motor performance.

The TLRV output characteristics are computed at rated speed (300 mph) and stator current (530 amperes/phase) as a function of excitation frequency. Motor parameters required for the calculations are summarized in Table 20. To insure convergence of the Fourier series for the case of the continuous primary iron (Model B), it is necessary to increase the length of the periodic cell to about eight times the length of the primary winding. The computer parameters used in the calculations are given below:

MODEL	KP	NMAX
A	2	15
B	8	50

Figure 22 presents the LIM thrust for Models A and B as a function of stator excitation frequency. The magnetic end-effect as represented by the difference in the curves becomes quite small above 200 Hz but has a large effect at lower frequencies. Thus, at a frequency of 165 Hz corresponding to a slip of 0.0928, LIM thrust is reduced approximately fifty percent by magnetic end-effect.

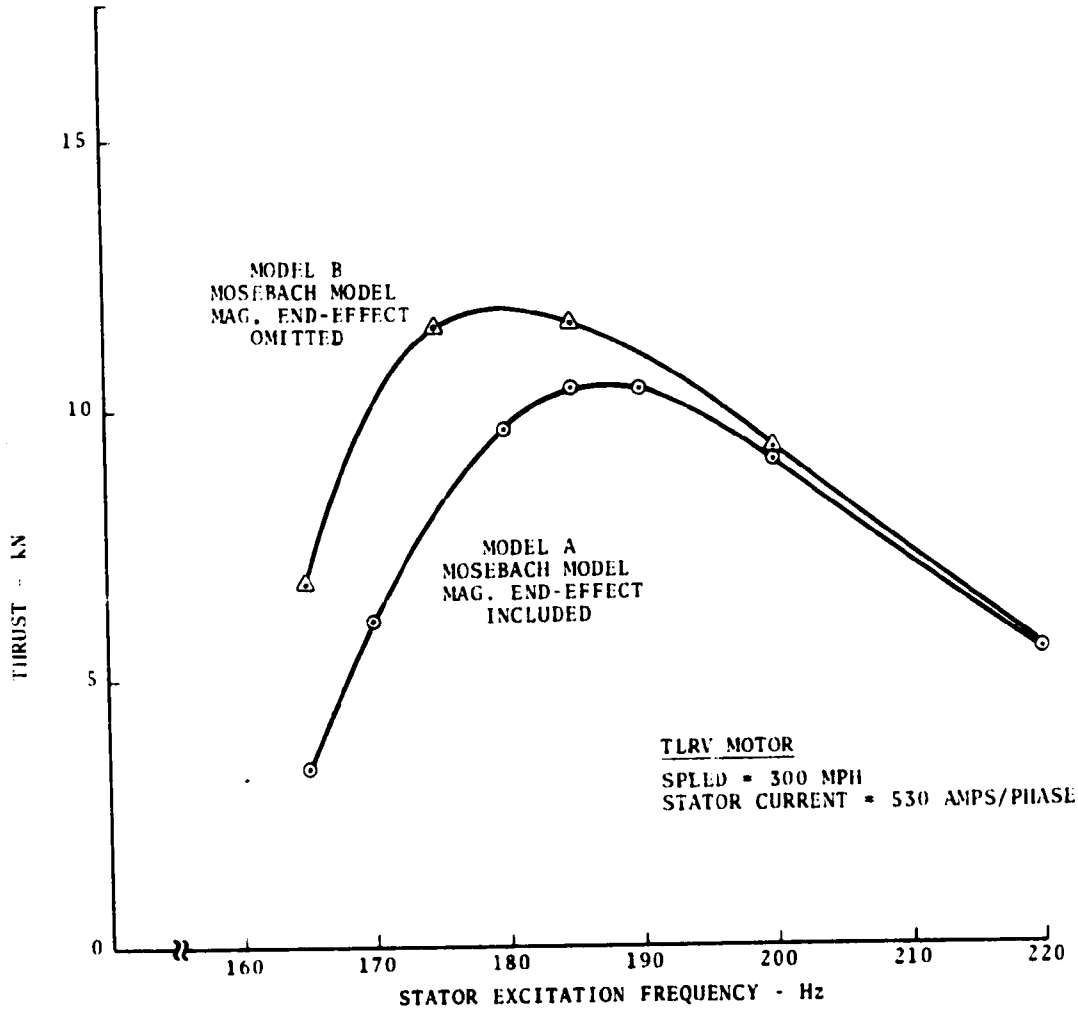

FIGURE 22. TLRV THRUST PREDICTED BY MOSEBACH THEORY WHEN MAGNETIC END-EFFECTS ARE INCLUDED AND NEGLECTED IN LIM MODEL

Figure 23 presents the airgap power P_{ag}, mechanical power P_m, and secondary power P_{sec} predicted by the Mosebach theory for finite length and continuous primary iron models. Airgap power is almost unaffected by the length of the primary iron core, in contrast to the mechanical and secondary powers which are considerably affected by the length of the primary iron. This suggests that magnetic end-effects do not affect the total real power to the motor but, alter the division of this power into usable mechanical work and secondary power loss (heating).

The power factor was also computed for the same set of conditions applicable to Figures 22 and 23. The change in power factor with magnetic end-effect included was relatively small, and typically increased four percent at a slip of .0928. The results suggest that LIM real and reactive power components are insensitive to the extention of iron beyond the region of the primary winding.

The airgap flux density along the longitudinal (x) axis of the motor is insensitive to magnetic end-effect within the primary ($-x_1 \leq x \leq x_1$) but can be strongly dependent on magnetic end-effect in the region outside the primary ($x \geq |x_1|$). Figure 24 shows the flux density amplitude computed for the TLRV at 300 mph (530 amperes/phase, 165 Hz) for continuous primary ferromagnetic region and a finite ferromagnetic region given by the actual core size. The trailing flux density in the exit end of the LIM attenuates exponentially with distance in both cases. This is illustrated in Figure 25 in which the log of the flux density amplitude is plotted against distance along the x axis. The linear slopes of these flux attenuation characteristics yield the attenuation constants given below. Also shown is the corresponding attenuation constant predicted by the Yamamura theory[2] for the case of continuous primary iron.

	Mosebach Model	Yamamura Model
Continuous iron primary	$0.211m^{-1}$	$0.25m^{-1}$
Finite iron primary	$1.61m^{-1}$	-

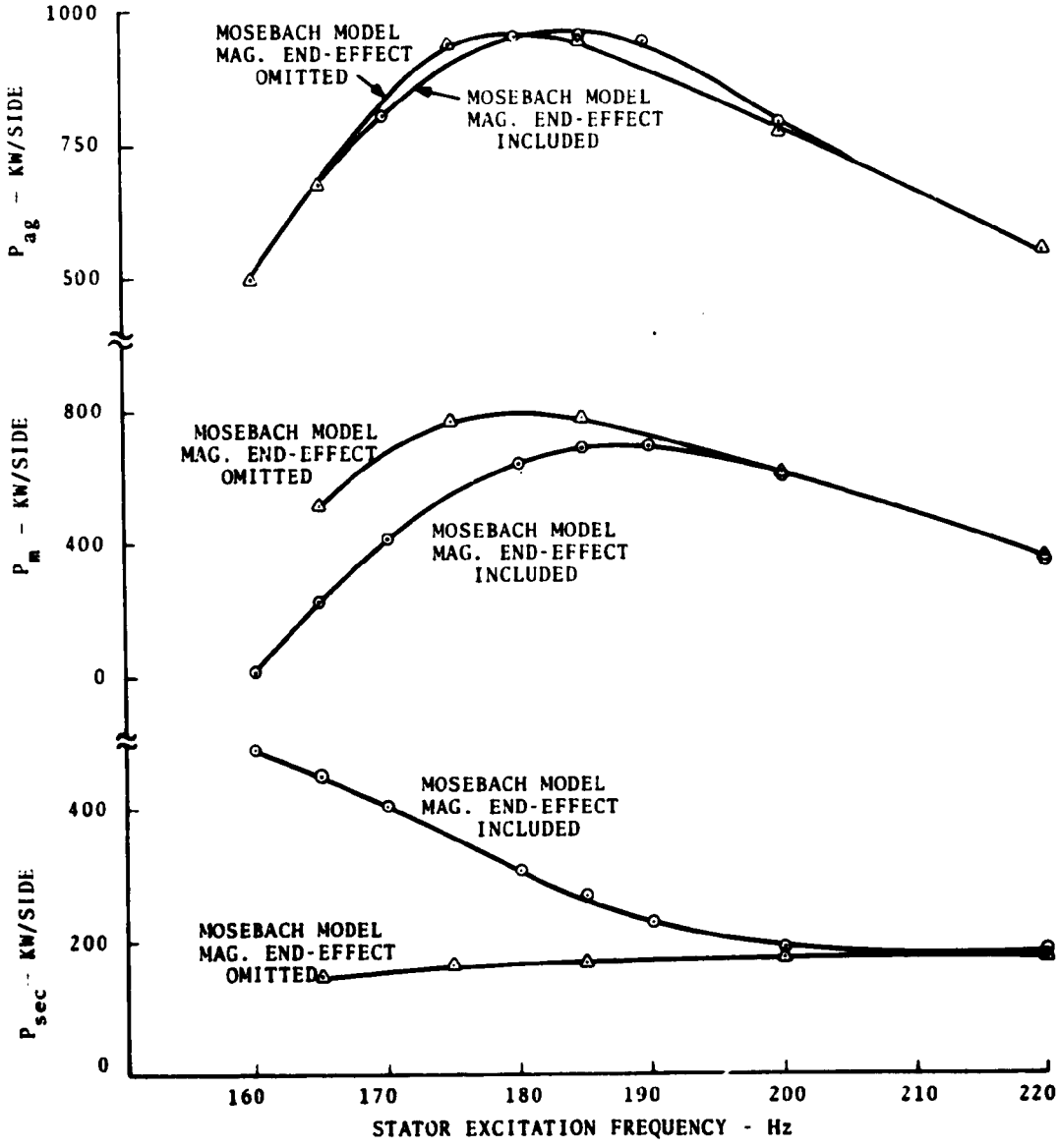

FIGURE 23. TLRV AIRGAP POWER, MECHANICAL POWER, AND SECONDARY POWER PREDICTED BY MOSEBACH THEORY WHEN MAGNETIC END-EFFECTS ARE INCLUDED AND NEGLECTED IN LIM MODEL

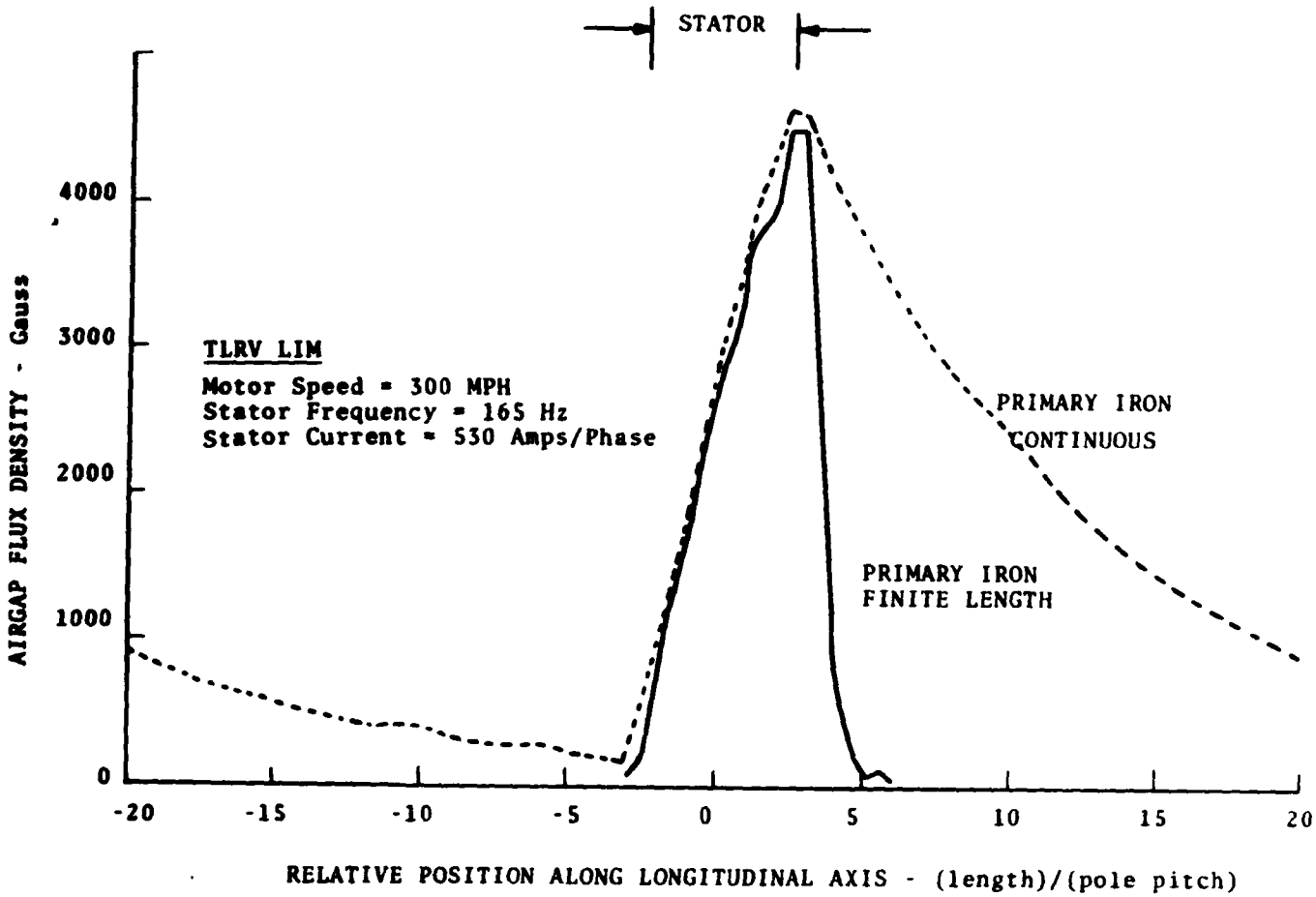

FIGURE 24. TLRV FLUX DENSITY PREDICTED BY MOSEBACH THEORY WHEN MAGNETIC END-EFFECTS ARE INCLUDED AND NEGLECTED IN LIM MODEL

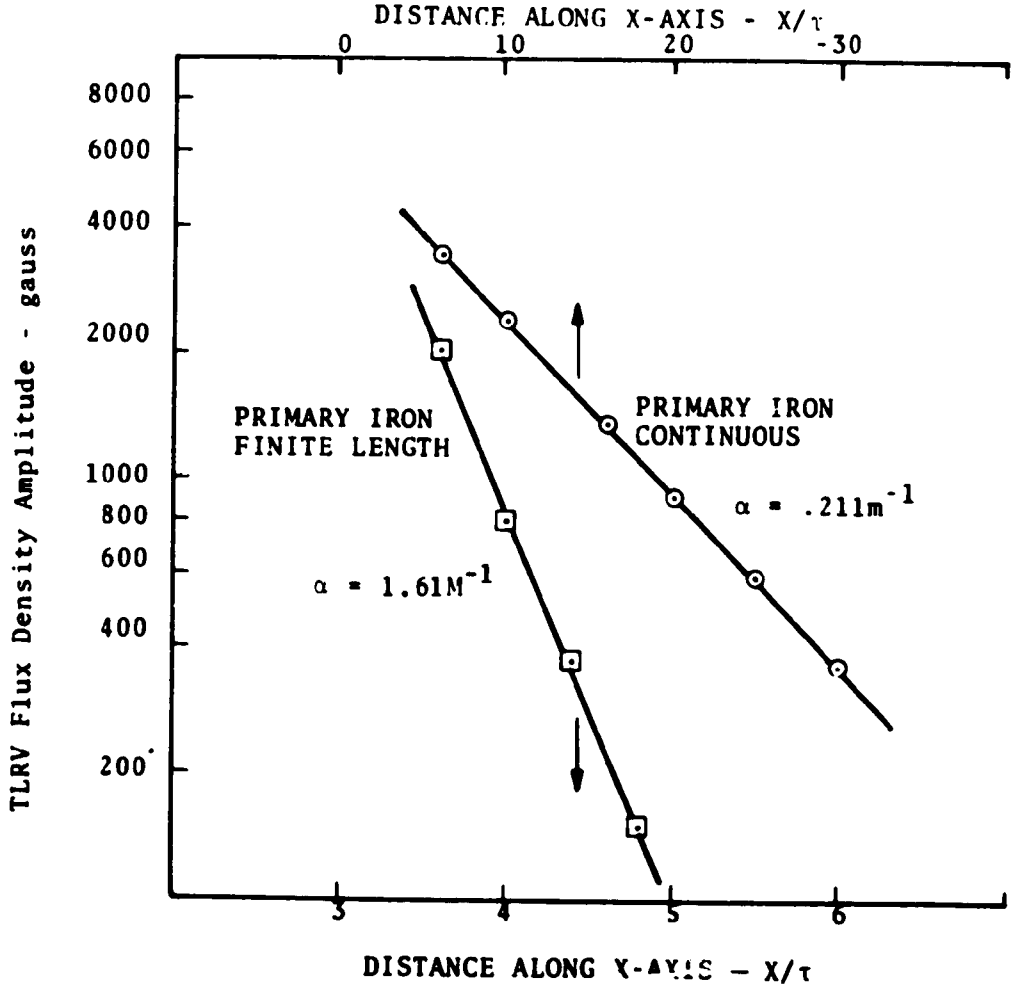

FIGURE 25. TLRV TRAILING FLUX DENSITY AMPLITUDE PREDICTED BY MOSEBACH THEORY WITH AND WITHOUT MAGNETIC END-EFFECT

2.3.3.2 Transverse Edge-Effect: Mosebach Versus Bolton Treatments

The Mosebach treatment of the transverse edge-effect differs considerably from the approach used by Bolton.[4] In the Mosebach one-dimensional model, the actual secondary overhang is replaced by ficticious sidebars which serve to conduct all the longitudinally directed currents flowing in the secondary. The secondary current is also assumed to flow in rectangularly-shaped patterns (Figure 19a. These flow patterns remain independent of frequency so that the mutual coupling (inductance) between primary and secondary is independent of frequency. Changes in the secondary impedance (as seen by the primary) are then identified with changes in the secondary leakage inductance and secondary resistance, rather than with changes in the secondary magnetizing inductance and secondary resistance. In the Bolton model, the finite secondary width does not cause any restriction in the secondary current paths. Secondary currents flow in patterns described by Bolton as 'television screen' or 'distorted television screen' shaped patterns. These flow patterns change with slip frequency in order to accommodate flow paths of minimum secondary reactive impedance. In terms of equivalent circuit parameters, this requires a slip-dependent mutual inductance and secondary resistance.

The secondary current flow pattern was computed by Mosebach using a two-dimensional theory which allows for unrestricted current flow in the x, z plane. His results are shown in Figure 26 for two values of effective Reynolds number (r's). For large r's, the flow pattern is nearly rectilinear and similar to the flow lines shown sketched in Figure 19a. For r's equal to five, a more nearly television-screen type pattern results. Since the one-dimensional Mosebach theory is restricted to rectilinear-type flow patterns, it should yield more accurate results when applied under conditions of large effective Reynolds numbers.

The Mosebach treatment of the transverse edge-effects leads to an effective secondary conductivity σ^*, which depends on the longitudinal harmonic order n,

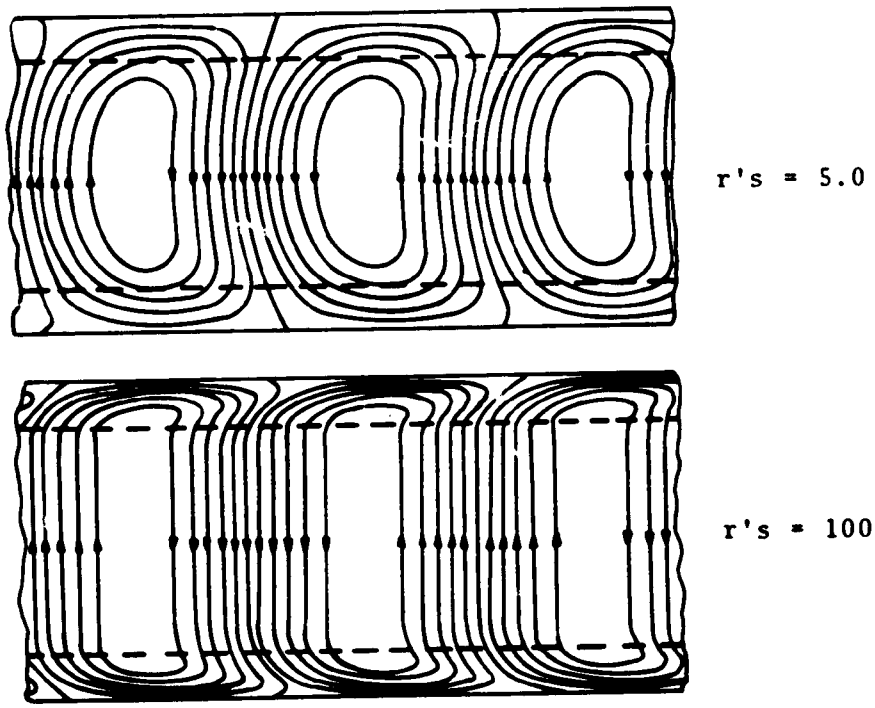

FIGURE 26. SECONDARY CURRENT FLOW AS PREDICTED BY MOSEBACH TWO-DIMENSIONAL THEORY

$$\sigma^* = \frac{\sigma}{1 + z_1 d_s a^2 n^2} \quad . \tag{100}$$

The effect of the sidebars is contained in the term in the denominator which is a function of the overhang distance d_s, the half-core width z_1, and wave vector amplitude a n. Since the overhang distance d_s cannot be zero in the Mosebach model, as otherwise there remains no return path for the secondary currents, this poses a problem in treating LIMs with zero or near-zero overhand distances.

The Bolton treatment of the transverse edge-effect leads to an effective secondary resistance in parallel with an effective magnetizing reactance given by

$$R_2' = K_2 \cdot R_2$$

$$X_m' = K_1 \cdot X_m$$

where K_1 and K_2 are defined by,

$$K_1 = K_x \frac{1 + s^2 G^2 K_R^2 / K_X^2}{1 + s^2 G^2} \qquad K_2 = \frac{K_X}{K_R} K_1 \quad .$$

For the TLRV operating at 165 Hz, K_1 varies from 1.0 to 0.4 as the slip goes from 0.0 to 1.0, and K_2 varies from 2.47 to 2.72 as the slip goes from 0.0 to 1.0. The latter range of parameter values is to be compared with the denominator of Equation (100) which equals 2.32 evaluated at the harmonic order of peak flux density amplitude. (For KP equal to two, the peak flux density harmonic occurs at n equal to five.)

In the Yamamura theory of linear induction motors,[2] the Bolton factors K_1, K_2 are used to correct for the finite width of the LIM, but in a different manner than used by Bolton in his analysis. The Yamamura treatment assumes X_m remains constant and secondary conductivity is modified by the factor K_1/K_2. In addition the primary current density is replaced by K_1x (primary current density. When applied correctly, the Yamamura treatment is equivalent to that of Bolton.

It is interesting to compare the different results which would have been obtained had the Bolton factors been used in place of Equation (100) to compensate for edge-effect. Table 19 gives the thrust and airgap power for the TLRV computed for two slips using the two different methods for treating edge-effect. To provide a further comparison with Yamamura's treatment, the LIM model was assumed to comprise a continuous primary iron. The Bolton correction was applied to the Mosebach results by setting $\sigma^* = \sigma$, and replacing the secondary conductivity by $(K_1/K_2 \cdot \sigma)$, taking care to correct the final results for the reduced primary current density using the K_1 factor as described above. Both methods yield almost the same thrust value at s = .0928 but give somewhat poorer agreement at s = 1.0. This is not surprising since the edge-effect correction is greater at high slip-frequencies and large values of slip. For comparison, the thrust and airgap power computed with the Yamamura theory is given in Table 19. It is interesting that the Yamamura results tend to lie midway between those computed via the Mosebach theory using the two methods for correcting edge-effect. The exception to this is the thrust computed for slip of 0.0928.

TABLE 19. TLRV THRUST AND AIRGAP POWER COMPUTED USING THE MOSEBACH AND BOLTON METHODS FOR EDGE-EFFECT CORRECTION (Included in table are results obtained using Yamamura theory with Bolton methods for edge-effect correction)

	Edge Correction	Thrust (n/side)		Airgap Power (KW/side)	
		Mosebach	Yamamura	Mosebach	Yamamura
s=.0928	Mosebach: Eq'n 46	3398	-	674	-
	Bolton: K_1, K_2	3380	3621	600	634
s=1.0	Mosebach: Eq'n 46	1201		183	
	Bolton: K_1, K_2	1421	1299	208	195

2.3.3.3 Further Boundary-Effect Considerations

LIM characteristics are altered in varying amounts by the finite size of the primary winding and primary iron core structure. In this section, the cumulative effects of finite primary current winding and finite primary iron core on the TLRV thrust-versus-slip characteristics are examined.

Four different LIM models were considered for this purpose having boundary limiting characteristics as shown below. Model A corresponds to an 'ideal' LIM having no boundary limitations, while Model D describes a LIM having finite primary winding and finite length of iron core. Models B and C describe configurations with boundary limitations intermediate between those of Model A and D.

Model	Primary Winding	Primary Ferromagnetic Region
A	Infinite in x,z plane	Infinite in x,z plane
B	Finite in x-dir. Infinite in z-dir.	Infinite in x,z plane
C	Finite in x-dir. Finite in z-dir.	Infinite in x,z plane
D	Finite in x-dir. Finite in z-dir.	Finite in x-direction Infinite in z-direction

The LIM thrust computed as a function of motor slip is shown in Figure 27 for the different models. In the absence of boundary limitation effects, Model A predicts a peak thrust approaching 51 kilonewtons at a slip near 0.01. The finite length of primary winding (Model B) mainly causes a reduction in thrust at slips below 0.2. Limiting the width of the primary winding (Model C) results in a large increase in thrust over the full range of slips, while the addition of finite ferromagnetic primary (Model D) reduced thrust at slips below 0.2, in a manner not dissimilar to that produced by the finite length of primary winding.

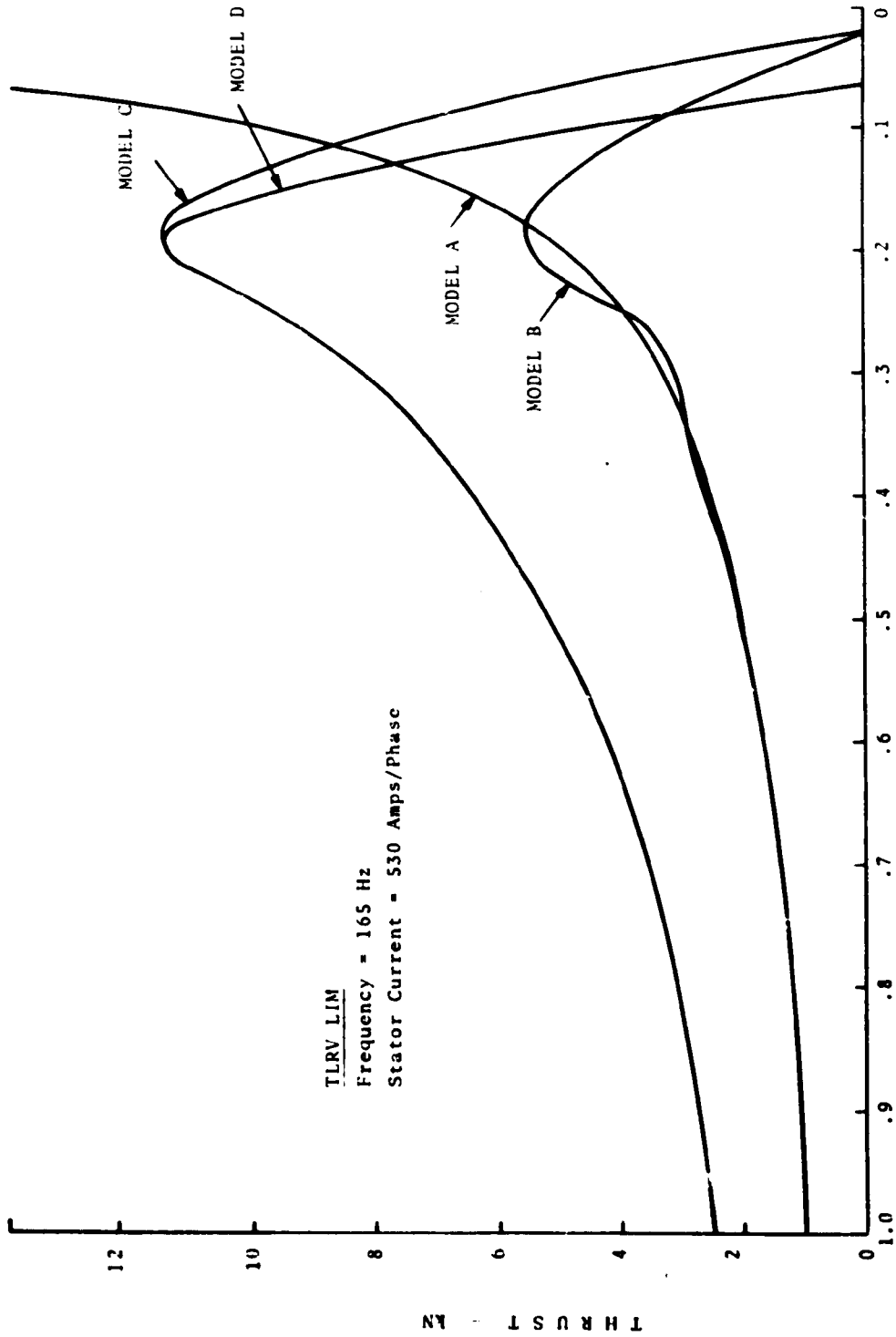

FIGURE 27. TLRV THRUST PREDICTED BY MOSEBACH THEORY FOR DIFFERENT BOUNDARY PERTURBATIONS

2.3.4 Mosebach Model Applied to TLRV & LIMRV LIMs

The thrust predicted by the Mosebach one-dimensional LIM model is compared with similiar predictions based on the mesh-matrix model. Both the Mosebach and the mesh-matrix models take into account the finite length of the stator (iron) core. The main difference between the two models lies in the mathematical solution for the field quantities. The Mosebach theory describes the field in terms of Fourier series; the mesh-matrix theory uses discrete elements to describe the continuous secondary structure and computes field quantities using a summation of contributions from discrete elements along the length of the motor. In assigning equivalent circuit parameter values to the mesh elements, Elliott adjusts the sidebar resistance so that the total mesh circuit resistance is equal to the resistance value given by the Bolton edge-effect analysis. Since the equivalent Bolton secondary resistance with edge-effect included is derived for a fundamental excitation wave only and neglects end-effect contributions, it cannot describe accurately effects occuring with higher-order harmonic excitations and field distributions. Since the differences in motor characteristics predicted by the Mosebach and mesh-matrix models depends on the above factors which are difficult to quantify, the comparison of results of the two methods are presented without any attempts to explain causes for differences between the predicted results.

The LIM parameters describing the TLRV and LIMRV motors are given on the next page. The values of primary core separation (air gap) and secondary thickness include corrections for the Carter factor and structural (web-like) characteristics of the secondary. The widths of the secondaries are adjusted to compensate for asymmetrical positioning of the secondaries relative to the primaries using the theory of Bolton.[7]

TABLE 20. TLRV LIM PARAMETERS IN MOSEBACH MODEL

Turns per Coil (N) = 4
Pole Pitch (τ_p) = 0.448 m.
Core Width (2c) = 0.1905 m.
Poles (P) = 5
Core Length (ℓ_s) = 2.56 m.
Air Gap (g) = 0.0171 m.*
Phases (m) = 3
Slots per Phase (q) = 5
End Half-filled Slots (ε) = 5
Secondary Thickness (b) = 0.0066 m.
Secondary Resistivity (p) = 0.416×10^{-7} ohm-m.
Periodic Cell Length ($KP^*\tau_p$) = 4.48 m.
Maximum Order of Harmonics (NMAX) = ± 50

TABLE 21. LIMRV LIM PARAMETERS IN MOSEBACH MODEL

Turns per Coil (N) = 1
Pole Pitch (τ_p) = 0.355 m.
Core Width (2c) = 0.254 m.
Poles (P) = 10
Core Length (ℓ_s) = 3.81 m.
Air Gap (g) = 0.024 m.*
Phases (m) = 3
Slots per Phase (q) = 5
End Half-filled Slots (ε) = 5
Secondary Thickness (b) = 0.0071 m.
Secondary Resistivity (p) = 0.416×10^{-7} ohm-m.
Periodic Cell Length ($KP^*P^*\tau_p$) = 7.08 m.
Maximum Order of Harmonics (NMAX) = ± 43

*Includes Carter Factor

2.3.4.1 TLRV LIM Thrust at Rated Speed

The TLRV thrust versus stator excitation frequency is shown in Figure 28 for the one-dimensional Mosebach model. The dashed curve describes the corresponding thrust predicted by the mesh-matrix model. The Mosebach theory predicts motor thrust to decrease rapidly to zero as the slip-frequency is lowered from 185 Hz to 160 Hz. This rapid decrease in thrust with slip-frequency is partly due to the finite length of the primary iron core which generates end-effect waves which reduce the net thrust developed by the LIM. Both the Mosebach and mesh-matrix models predict a thrust decaying rapidly to zero near 160 Hz; however, the peak thrust predicted by the Mosebach model lies about 20 percent above that predicted by the mesh-matrix model. This latter is consistent with similiar results obtained using the Oberretl and Yamamura computer models, which give peak LIM thrusts in excess of that predicted by the mesh-matrix model.

2.3.4.2 LIMRV LIM Thrust at Rated Speed

The LIMRV thrust versus excitation frequency is shown in Figure 29. The mesh-matrix prediction agrees with the Mosebach predicted except in the region of peak thrust, where the mesh-matrix result is characteristically below that of Mosebach as well as other predictions. The somewhat better agreement between the Mosebach and mesh-matrix predictions for the LIMRV as compared with the TLRV is probably the result of reduced end-effect interactions in the LIMRV compared with that of the TLRV.

2.3.5 Summary of Mosebach Theory Applied to TLRV & LIMRV LIMs

Magnetic end-effects caused by the finite length of primary core are shown to degrade TLRV LIM performance under conditions of high motor speed and low slip. This phenomena has certain characteristics similar to those associated with the MMF end-effect, high motor speed, and low slip. Under such conditions, the total real power delivered to the motor remains constant but the fraction converted in usable mechanical power is reduced. This is

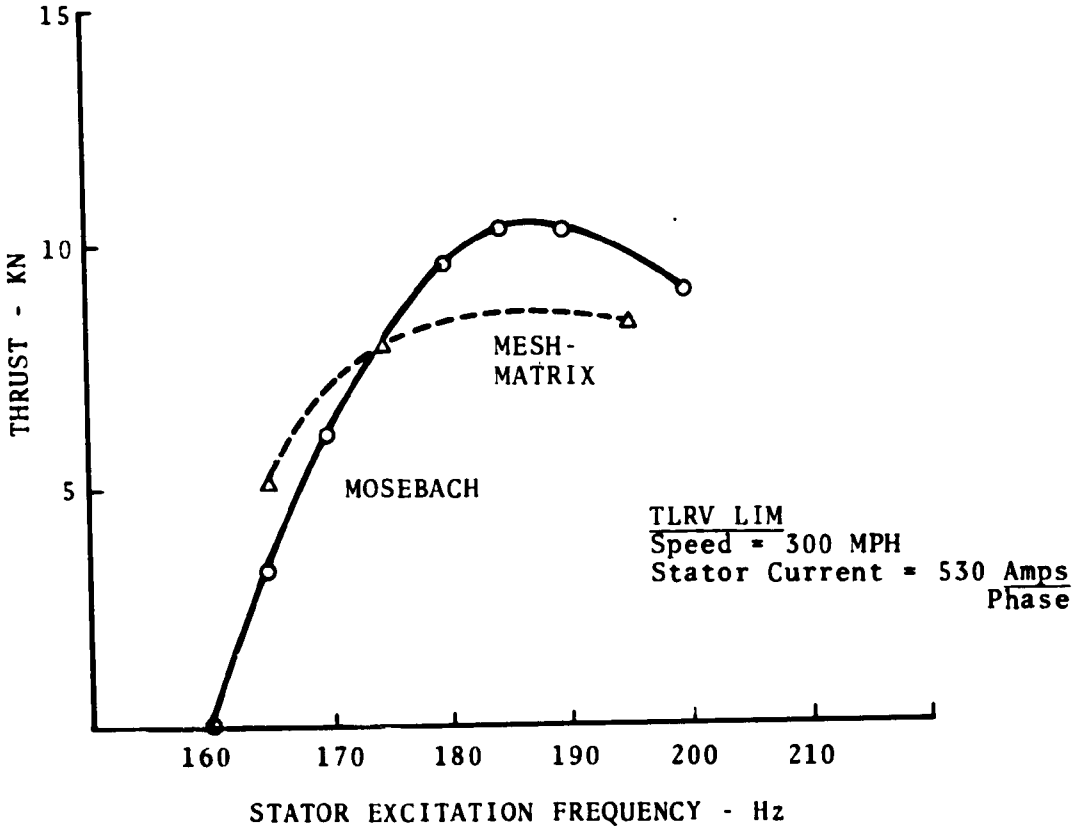

FIGURE 28. TLRV LIM THRUST AS PREDICTED BY MOSEBACH THEORY

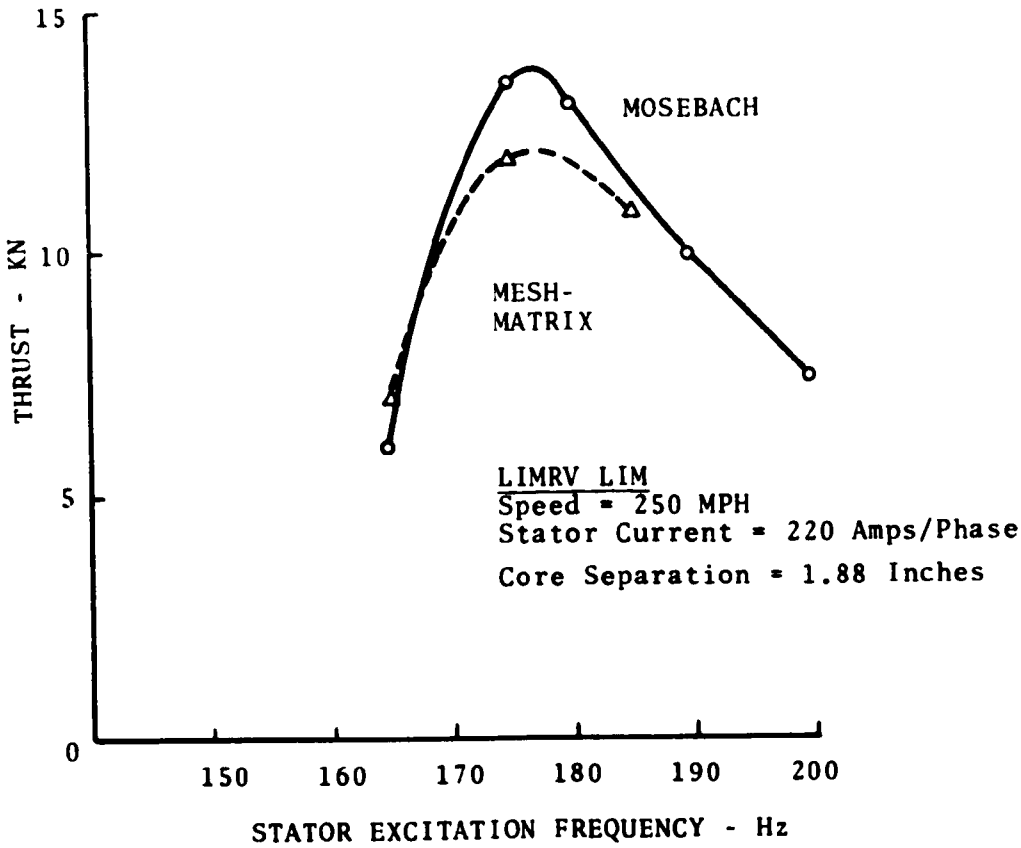

FIGURE 29. LIMRV LIM THRUST AS PREDICTED BY MOSEBACH THEORY

reflected in a drop in motor efficiency at high speeds. For the TLRV operating at rated speed (300 MPH) and a slip of about 1/10, theory predicts a drop in motor efficiency from 77 to 33 percent due to magnetic end-effects.

The TLRV and LIMRV thrust-versus-frequency characteristics were computed for rated motor speeds using the Mosebach (one-dimensional) computer program and compared with the corresponding predictions given by the mesh-matrix program. At high slip-frequencies, the agreement was fairly good with the maximum spread in thrust amounting to less than ten percent. Magnetic end-effect was observed to be considerably more promounced in the TLRV LIM than in the LIMRV LIM, a result due to the characteristicly higher speed of the TLRV LIM.

Constant input voltage calculations were made for the LIMRV LIM at five different motor speeds. The computed Mosebach thrusts were compared with thrust data obtained from test runs at Pueblo, Colorado. At speeds of 140 and 178 MPH, the predicted thrusts were within three percent of measured thrusts and at low speeds, within ten percent of measured thrusts. Similar calculations performed on a constant input <u>current</u> basis gave somewhat poorer agreement at the higher motor speeds than those on a constant <u>voltage</u> basis.

2.4 COMPARISON OF OBERRETL, YAMAMURA, AND MOSEBACH COMPUTER MODELS AS APPLIED TO THE TLRV & LIMRV LIMS

The previous sections have described the Oberretl, Yamamura, and Mosebach LIM models and the application of the respective computer predictions for the TLRV and LIMRV motors will be reviewed with an attempt to identify any significant differences in motor performance as predicted by the three theories.

The motor parameters used in the calculations have been previously listed in tabular form in the sections describing the different LIM models. The values for the air gap (g) include the Carter Factor correction, which amounts to a 14 percent correction for the core-to-core separation in the LIMRV LIM and a 7 percent correction for the core-to-core separation in the TLRV LIM.* The calculations of LIMRV thrust given in this section use a value of electrical conductivity for 6061-T6 aluminum alloy equal to 47.7 percent as compared with the value of 43 percent used in the previous LIMRV calculations. This revised value reflects the results of more recent measurements of 6061-T6 conductivity which indicates it is considerably higher than originally reported.

2.4.1 LIMRV Thrust at 5, 40, 80, and 112 M/S

Figures 30-33 show LIMRV motor thrust as computed for motor speeds of 5, 40, 80, and 112 M/S. The core spacing for these motor characteristics was 1.5 inches as compared with the core spacing of 1.875 inches used in the previous LIMRV calculations. Stator current was 2200 amperes per phase corresponding to 1100 amperes per phase per LIM half.

The computed thrust using the Oberretl theory is consistently lower than that computed using the Yamamura and Mosebach theories. This is particularly noticeable at the lower motor speed range where the LIM thrust using the Oberretl theory lies about 14 percent below the average peak thrust predicted by the Yamamura and Mosebach theories. Since end-effect is not significant at

*Carter factor values supplied by Dr. D. Elliott .

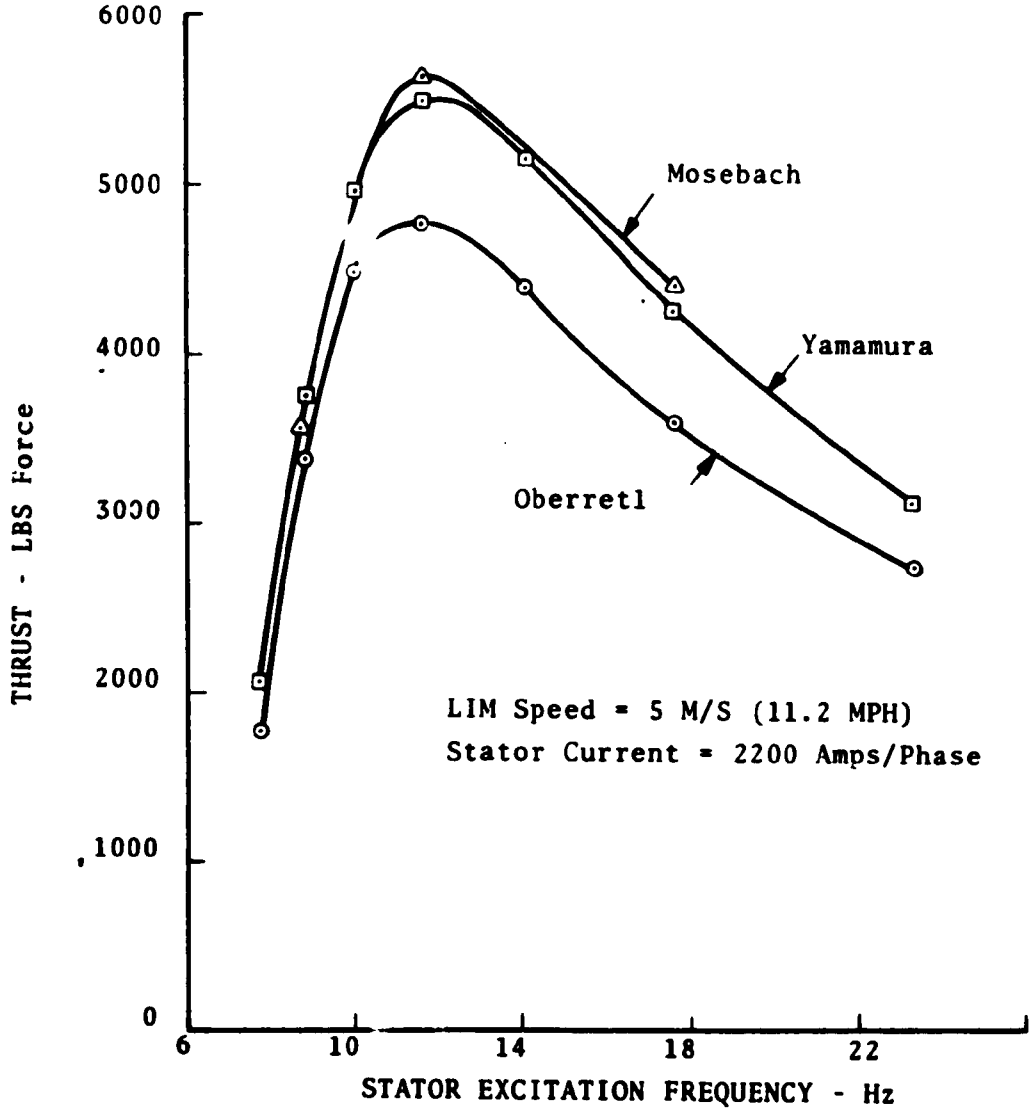

FIGURE 30. LIMRV THRUST AT 5 M/S AS PREDICTED BY THREE LEADING THEORIES

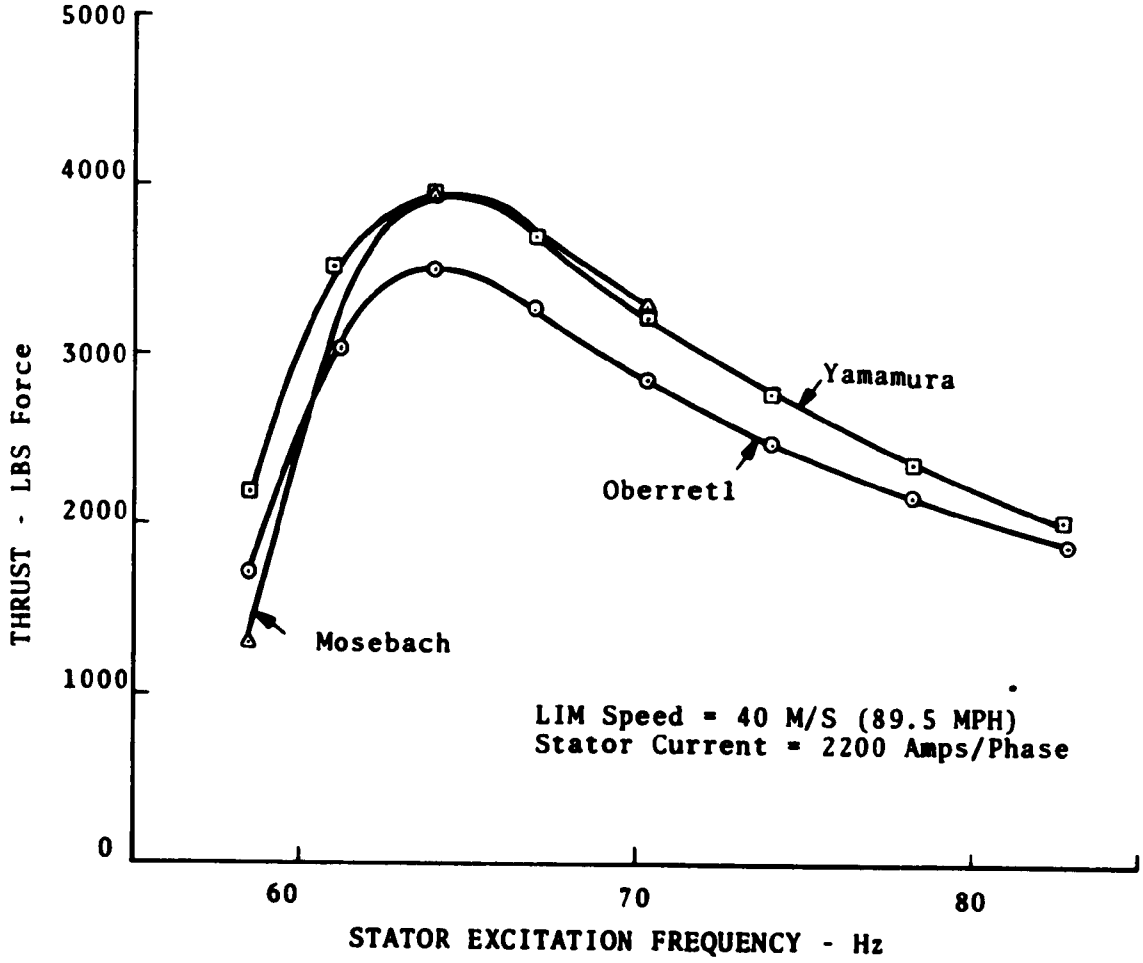

FIGURE 31. LIMRV THRUST AT 40 M/S AS PREDICTED BY THREE LEADING THEORIES

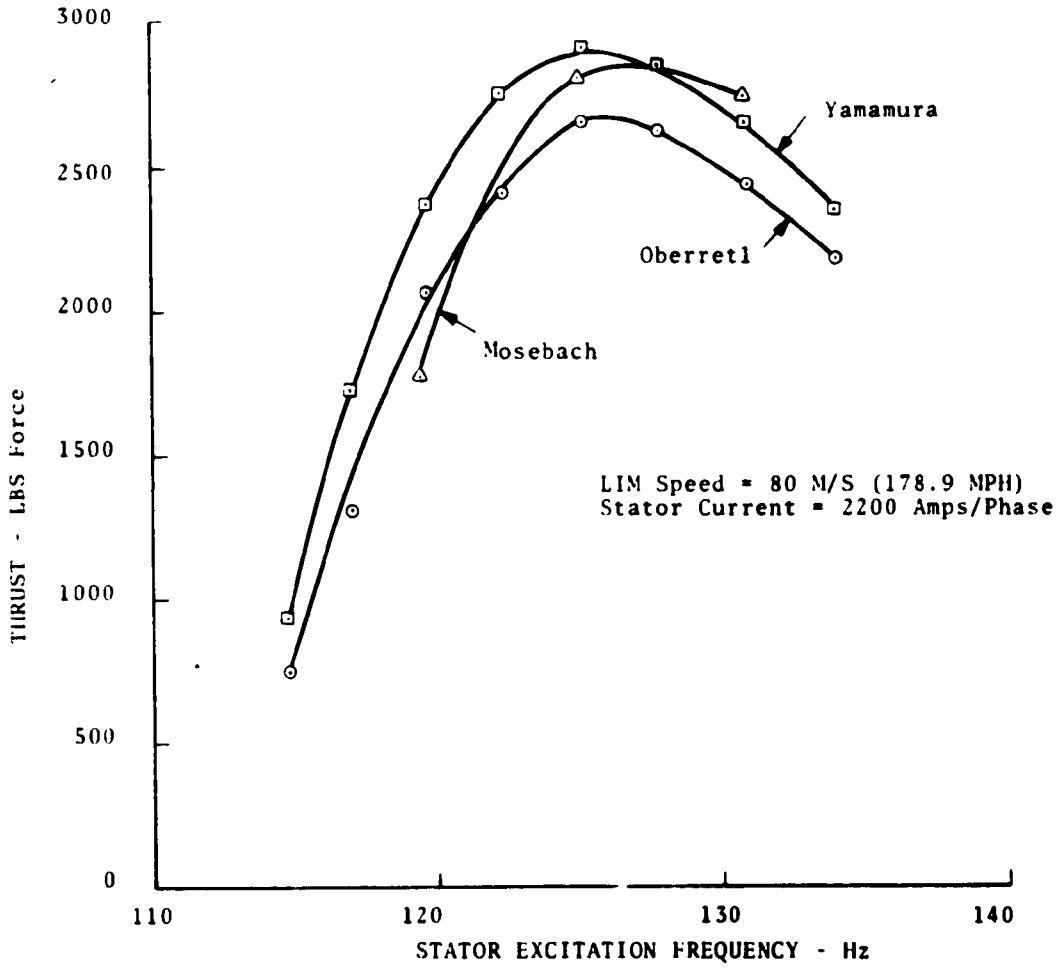

FIGURE 32. LIMRV THRUST AT 80 M/S AS PREDICTED BY THREE LEADING THEORIES

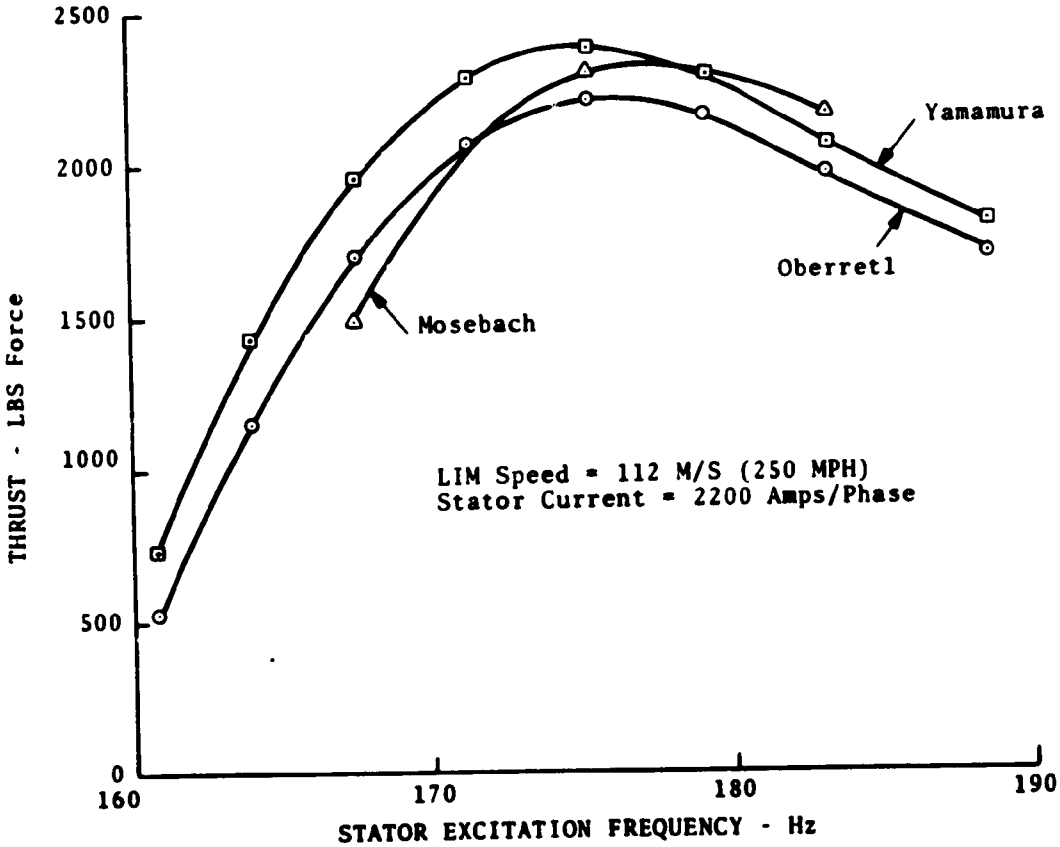

FIGURE 33. LIMRV THRUST AT 112 M/S AS PREDICTED BY THREE LEADING THEORIES

the lower speed range, this difference is probably associated with the Oberretl treatment of the edge-effect which allows the primary ferromagnetic region to extend beyond the stator width and thereby alters the boundary conditions at the motor sides. At higher motor speeds, somewhat better agreement exists between the Oberretl and the Yamamura, Mosebach predictions. At a motor speed of 112 M/S (250 MPH), the three theories yield predicted thruststhich vary by only 7 percent.

A study of the LIM characteristics shows that the Mosebach model leads to a larger thrust reduction at higher speeds than do the Yamamara and Oberretl models in the lower slip-frequency range. This could be associated with the magnetic end-effect associated with the finite length of the primary core range. This reduction in thrust is associated with the end-effect arising from the finite length of the primary core structure. Since only the Mosebach model includes this refinement of finite core length, a similiar reduction in thrust is not predicted in the other two theories. A comparison of the motor thrust in the four speed ranges shows a progressive reduction in LIM thrust at higher motor speeds at slip-frequencies below that associated with the peak thrust of the motor.

It is interesting to note that the Yamamura model leads to larger thrusts at low slip-frequencies than do the other two models. It is in this region that end-effect becomes most pronounced. Since the Bolton correction factor which Yamamura uses to take into account edge-effect neglects end-effect in its derivation, one would expect the Yamamura LIM theory to yield thrust predictions different from those given by Oberretl or Mosebach in the region of high speeds and low slip frequencies.

The locus of peak thrust is shown plotted in Figure 34 using the values gives in Figures 30-33. Included in peak thrust characteristic is the prediction based on the mesh-matrix method. Two values of measured thrust are also indicated on the figure. The measured thrust exceeds the predicted thrust by about 400-450 pounds. The source of this discrepancy is not presently known.

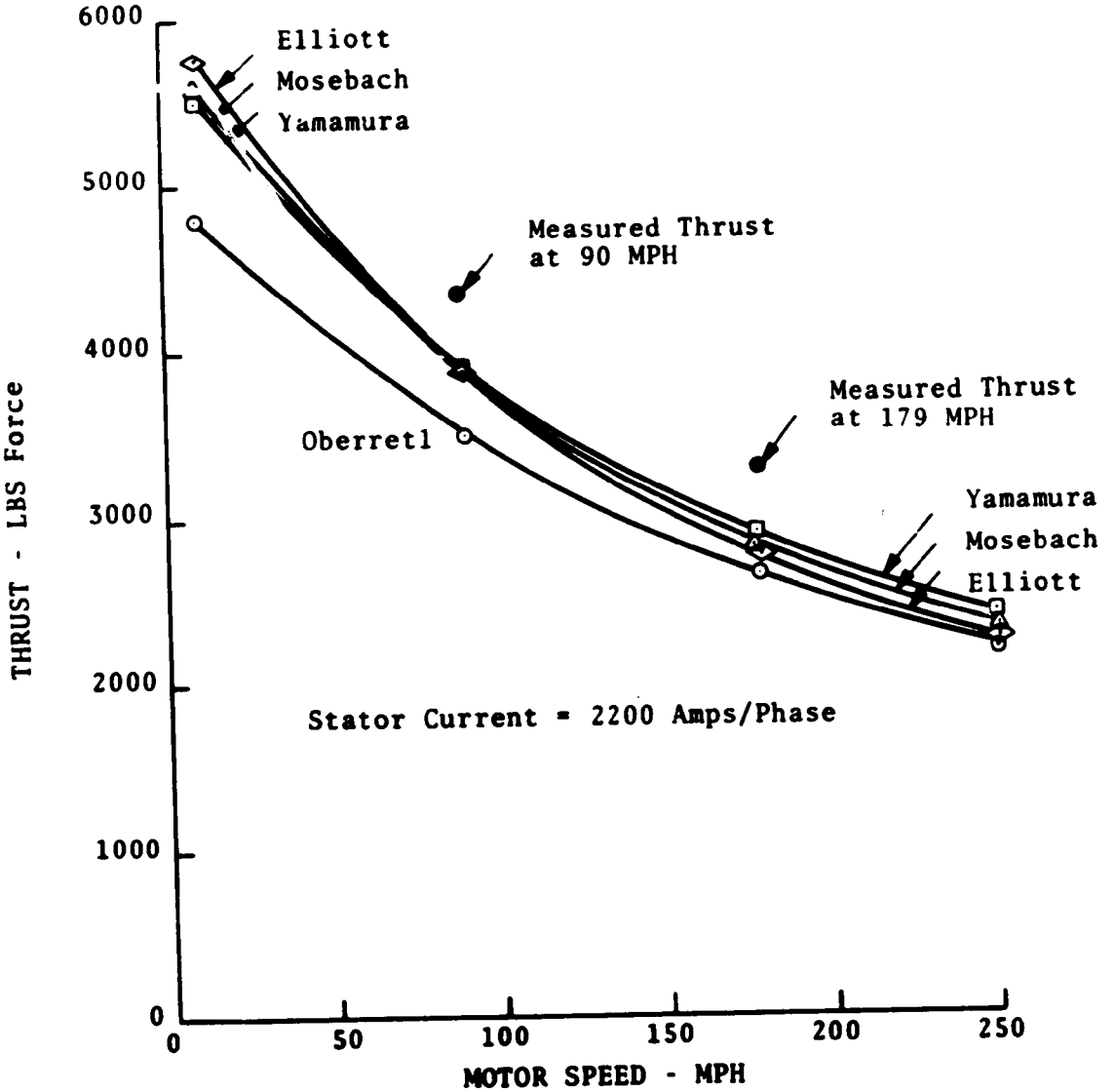

FIGURE 34. MAXIMUM LIMRV THRUST THAT CAN BE DEVELOPED AT VARIOUS SPEEDS AS PREDICTED BY FOUR LEADING THEORIES

The use of a lower conductivity value for the secondary would improve the agreement with measured data.

2.4.2 TLRV LIM Thrust at Rated Speed

The TLRV trust as predicted by the Oberretl, Yamamura, Mosebach, and mesh-matrix theories is shown in Figure 35. Above 185 Hz, the Oberretl, Yamamura, and Mosebach theories give predicted thrusts which are in fair agreement, with the maximum divergence amounting to ten percent. Below 185 Hz, the Mosebach prediction drops off sharply reflecting the added thrust reduction due to the finite length of the stator core. This trust reduction associated with the magnetic end-effect is more prounced than with the LIMRV LIM due to the higher LIM speed and reduced electrical length of the TLRV LIM compared with the LIMRV LIM. The peak thrust predicted by the mesh-matrix method lies below that predicted by the other theories.

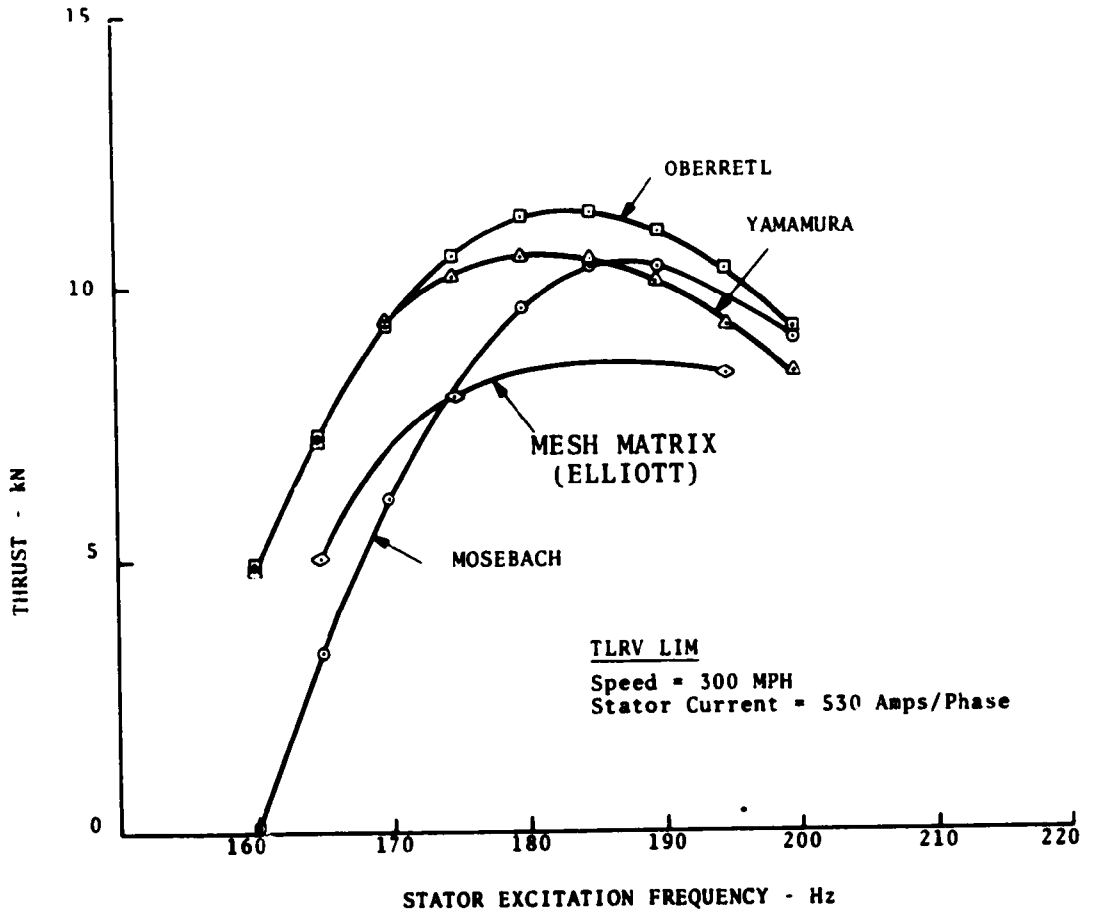

FIGURE 35. TLRV THRUST AT 134 M/S AS PREDICTED BY FOUR LEADING THEORIES

3. CONCLUSIONS

The Oberretl, Yamamura, and Mosebach theories of the linear induction motor have been reviewed and the LIM models upon which the theories are based have been examined in detail. The models have been shown to give theoretical LIM characteristics which differ significantly over the operating range of the motor. These characteristics were shown to be sensitive to the boundary conditions used to describe the finite size of the motor, e.g., the finite width and length of the primary and secondary LIM structures.

Values of LIMRV LIM thrust were computed for constant primary current excitation and specified operating slip-frequencies. The thrust predicted by the three theories deviated no more than 15-20 percent from each other. The largest thrust deviations occurred at low slip-frequencies where the thrust is a strongly dependent function of slip-frequency and motor speed. The Oberretl thrust predictions tended to be about 10-15 percent below the corresponding Yamamura and Mosebach prediction. The theoretical predictions based on the mesh-matrix LIM analysis were generally in close agreement with the Yamamura and Mosebach predictions.

Calculation of TLRV LIM thrust were also made using the three LIM computer models. The computed values of LIM thrust for constant current excitation and a speed of 300 MPH deviated about 12 percent for the Oberretl, Yamamura, and Mosebach theories; the corresponding mesh-matrix prediction was approximately 20 percent below the average of the other three predictions.

The boundary related phenomena were shown to have a large effect on the LIMRV and TLRV motor performances over the entire speed range of the two motors. Calculations made for the TLRV LIM driven with constant current show that the MMF transverse edge-effect increases LIM thrust appreciably at all motor speeds while the magnetic and MMF end-effects reduce LIM thrust at high motor speeds and low slip-frequencies. This is explained by the

fact that edge-effect is not speed dependent, while end-effect results from Eddy currents, which are generated when the motor is moving at high speeds. The effect of finite primary winding and finite primary stator core on LIM performance is of a similiar nature; both tend to reduce LIM thrust at the higher speed range of the motor. The exception to this occurs at zero slip where end-effect can develop positive thrust in the case of high-speed motors.

The important features of the Oberretl, Yamamura, and Mosebach LIM models and their relation to predicted LIM performance are summarized below.

3.1 OBERRETL LIM MODEL

a. The primary ferromagnetic region is assumed continuous in the plane of the motor. This assumption introduces errors in the description of the fields in the LIM airgap and in the regions external to the motor as well. As a consequence, the computed normal force and stored magnetic energy are overestimated in the Oberretl model; the input impedance is likewise too large due to the excessively large field energies computed for the LIM when operating at high speeds and low slip-frequencies. The assumption of continuous ferromagnetic region in the longitudinal motor direction has been shown, in the Mosebach model, to reduce LIM thrust. The effect of assuming a continuous ferromagnetic region in the transverse motor direction on LIM thrust is not clear. The numerical studies do indicate that the Oberretl theory predicts LIM thrust which tends to be below that predicted by Yamamura and Mosebach theories at most motor speeds.

b. The Oberretl theory models the LIM as a 2-dimensional array of periodic cells in the plane of the motor. Field and current distributions are described by a 2-dimensional Fourier series using k-vectors, whose fundamental are determined by the unit cell dimensions. The cell dimensions and the maximum number of harmonics used in the Fourier expansion must be carefully chosen in order to accurately describe the field distributions in the LIM.

Failure to do this can lead to large errors in the predicted LIM characteristics.

c. The Oberretl model predicts substantial flux densities at both outer edge regions of the motor. This flux is mostly due to the assumption of a continuous primary iron core extending beyond the width of the stator.

d. The mathematical development of the theory limits its application to LIMs with even numbers of electrical poles. This limitation is the result of the winding distribution factor which is valid for even pole numbers only. A modified winding factor has been derived which is valid for both even and odd numbers of electrical poles.

3.2 YAMAMURA LIM MODEL

a. The Yamamura model assumes the primary ferromagnetic region is continuous and extends to infinity along the longitudinal axis of the motor. As in the Oberretl model, this assumption results in large predicted normal forces and stored magnetic energies at high motor speeds and low slip-frequencies. It also results in somewhat larger predicted thrust than would otherwise occur.

b. The Yamamura model uses the Bolton edge-effect analysis to correct for the finite width of the motor. The Bolton correction factor neglects the end-effect; consequently its use under conditions in which the end-effect is appreciable can lead to errors. When applied to motors operated at low speeds and high slip-frequencies, the Bolton factor probably gives a reasonable approximation to the correction required for finite width LIMs.

c. The Yamamura model is based on a fundamental primary current excitation wave; it neglects higher harmonic excitations which are generated in real winding distributions. Fortunately, the contribution of the high harmonic excitations to LIM thrust is small and can be neglected in most cases. The application of the Yamamura model to LIMs having layered windings introduces

complications since each winding layer interacts differently with the end-effect.

d. The mathematical solution of the wave equation uses the theorem of residues to compute the vector potential Fourier integral. Two of the three significant roots describe damped exponential waves; the third root corresponds to the normal excitation wave. Little difference results if the negatively propagating damped wave is neglected in the final solution. The description of the LIM EM interactions in terms of a single excitation wave plus a damped exponential wave has a conceptual advantage in that the wave interactions are easy to visualized and solutions can be written in closed form.

3.3 MOSEBACH LIM MODEL

a. The Mosebach model describes the simultaneous interactions of the edge-effect, MMF end-effect, and the magnetic end-effect; it is the only one of the three models to attempt to include effects of finite iron and current excitation in the analysis. The model uses an approach similiar to that of the Oberretl model to describe the field and current distributions using a 2-dimensional Fourier series. The finite stator core is described by an airgap function. The boundary effect due to the finite length of the iron core becomes significant only at high speeds and low slip-frequencies. Due to the increased number of expansion terms required to describe the airgap function, the computer time (and cost) is considerably greater than that of the Oberretl and Yamamura computer models.

b. The Mosebach model limits the flow of secondary current to rectilinear patterns such that the currents within the active region of the motor flow in the transverse direction and currents outside the active region flow in the longitudinal direction. This restriction impacts on the computed edge-effect and the dependence of the edge-effect on slip frequency and rail configuration. The Mosebach edge-effect treatment becomes equivalent to the Bolton analysis at low slip frequencies but diverges from it

at high slip-frequencies. It is interesting that the Mosebach predicts a value for the TLRV thrust at a slip equal to 0.8 which is about 6 percent below that predicted by the Yamamura theory.

c. The finite iron core structure is described by a Fourier series representing an equivalent airgap function. In some cases, the amplitudes of the airgap harmonics can be comparable with the motor pole pitch. Since the theory assumes the airgap is much less than the pole pitch, this violates one of the basic assumptions of the model. The effect which this conflict has on the accuracy of the theoretical results is not known.

d. The computer time required for LIM calculations can be reduced by restricting the range of harmonic terms used in the Fourier expansions. The number of positive harmonics used in the field expansion could be reduced since these harmonics contribute little to the end result.

4. REFERENCES

1. Oberretl, K., "Three-Dimensional Analysis of the Linear Model Taking into Account Edge-Effects and the Distribution of the Winding," Archiv fuer Electrotechnik, 55, No. 4, 1973.

2. Yamamura, S., THEORY OF LINEAR INDUCTION MOTORS, John Wiley & Sons, New York NY, 1972.

3. Mosebach, H., "Effects of Finite Length and Width on Short Stator and Rotor Linear Induction Motors," Dissertation Technische Universität Braunschweig, 1972.

4. Bolton, H., "Transverse Edge-Effect in Sheet-Rotor Induction Motors," Proc. IEE, Vol. 116, No. 5, May 1969.

5. Iwamoto, M., Ohno, O., Itoh, T., and Shinryo, Y., "End-Effect of High Speed Linear Induction Motor," IEEE Transactions on Industry Applications, Vol IA-9, No. 6, Nov./Dec. 1973.

6. Weh, H., Waltke, G., and Appun, P., "Induction Phenomena in MHD Converters with Constant and Traveling Magnetic Field," Energy Conversion 9 (1), 31-38 (March 1969).

7. Bolton, H., "Forces in Induction Motors with Laterally Asymmetric Sheet Secondaries," Proc. IEE, 117 (12), 2241-2248, December 1970.

8. Elliott, D.G., "Matrix Analysis of Linear Machines," U.S. Department of Transportation, Federal Railroad Administration, Washington DC, Report No. FRA-OR&D-75-77, June 1975.

APPENDIX

Listing of Oberretl Computer Program

```
      PROGRAM COMPUTES REACTION FORCES AND POWER(S) USING OBERRETL THEORY.
      UNIT OF FORCE=NEWTONS UNIT OF POWER=WATTS
         LS=TOTAL LENGTH=,LL=EXIT LENGTH GAP=,G=AIRGAP,P2=SEC RES*10000000
         ZC=CORE WIDTH,Z=SEC THICKNESS,W=WIDTH PERIODICITY=,P=POLES
         M=PHASES,M=TURNS,H=WIDTH OVERHANG,E=HALF-FILLED SLOTS
         VMAX=MAX LENGTH HARMONIC ORDER,UMAX=MAX WIDTH HARMONIC ORDER
      COMPLEX     SKY,ETA,AGF1,AGF2,G1 ,E1,CTNH
      DIMENSION FTX(20),FTY(20),PT(20),TT(20),PPT(20)
      NAMELIST/NAME/F,A1
      NAMELIST/NAME2/LS,ALL,T,G,P,AM,E,ZC,H
      NAMELIST/NAME/VMAX,UMAX,P2
      NAMELIST/NAME/ZN,AS,C
    2 FORMAT(7X,2HS,9X,2HFX,9X,2HFY,7X,6HP(AIR),7X,2HPS)
    3 FORMAT(A1,1X,E10.3)
    4 FORMAT(1X,3HLS=,F6.3,1X,3HLL=,F6.3,1X,2HW=,F6.3,1X,4HGAP=,F6.3,1X,
     12HP=,F3.0,1X,2HN=,F2.0)
    5 FORMAT(1X,2HE=,F3.0,1X,2HC=,F3.0,1X,2HB=,F6.3,1X,3HP2=,F6.3,1X,
     12HM=,F3.0,1X,2HM=,F6.3,1X,2FC=,F6.3)
    6 FORMAT(1X,5HVMAX=,F4.0,1X,5HUMAX=,F4.0,1X,5HFREQ=,F4.0,1X,2HI=,F6.
     10)
      DEL=0.1
      XMAX=1./(LS+1.0
      S=0.0
      PI=3.1415
      AMU=4.*PI
      SQT2=SQRT(2.)
      READ(5,NAME)
      READ(5,NAME2)
      READ(5,NAME)
      READ(5,NAME3)
      TMAX=VMAX
      JMAX=(UMAX+1.1)/2.
      AL=ALS+ALL
      A1=AM/P
      A2=C/P
      AL=PI*S/AL**2.*DT/(2.*(E+1.1-E)
      B1=B*AL**2/2.
      B2=M*4./PI*AL
      B3=16.*B**II*SQT2/PI/AL
      K=1
   10 FX=0.0
      FY=0.0
      P1=0.0
      DO 15 J=1,JMAX
      AJ=2*J-1
      M=1
      BA=1./(1.-(AJ*2.*A1)**2)
      VW=BA*(SIN(PI*AJ*(A1+2Z))/AJ-COS(PI*AJ*2Z)*2.*A1)
      DO 15 I=1,IMAX
      M=I
```

```
   13 AI=I*N
      VS=1.-AI*(1.-S)*ANU*ALPHA/PI
      THF1=AI*ALPHA/2.
      THF2=2.*THF1
      THF3=AM*THF2
      AK=AN1/AM
      AK1=AMU*SIN(AV/2.*(THF2-PI/AM))/SIN((THF2-PI/AM)/2.)
      AJZ=AK1*AK1*STH/1000.0.
      ALPA2=(AI*2.*PI/AL)**2+(AJ*PI/W)**2
      ALGS=SQRT(ALPA2)
      AKY=CSQRT(ALPA2*(U.0)*1.0)*VS*2.*PI*F*AMU/P2)
      E1=AKY*B/2.
      CTANH=(CEXP(E1)+CEXP(-E1))/(CEXP(E1)-CEXP(-E1))
      FYA=AKY/CTANH/ALPA
      AGF1=SINH(ALPHA*G)*FTA*COSH(ALPHA*G)
      AGF2=COSH(ALPHA*G)*FTA*SINH(ALPHA*G)
      F1=AJZ*CABS(1./AGF1)
      FX=FX*F1*ALPHA*F1*F1*AIMAG(ETA)/AI*1000.
      FY=FY+   B2*ALPA2*F1*F1*(1.-(CABS(ETA))**2)/AI/AI*1000.
      G1=AGF2/AGF1
      P1=P1-B2*ALPHA*F*AIMAG*AJZ*AJZ*AIMAG(G1)/AI/AI*1000.
      N=N-2
      IF(N+1)15,13,15
   15 CONTINUE
      T(K)=S
      FTX(K)=FX
      FTY(K)=FY
      PVZ=PI-FX*(1.-S)*ANU*ALPHA*AL/PI
      PT(K)=PVZ
      PP(K)=PI
      K=K+1
      S=S+DELS
      IF(S-1.0)11,1,1
   20 WRITE(6,
      WRITE(6,
      WRITE(6,
      WRITE(6,2)
      DO 25 I=1,KEY
   25 WRITE(6,3)    T(K),FTX(K),FTY(K),PP(K),PT(K)
      STOP
      END
```

Listing of Yamamura Computer Program

```
C     PROGRAM COMPUTES LIM OUTPUT PARAMETERS USING YAMAMURA THEORY FOR
C     CONSTANT CURRENT EXCITATION. EDGE EFFECT INCLUDED IN CALCULATION.
C     IMODE=1 FOR VARIABLE FREQUENCY. IMODE=0 FOR VARIABLE SLIP.
C     THRUST AND POWER COMPUTED FOR ONE CORE SIDE.  MULTIPLY BY 2 FOR
C     TOTAL THRUST. POWER OF DLIM.
C     REQUIRED INPUT DATA:  AL=P X TP. W=SEC WIDTH. C=HALF CORE WIDTH
C     B=SEC THICKNESS. GAP=AIRGAP. TP=POLE PITCH. P=NO. OF POLES
C     E=NO. OF HALF FILLED SLOTS. Q=SLOTS/PHASE BELT. AN=TURNS/SLOT
C     AM=NO. PHASES. IMODE=FREQ-VERSUS-SLIP OUTPUT. PS=SEC RES X 10000000.
C     AMU2=REL PERM. OF SEC. AMU3=REL PERM OF AIR. AII=CURRENT/CONDUCTOR
C     FREQ=MOTOR FREQUENCY. FOR VARIABLE FREQUENCY OUTPUT FORMAT. CHOOSE
C     FREQ EQUAL TO INITIAL INPUT FREQUENCY.  FO=MOTOR SPEED/2./TP
C     MKS UNITS. LENGTH IN METERS. FORCE IN NEWTONS
      COMPLEX GAMMA1,TNH,AMBDA,UV
      COMPLEX FX21,FX22,FX31,FX32,FX11,FX42
      COMPLEX ZB,ZC,Z(9),GAMMA,E1,E2,C1,C2,S1,S2
      COMPLEX F(3),DF(3),CERF,G(3),FX1,FX2,FX3,DZ
      COMPLEX DGAMMA,AA,BB,GAMMA2
      DIMENSION T(20),FX(20),FY(20),DFL(3,20),POWER(20),EFF(20)
    1 FORMAT(1X,5HFREQ=,F5.0,1X,3HFQ=,F6.1,1X,3HII=,F6.0,1X,3HTP=,F6.3)
    2 FORMAT(       17X,2HFX,6X,9HP(AIRGAP),4X,3HEFF)
    3 FORMAT(4X,F6.2,2X,2(1X,E10.3),1X,F6.3)
    4 FORMAT(1X,2HL=,F6.3,1X,2HB=,F6.4,1X,2HW=,F6.3,1X,2HC=,F6.3
     1,1X,4HGAP=,F6.3,1X,2HP=,F3.0,1X,2HM=,F2.0)
    5 FORMAT(1X,2HE=,F3.0,1X,2HQ=,F3.0,1X,3HP2=,F6.3,1X,2HN=,
     1F3.0,1X,5HAMU2=,F6.2,1X,5HAMU3=,F6.2)
    6 FORMAT(2X,F4.0,F7.3,2(1X,2F7.2),2X,2(1XF4.3),3I5)
    9 FORMAT(4X,1HF,3X,5HXI(1),6X,5HXI(2),10X,5HXI(3),6X,4HETA1
     1,1X,4HETA2,3X,4HIER0,1X,4HIER1,1X,4HIFR2)
   40 FORMAT(1X,6F10.3)
   41 FORMAT(6F10.4)
   42 FORMAT(5F10.1,I5)
   43 FORMAT(4F10.3)
   44 FORMAT(2F10.1)
      SQT2=SQRT(2.)
      S=1.0
      PI=3.14159
      AMU=4.*PI
      N=1
    8 CONTINUE
      READ(5,41,END=99)AL,W,C,B,GAP,TP
      READ(5,42)P,F,Q,AN,AM,IMODF
      READ(5,43)PS,AMU2,AMU3,AII
      READ(5,44)FREQ,FO
      XMODE=IMODE
      AK=PI/TP
      GF=2.*PI*FREQ*AMU*B/PS/(B+2.*GAP)/AK/AK
      ALPHA=PI/Q/AM
      AKW1=SIN((AM*Q-F)/2.*ALPHA)*SIN(Q*ALPHA/2.)/SIN(ALPHA/2.)
      AJZ=6.*SQT2*AN*AII*AKW1/TP/100000.
      K=1
C     NEXT COMPUTE BOLTON'S FACTORS=ETA1,ETA2
   10 S=1.-FO/FREQ*XMODE
      GS=GF*S
      GAMMA1=AK*CSQRT(1.+(0.0,1.0)*GS)
      E2=CEXP(C*GAMMA1)
      S2=0.5*(E2-1./E2)
      C2=0.5*(E2+1./E2)
      TNH=S2/C2
      AMBDA=1./(1.+GAMMA1*TNH*TANH(AK*(W/2.-C))/AK)
      UV=AMBDA*TNH/GAMMA1/C
```

```
      U=REAL(UV)
      V=AIMAG(UV)
      ETA1=(1.-U-GS*V)/(1.-GS*V+GS*GS*U)
      ETA2=((1.-GS*V)**2+(GS*U)**2)/(1.-GS*V+GS*GS*U)
      P2=PS/ETA1
C     NEXT COMPUTE ROOTS OF F(N) USING NEWTON-RAPHSON METHOD. ZB,ZC ARE
C     FIRST APPROXIMATION ROOTS.
      A1=2.*PI*FREQ*AMU/P2
      A2=A1*B/4./AK/(GAP+B/2.)
      ZA=-AK
      ZB=(0.0,-1.0)*A2*((1.-S)-CSQRT((1.-S)**2+(0.0,1.0)*AK/A2**2.))
      ZC=(0.0,-1.0)*A2*((1.-S)+CSQRT((1.-S)**2+(0.0,1.0)*AK/A2**2.))
      Z(1)=ZA
      Z(2)=ZB
      Z(3)=ZC
   15 CONTINUE
      S=(1.-FQ/FREQ)*XMODE+S*(1.-XMODF)
      GS=GF*S
      GAMMA1=AK*CSQRT(1.+(0.0,1.0)*GS)
      E2=CEXP(C*GAMMA1)
      S2=0.5*(E2-1./E2)
      C2=0.5*(E2+1./E2)
      TNH=S2/C2
      AMBDA=1./(1.+GAMMA1*TNH*TANH(AK*(W/2.-C))/AK)
      UV=AMBDA*TNH/GAMMA1/C
      U=REAL(UV)
      V=AIMAG(UV)
      ETA1=(1.-U-GS*V)/(1.-GS*V+GS*GS*U)
      ETA2=((1.-GS*V)**2+(GS*U)**2)/(1.-GS*V+GS*GS*U)
      P2=PS/ETA1
      A1=2.*PI*FREQ*AMU/P2
      AJ1=ETA2*AJZ
      DO 25 N=1,3
      IEND=8
      IF(N.EQ.1)IEND=1
      DO 18 I=1,IEND
      ZR2=REAL(Z(2))
      ZI2=AIMAG(Z(2))
      GAMMA3=ZR2*ZR2-ZI2*ZI2-A1*ZI2*(1.-S)/AK
      GAMMA4=2.*ZR2*ZI2+A1*ZR2*(1.-S)/AK+A1
      GAMMA2=Z(N)*Z(N)
   16 GAMMA2=(GAMMA2+(0.0,1.0)*A1*(Z(N)*(1.-S)/AK+1.))
      GAMMA=CSQRT(GAMMA2)
   90 DGAMMA=(Z(N)+(0.0,1.0)*A1*(1.-S)/2./AK)/GAMMA
      E1=CEXP(GAMMA*B/2.)
      E2=CEXP(Z(N)*GAP)
      C1=0.5*(E1+1./E1)
      C2=0.5*(E2+1./E2)
      S1=0.5*(E1-1./E1)
      S2=0.5*(E2-1./E2)
      IF(N.EQ.1)GO TO 20
      AA=C1*S2+Z(N)*C1*C2*(GAP)+AMU3/AMU2*GAMMA*S1*S2*(GAP)
      BB=Z(N)*B/2.*S1*S2+AMU3/AMU2*(S1*C2+GAMMA*B/2.*C1*C2)
      DERF=AA+BB*DGAMMA
      F(N)=Z(N)*C1*S2+AMU3/AMU2*GAMMA*S1*C2
      DZ=F(N)/DERF
      ADZ=CABS(DZ)
   18 Z(N)=Z(N)-DZ
C     END OF NEWTON-RAPHSON CALCULATION.
      DEL(N,K)=-ALOG10(ADZ)
C     DEL(N,K)=PARAMETER DEFINING ROOT CONVERGENCE. DEL SHOULD BE POSI-
C     TIVE AND GREATER THAN 3 FOR CORRECT RESULTS.
   20 F(N)=Z(N)*C1*S2+AMU3/AMU2*GAMMA*S1*C2
      DF(N)=DERF
      G(N)=C1*C2+GAMMA*S1*S2/Z(N)
   25 CONTINUE
```

```
      FX1=-P*TP*G(1)/F(1)*(0.0,1.0)
      ZR2=REAL(Z(2))
      ZI2=AIMAG(Z(2))*AL
      ZI3=AIMAG(Z(3))*AL
      ZR3=REAL(Z(3))
      IF(ZI2.GT.30.)ZI2=30.
      IF(ZI3.LT.-30.)ZI3=-30.
      FX21=(1.-EXP(-ZI2)*CEXP((0.0,1.0)*(ZR2+AK)*AL))
      FX21=FX21/(Z(2)+AK)
      FX31=-(1.-EXP(ZI3)*CEXP((0.0,-1.)*(ZR3+AK)*AL))
      FX22=G(2)/(Z(2)+AK)/DF(2)
      FX32=G(3)/(Z(3)+AK)/(Z(3)+AK)/DF(3)
      FX2=FX21*FX22
      FX3=FX31*FX32
      POWER(K)=-PI*FREQ*AMU*AJ1*AJ2*REAL(FX1*FX2+FX3)*2.*C*1000.
      FX(K)=0.5*AJ2*AJ1*AMU*REAL(Z(1)*FX1+Z(2)*FX2+Z(3)*FX3)
     1*1000.*2.*C
      EFF(K)=FX(K)*2.*TP*FREQ*(1.-S)/POWER(K)
      T(K)=FREQ*XMODE+(1.-XMODE)*S
      K=K+1
   28 CONTINUE
      FREQ=(FREQ+5.)*XMODE+FREQ*(1.-XMODE)
      S=(S-.1)*(1.-XMODE)+S*XMODE
      IF(K-11)15,15,30
C     PROGRAM COMPUTES 11 DIFFERENT SLIP-FREQUENCY CASES.
   30 CONTINUE
      WRITE(6,11)(DEL(2,K),K=1,11)
      WRITE(6,11)(DEL(3,K),K=1,11)
   11 FORMAT(1X,11(1X,F4.1))
      WRITE(6,6)AL,B,W,C,GAP,P,AM
      WRITE(6,5)E,Q,PS,AN,AMU2,AMU3
      WRITE(6,1)FREQ,FQ,AI1,TP
   32 WRITE(6,2)
      DO 35 K=1,11
   35 WRITE(6,3)T(K),FX(K),POWER(K),EFF(K)
      GO TO 8
   99 STOP
      END
```

*U.S. GOVERNMENT PRINTING OFFICE: 1977—702-531/13

120 Copies